I. Impact of Volcanic Aerosols on Stratospheric Chemistry    II. $O_2(^1\Sigma g^+)$ and $O_2(^1\Delta g)$ in the H + $O_2$ Reaction System    III. Barotropic Instability of Zonal Jets on Mars, Earth and Venus

Thesis by

Diane V. Michelangeli

In partial fulfillment of the requirements

for the Degree of

Doctor of Philosophy

California Institute of Technology

Pasadena, California

1989

(submitted 15 July 1988)

*This thesis is dedicated with love to my parents and my sister Lucy*

*Cette thèse est affectueusement dédiée à mes parents et ma soeur Lucy*

## Acknowledgements

Years spent as a graduate student are challenging, frightening, and extremely rewarding when a life–long dream finally becomes reality. The transition from student to independent scientist, and the birth of a thesis cannot occur in a vacuum; therefore, an extensive network of friends, teachers, and more generally, "people who care", is crucial.

I start by thanking my parents for believing in my desire to go to California for an education, and not only for the weather! Their love and strong faith in my ability kept me striving forward. I also thank them for sending Lucy to "take care of me" every year.

Professor Yuk Yung is a great thesis advisor. This statement is based on the concept that the "advising" must not be limited to intellectual questions, but must extend to the development of the body, and spirit. I will forever remain fascinated by Yuk's views on psychology, sociology, philosophy, religion, economy, politics, etc... In the traditional "scientific" manner, your enthusiasm, ideas, guidance and...jokes...were greatly appreciated. And a big thank you for letting this chemist dissappear to JPL for a few years to get "dirty hands".

A huge, and truely felt, thank you is addressed to Dr. Mark Allen. Your knowledge, guidance, friendship and patience (most of the time!) kept me marching forward towards the completion of this work. Thank you for always being there – and thank Emily for inviting me to dinner that "special" night!

My dream of doing experimental planetary science could not have been fulfilled without the tremendous help of Dr. Ming–Taun Leu. I am deeply grateful for your undying patience and trust in me. I thank Dr. Bill DeMore for welcoming me in his laboratory, and for the financial support I received from him. I would also

like to extend my deepest thank you to the entire group, for sharing their knowledge with me, and especially for treating me as "part of the group".

From a class – to a term project – to a paper – to a thesis – that was the development of my work and association with Dr. Rich Zurek. Your good humor, kindness, understanding, ideas,...all so remarkable and appreciated. Guess what?...you won...I'm off into the world of dynamics!

I am grateful to all the planetary science and geochemistry professors who have contributed to my general education. In particular, I thank Dr. Andrew Ingersoll for his direction as my academic advisor, and Dr. Sam Epstein for his help during the research of my first year at Caltech.

To my Friends: George: thank you for providing the distractions, stability, understanding, as well as scientific judgement needed through my learning years. Run Lie: our long talks, your wonderful family, your friendship, were all so important to me. Randy: thanks for being the "big–brother" I always wanted. Gloria: your friendship arrived at such a crucial time, and will never die, even with the distance. Lionel: the extent of your patience in dealing with the depression of this last year was immeasurable. Thank you for being so supportive.

Thanks to my office–mates (so...Ken, Julie and Kathy) for being "fun", and to all my friends who have talked and listened, and talked and listened over the years...Carol, Don, Jun Shan, Bridget, Walter, Mark, Tim, Dave, and the ghosts of students passed and present.

Finally, nothing would have been possible without the administrative, and "political" advice offered by Kay Campbell, and the excellent word processing skills of Donna Lathrop, who was in particular very helpful during the completion of this thesis.

# ABSTRACT

In order to fully understand an atmospheric system, we must answer questions in radiative transfer (Paper I), dynamics (Paper II), and chemistry (Paper I). The adequacy of the chemical models at reproducing the atmosphere depends on the fundamental knowledge of rate constants and absorption cross sections, which are determined in laboratory experiments (Paper III). All these issues are investigated in the three independent papers of this thesis. While seemingly unrelated, they all attempt to explain observations of terrestrial atmospheres. Paper I focusses on the chemical effects, in the Earth's stratosphere, of a volcanic eruption. Paper II reports experimental results important for the understanding of nightglow emissions on Earth. And finally, Paper III discusses barotropic instabilities as a possible explanation for thermal waves on Mars.

## PAPER I

### Impact of Volcanic Aerosols on Stratospheric Chemistry

We have studied the consequences of the eruption of the El Chichon volcano on the Earth's stratospheric chemistry. The volcanic aerosol cloud, formed after the eruption, was very efficient at altering the radiation field. The results of a one–dimensional radiative transfer model show that the total radiation increased and decreased mainly within the aerosol layer longward and shortward of 3000 Å, respectively. The photolysis rates obtained from a one–dimensional photochemical model vary consistently with the total radiation changes. $O_3$, $NO_2$ and $ClNO_3$ photodissociation rate constants increase by nearly 10%, while those for $H_2O$, $NO$ and $HCl$ decrease by as much as 15%. The effect of a temperature variation caused by the radiation change was also added to the photochemical model, and contributed

to the changes in concentrations. Ozone decreases by 7% at 24 km, which compares well with the SBUV measurements of a 5–10% decrease. The hydrochloric acid increases by 10% at 24 km, which is low with respect to the observations of 30–40% increase. A direct injection of chlorine or hydrochloric acid into the stratosphere produces only the measured increase for very large injections. The observations of an increase in OH and a decrease in NO, and $NO_2$ led us to investigate the effect of a water injection, which ended up violating the HCl observations. The possible important heterogeneous reactions involving the aerosols were evaluated in order to explain the $NO_x$ measurements. It is impossible to reproduce all the existing observations with any one reaction. These last investigations are of general interest because of the possible involvement in the explanation of the Antarctic ozone hole.

## PAPER II

### $O_2(^1\Sigma g^+)$ and $O_2(^1\Delta g)$ in the H + $O_2$ Reaction System

The generation of metastable $O_2(^1\Sigma g^+)$ and $O_2(^1\Delta g)$ in the H + $O_2$ system of reactions was studied by the flow discharge chemiluminescence detection method. In addition to the $O_2(^1\Sigma g^+)$ and $O_2(^1\Delta g)$ emissions, strong OH $(\nu = 2) \rightarrow$ OH $(\nu = 0)$, OH $(\nu = 3) \rightarrow$ OH $(\nu = 1)$, $HO_2\,(^2A'_{000}) \rightarrow HO_2\,(^2A''_{000})$, $HO_2\,(^2A'_{001})$ $\rightarrow HO_2\,(^2A''_{000})$, and $HO_2\,(^2A''_{200}) \rightarrow HO_2\,(^2A''_{000})$ emissions were detected in the H + $O_2$ system. The rate constants for the quenching of $O_2(^1\Sigma g^+)$ by H and $H_2$ were determined to be $(5.1 \pm 1.4) \times 10^{-13}$ and $(7.1 \pm 0.1) \times 10^{-13}$ $cm^3$ $s^{-1}$, respectively. An upper limit for the branching ratio to produce $O_2(^1\Sigma g^+)$ by the H + $HO_2$ reaction was deduced from the experiments to be 2.1%. The contributions from other reactions producing singlet oxygen were investigated.

viii

## PAPER III

### Barotropic Instability of Zonal Jets on Mars, Earth and Venus

We have used a linearized nondivergent barotropic vorticity model on a sphere to intercompare the fastest growing, barotropically unstable wave modes computed for zonal jets at high latitudes in the middle atmospheres of Venus, Earth, and Mars. Such zonal jets have been observed in the wintertime stratosphere on Earth and have been inferred from remotely sensed temperatures in the Venus middle atmosphere and in the wintertime Martian atmosphere. The comparison was done by extending the results of Hartmann (1983) for his simple analytic profile of a latitudinally varying terrestrial zonal wind to zonal wind profiles characterized by the larger Rossby numbers $Ro$, appropriate to Mars and Venus. As Hartmann's results suggested, the fastest growing barotropic waves continue to grow more quickly as $Ro$ increases. Eventually, the fastest growing mode shifts from a zonal wavenumber $k = 1$ to a $k = 2$ mode, both located on the poleward flank of the high–latitude jet. However, for somewhat higher Rossby numbers, the $k = 2$ mode on the equatorward side of the zonal jet becomes the fastest growing planetary–scale barotropic mode, and this transition is marked by a discontinuous shift to longer wave periods. The Venus high–latitude zonal jet appears remarkably close to this transition $Ro$. For each of the three planets, satellite–borne instruments have detected wave patterns in the thermal radiance field in the vicinity of the high–latitude zonal jets. As reported earlier for the terrestrial wintertime stratosphere by Hartmann and for Venus by Elson (1982), these observed waves have characteristics similar to those computed for the fastest growing barotropic modes. For Mars, we find that such modes would have zonal wavenumbers 1 or 2, with $e$–folding times of 2–3 days and periods of 0.75–2.5 days; the longer period, $k = 2$ equatorward mode would dom-

inate for the faster and narrower zonal jets. A poleward mode with $k = 1$ and a period of 1.2 days is the barotropic mode most likely to be consistent with the Mariner 9 IRIS observations of thermal waves above the 1 mb ($\sim 20$ km) level in the Martian atmosphere.

# Table of Contents

# List of Figures

Paper III

# List of Tables

# PAPER I

# Impact of the El Chichon Volcanic Aerosols
# on Stratospheric Chemistry

# Impact of the El Chichon Volcanic
# Aerosols on Stratospheric Chemistry

Diane V. Michelangeli, Mark Allen,[1] and Yuk L. Yung

Division of Geological and Planetary Sciences

California Institute of Technology

Pasadena, California    91125

[1] Also at Jet Propulsion Laboratory, California Institute of Technology, 4800 Oak Grove Drive, Pasadena, California 91109.

## ABSTRACT

We have studied the consequences of the eruption of the El Chichon volcano on the Earth's stratospheric chemistry. The volcanic aerosol cloud, formed after the eruption, was very efficient at altering the radiation field. The results of a one–dimensional radiative transfer model show that the total radiation increased and decreased mainly within the aerosol layer longward and shortward of 3000 Å, respectively. The photolysis rates obtained from a one–dimensional photochemical model vary consistently with the total radiation changes. $O_3$, $NO_2$ and $ClNO_3$ photodissociation rate constants increase by nearly 10%, while those for $H_2O$, NO and HCl decrease by as much as 15%. The effect of a temperature variation caused by the radiation change was also added to the photochemical model, and contributed to the changes in concentrations. Ozone decreases by 7% at 24 km, which compares well with the SBUV measurements of a 5–10% decrease. The hydrochloric acid increases by 10% at 24 km, which is low with respect to the observations of 30–40% increase. A direct injection of chlorine or hydrochloric acid into the stratosphere produces only the measured increase for very large injections. The observations of an increase in OH and a decrease in NO, and $NO_2$ led us to investigate the effect of a water injection, which ended up violating the HCl observations. The possible important heterogeneous reactions involving the aerosols were evaluated in order to explain the $NO_x$ measurements. It is impossible to reproduce all the existing observations with any one reaction. These last investigations are of general interest because of the possible involvement in the explanation of the Antarctic ozone hole.

## 1.1  Introduction

Interest in developing accurate stratospheric photochemical models emerged when it was realized that anthropogenically produced halocarbons had an adverse impact on the ozone layer (Molina and Rowland, 1974; Rowland and Molina, 1975; Cicerone et al., 1983; Prather et al., 1984). The long–term effects of man–made pollutants can only be predicted with good models. Therefore, proving that a model is a good representation of the real atmosphere is crucial for establishing its predictability. Stratospheric photochemical modeling has undergone many stages of refinement, and a critical evaluation of remaining problems was made by Watson et al. (1985). Nevertheless, the models still do not adequately reproduce the ensemble of ozone concentration measurements above 35 km (see for example Watson et al., 1985).The newly discovered ozone hole over Antarctica, appearing in the spring, was never predicted by any polar stratospheric simulations (Farman et al., 1985).

One of the best ways of testing the adequacy of our photochemical model at representing the atmosphere is by studying its response to a known change. The time scale for the response has to be short enough so that we may observe the changes in the atmosphere. For example, it is difficult to evaluate whether or not our models respond well to halocarbon, $CO_2$ or $CH_4$ injections, because the atmosphere takes many years to show a measurable effect. Some examples of useful changes to study are the diurnal and seasonal variations seen in concentration profiles, solar eclipses, and volcanic eruptions. When the aerosol concentration increases suddenly, because of an explosive volcanic eruption, we expect the atmosphere to respond. There are measured variations in temperature, radiation field, general weather patterns, planetary albedo, or chemical species concentrations. Based on the current understanding of the scattering and chemical properties of volcanic aerosols, we can

use our models to investigate their impact, and calculate, for example, the radiation field and species concentrations. If the predictions of the model are in good agreement with the observations of changes after the eruption, we can conclude that the theoretical model responds well to this perturbation in the atmosphere.

In this work, we investigate the impact on the stratosphere of the March-April, 1982 eruptions of the El Chichon volcano (17.33° N, 93.2° W) (see for example Pollack $et\ al.$, 1983). There was an injection of more than $10^{12}$ g of $SO_2$ into the stratosphere at 30 km (Krueger, 1983). The $SO_2$ was oxidized to $SO_3$, which subsequently reacted with water to form $H_2SO_4$. After condensation, sulfuric acid aerosols composed of 75% $H_2SO_4$, 25% $H_2O$ were formed (Hofmann and Rosen, 1984). After three weeks, the volcanic cloud had circled the globe between 0 and 30°N. The altitude of the peak aerosol concentration had dropped to 27 km after eight weeks (Barth $et\ al.$, 1983).

These first stages of the impact of the eruption on the stratosphere were investigated by McKeen $et\ al.$ (1984). They modeled the chemical effects of the formation of $H_2SO_4$, and compared their calculated $SO_2$ chemical lifetimes with observations. In this way, they were able to put constraints on the $HSO_3$–to–sulfate conversion. Their calculations (with $5 \times 10^{12}$ g $SO_2$ at 20° N, 60 days after the eruption) predicted a decrease in OH by more than an order of magnitude because of the formation of $HSO_3$. This OH decrease diminished the rate of the reaction of OH with $NO_2$ to form $HNO_3$, and therefore, $NO_2$ was found to increase by more than a factor of two. Furthermore, they predicted an order–of–magnitude decrease in ClO, and argued that an $O_3$ increase should be expected. These predictions of OH decrease and $O_3$ increase were not confirmed by comparison with observations of Burnett and Burnett (1984), Heath and Schlesinger (1984), or Chandra (1987).

The photochemical calculations of McKeen $et\ al.$ (1984) reflected the chemical

response of the atmosphere to the formation of $H_2SO_4$ from the $SO_2$ injected during the volcanic eruption. Thomas *et al.* (1983) found that the peak in the optical depth of the aerosol cloud was reached 15 weeks after the eruption. After that date, the decline was consistent with the gravitational settling time. Therefore, all important chemical effects that were due to the process of formation of the sulfate particles, as modeled by McKeen *et al.* (1984), were complete by July. McKeen *et al.* (1984) did not consider that any radiative effects were due to increased scattering caused by the aerosol cloud. The optical depth of the stratospheric aerosols was near 0.25 at 6000–7000 Å (DeLuisi *et al.*, 1983) in June-July, 1982. This is a substantial increase in the aerosol content of the stratosphere, because the background level of the aerosol optical depth is only about $10^{-3}$ (see, for example, Wang and McCormick, 1985). This aerosol–cloud layer, spread out between 16 and 30 km (DeLuisi *et al.*, 1983), was still observable a year after the eruption (Hofmann and Rosen, 1983; Thomas *et al.*, 1983; Adriani *et al.*, 1983; Spinhirne and King, 1985). Jäger and Carnuth (1987) tracked the aerosol layer until the end of 1985. Therefore, the impact of this cloud on the stratosphere could be very significant. Pollack and Ackerman (1983) showed theoretically that the volcanic cloud increased the planetary albedo, decreased the temperature and solar radiation below the cloud, and increased the temperature within the cloud. This last prediction matched the observations of Labitzke *et al.* (1983) and Quiroz (1983). The corresponding cooling of the troposphere was not observed (Angell and Korshover, 1983), and a possible explanation given was that of a compensating El Niño effect.

The aerosols change the radiation field in the stratosphere and therefore have a direct effect on photolysis rates, and on concentrations of species. The purpose of this study is first to investigate and quantify the effect of the El Chichon volcanic aerosols on the chemistry of the stratosphere through the radiation changes.

To study the radiation field, we first use a one–dimensional radiative–transfer model to calculate the total actinic flux (attenuated solar beam and scattered flux) within the stratosphere. This is done for a standard "clear" model atmosphere, and for an "aerosol–containing" one based on the observational data of optical depth increase. A one–dimensional chemical kinetics model (Froidevaux *et al.*, 1985) uses the diffuse actinic flux values from the radiative transfer model. The changes in photochemical rates and concentrations, because of the inclusion of aerosols, are studied. A temperature perturbation based on a measured change, is also added to the "aerosol–containing" case.

All our calculations are compared to observations of changes in concentrations of $O_3$, HCl, NO, $NO_2$, $HNO_3$ and OH after the eruption of the volcano. In order to explain the change in HCl, we investigate the effect of a direct injection of $Cl_2$ and/or HCl into the stratosphere. To explain the $NO_x$ and OH variations, we consider an injection of water from the volcano. We discuss the consequences of these injections on all other species in the stratosphere.

Many ideas have flourished in an attempt to explain the Antarctic ozone hole. In the "chemical" solutions, scientists have proposed that the polar stratospheric clouds, present during that season, act as important catalysts of heterogeneous reactions involving $N_2O_5$, $ClNO_3$, HCl, and $H_2O$ (Solomon *et al.*, 1986; McElroy *et al.*, 1986). The verification of these theories remains difficult at this time, because of the lack of adequate, reproducible experimental data. Nevertheless, we can place certain constraints on the extent of their importance globally by studying the case of similar heterogeneous reactions on the surface of the volcanic aerosols. Our conclusions are limited by the difference in the surface chemistry properties of sulfuric acid aerosols and ice/$HNO_3$ crystals.

## 1.2   Radiative Transfer

The radiative transfer model (for details see Michelangeli *et al.*, 1988) treats the attenuation of the solar beam using spherical geometry, while the multiple scattering is evaluated for an inhomogeneous, plane parallel atmosphere. In the model, the direct solar beam is attenuated by Rayleigh scattering by $N_2$ and $O_2$ and absorption by $O_3$, $O_2$ and $NO_2$. The total actinic flux combines the direct flux and the diffuse actinic flux (multiple scattering). The calculations are performed for solar zenith angles between 0 and 89°, wavelengths from 1750 to 8000Å, and altitudes from 0 to 50 km. A Lambert surface with an albedo of 0.25 is prescribed at the lower boundary. The sulfuric acid aerosols are added to the model as multiple scatterers of the radiation.

The optical properties of the aerosols were taken from the calculations of Pollack and Ackerman (1983), which compared well with the data of Knollenberg and Huffman (1983) and Clarke *et al.* (1983). The average single scattering albedo (0.99), and the asymmetry factor ($g$=0.7) for the Henyey–Greenstein phase function (Van de Hulst, 1980; Hansen and Travis, 1974), are independent of wavelength. The particle extinction cross section ranges from $1.8 \times 10^{-8}$ cm$^2$ at 8000 Å to $1.4 \times 10^{-8}$ cm$^2$ for $\leq 2560$ Å. From the total "dust" optical depth as a function of wavelength recorded in June–July, at Mauna Loa in Hawaii (20°N) (Figure 3 of DeLuisi *et al.*, 1983) and the backscattering ratio obtained by lidar sounding (Figure 1 of DeLuisi *et al.*, 1983), we obtain the vertical distribution of the optical depth change that is due to volcanic aerosol loading as a function of wavelength. The aerosols are spread out from 16 to 30 km, and the largest optical depth increase was between 27 and 29 km (40% of total optical depth change). In a "clear" atmosphere (no aerosol scattering), there is little flux shortward of 3000 Å and below 50 km.

This is mainly due to the extremely high absorption cross–section of $O_3$ (Hartley bands from 2000 to 3000 Å) and $O_2$ (Schumann–Runge and Herzberg bands below 2000 Å) (Liou, 1980). When the aerosols are included in the calculations, above the cloud there is no change in the direct solar beam, but within and below the cloud, the direct flux is attenuated by as much as 28% at longer wavelengths (Fig. 1a). In regions of large absorption ($O_3$ at 2500 Å and $O_2$ below 2000 Å) the direct and diffuse fluxes are zero and do not change when the cloud is included (Figs. 1b, 2b). At these wavelengths, the total radiation does not change, regardless of the altitude (Fig. 3b). At other wavelengths below 3000 Å, the aerosols increase the pathlength, and therefore enhance the absorption, so that the direct beam is more attenuated than at longer wavelength, where the absorption is less important (Fig. 1b). This effect is also present at 6000 Å, where the ozone Chappuis bands have their peak.

The aerosols, being nearly white scatterers, increase the diffuse flux at all wavelengths, except where it is zero (below 2000 Å and near 2500 Å) (Fig. 2a, 2b). The largest change ($> 100\%$) was obtained within the aerosol layer. Since the scattering cross section increases slightly at longer wavelengths, the largest enhancement in the diffuse flux is found at 8000 Å. Below 3000 Å, the percent changes are large at all altitudes because of the small values of flux ($< 10^{-3}$ photons $cm^{-2} s^{-1}$) that are due to the large absorption, but are of little consequence since the direct flux dominates the total radiation. The diffuse flux varies as a function of solar zenith angle in the way described by Luther and Gelinas (1976), and Froidevaux et al. (1985) for both "clear" and "aerosol–containing" cases. There is a smooth decrease in the flux with increasing angle. At 90° solar zenith angle, the curves converge to near zero flux at the ground.

Above the aerosol layer, the total radiation increases by 2%, because of the extra backscattering. The largest increase is within the layer (10%) at 8000 Å (Fig.

3a). Longward of 3000 Å, the diffuse flux dominates the total radiation when the aerosols are present, giving rise to large increases ($\sim$ 100%) observed (Fig. 3b). Below 2000 Å and at 2500 Å, no change in total radiation is obtained, since the fluxes are zero (Fig. 3b). At 3000 Å and 6000 Å, the direct flux is the largest component of the total radiation and therefore, we observe a decrease in the total radiation at 3000 Å and lower values than expected at 6000 Å (Fig. 3a) This effect at 6000 Å is caused by the $O_3$ Chappuis bands and disappears on removal of the $O_3$ Chapuis absorption.

Below the aerosol layer we obtain a few percent increase. This result is counter-intuitive, since we would expect the aerosols to decrease the total radiation at the ground. This effect is described in detail by Michelangeli *et al.* (1988). The calculations show that the presence of aerosols leads to a trapping of photons in the atmosphere.

It is interesting to note that the presence of the aerosols increases the radiation within the aerosol layer and is responsible for the temperature change computed by Pollack and Ackerman (1983), and observed by Labitzke *et al.* (1983) and Quiroz (1983). It is also important to consider these results in comparison with the observations of DeLuisi *et al.* (1983). They measured with open–band and broad–band filters, a 5.6% decrease in the total radiation in the 0.3 to 3 $\mu$m bands at noon with a pyranometer at Mauna Loa. This measurement corresponds to the irradiance, not to the actinic flux. At solar zenith angles of 0° and 45°, and 7000 Å, we obtain a 1.3% and a 3.8% irradiance decrease, respectively. These results agree well with the observations. They also found that the direct flux alone had decreased by 21.3%, which compares very well with our 21.6% decrease at 0° solar zenith angle and 7000 Å. Therefore, our calculations of radiative transfer are in good agreement with observations.

The chemical and radiation calculations were made self-consistent. After running the photochemical model, with the new radiation field after the aerosols were added, we obtained different $O_3$ and $NO_2$ concentrations, which we used in a second radiative transfer calculation. Comparing the new results to the previous ones, we found that there was less than a 1% difference in the radiation change above 3000 Å. We therefore conclude that this effect is minor.

Figure 1a. The percent difference in the direct flux as a function of altitude (in km) and wavelength from 3000 to 8000 Å for a solar zenith angle of 45°. The percent difference in $X$ is defined as: $\left[\left(X_{\text{aerosols}} - X_{\text{no aerosols}}\right) / X_{\text{no aerosols}}\right] \times 100$.

Figure 1b. Same as Figure 1a except from 1750 to 3000 Å

Figure 2a. Same as Figure 1a except for the diffuse flux.

Figure 2b. Same as Figure 1b except for the diffuse flux.

Figure 3a. Same as Figure 1a except for the total radiation.

Figure 3b. Same as Figure 1b except for the total radiation.
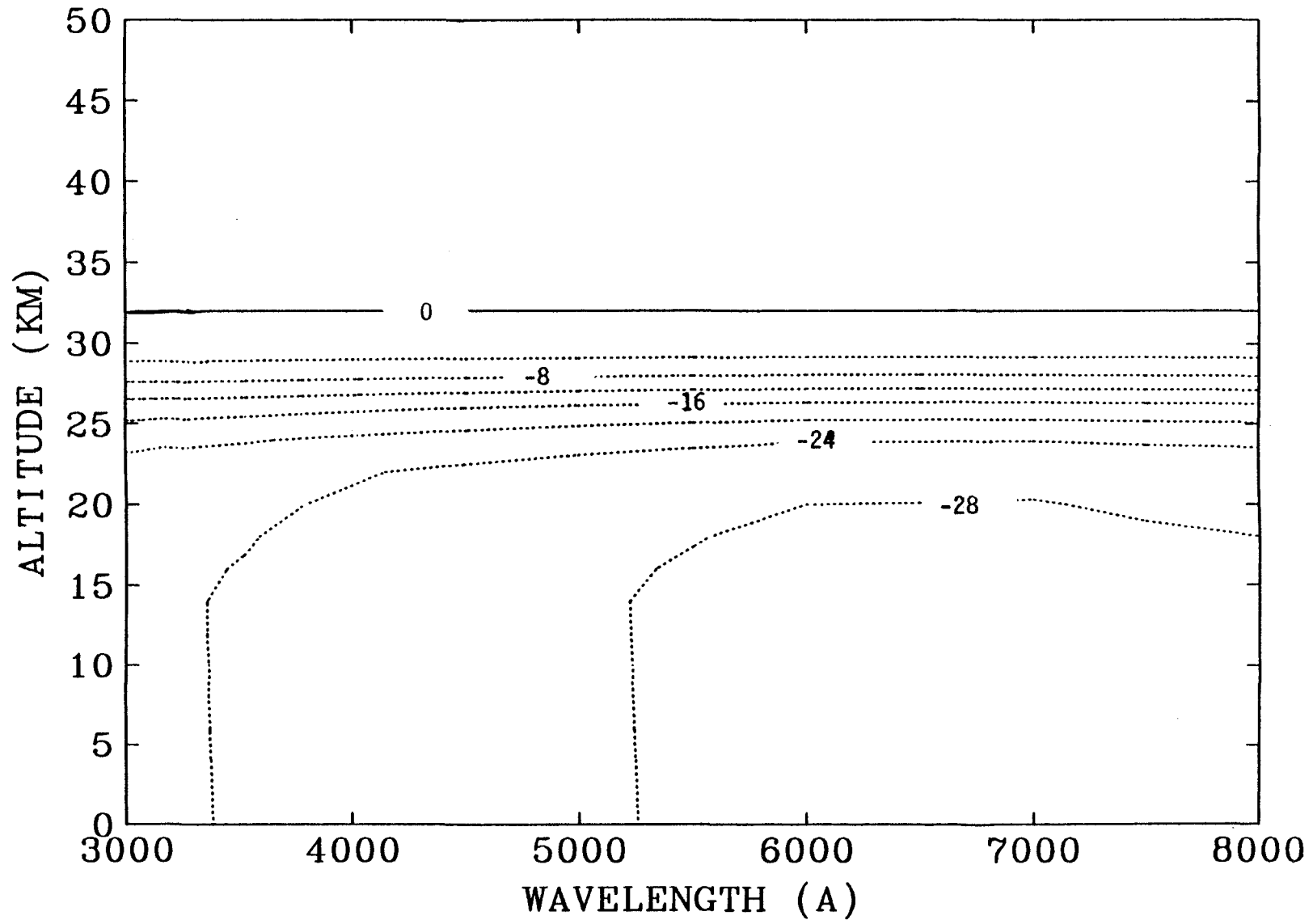
Figure 1a
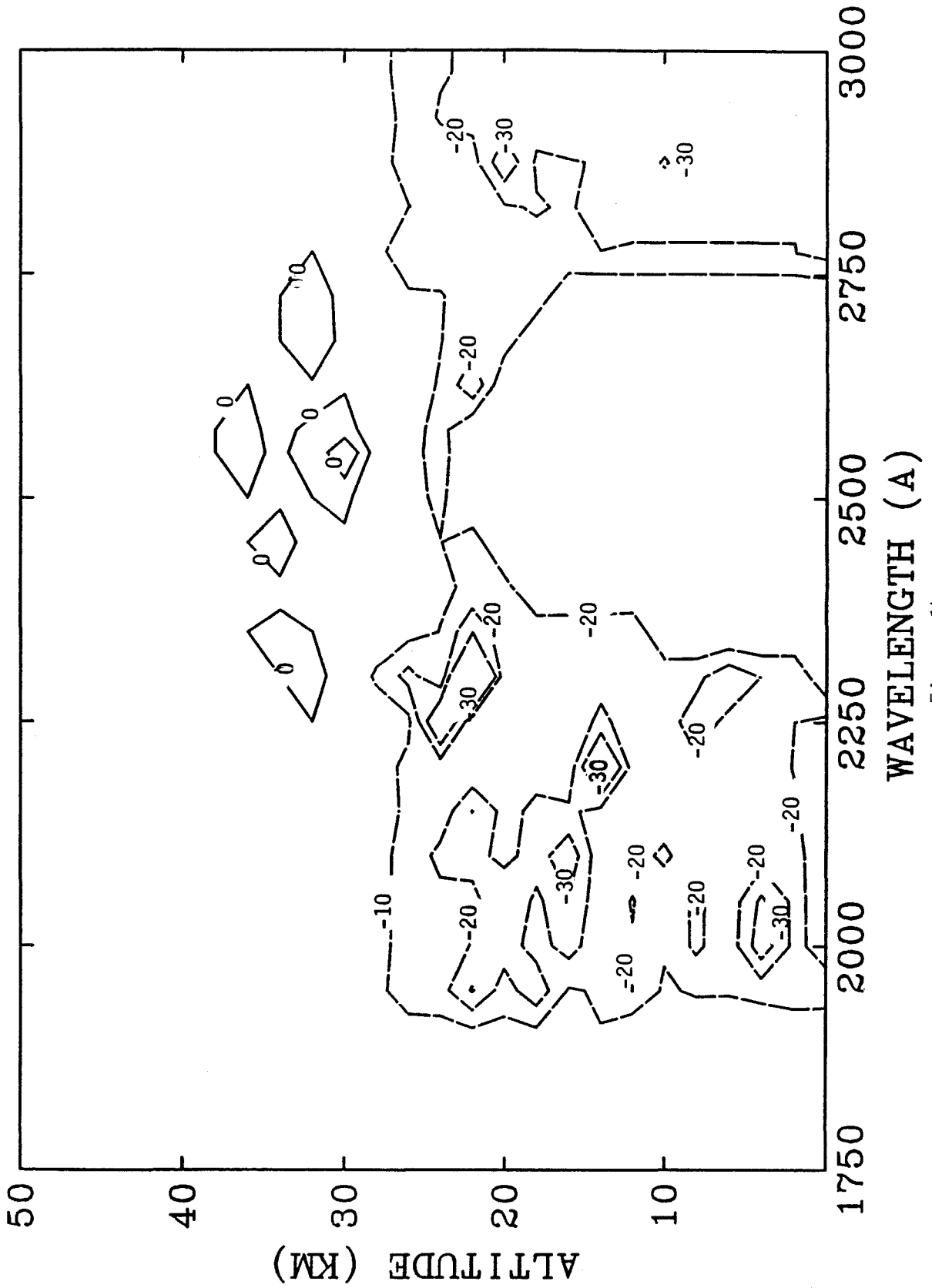
Figure 1b
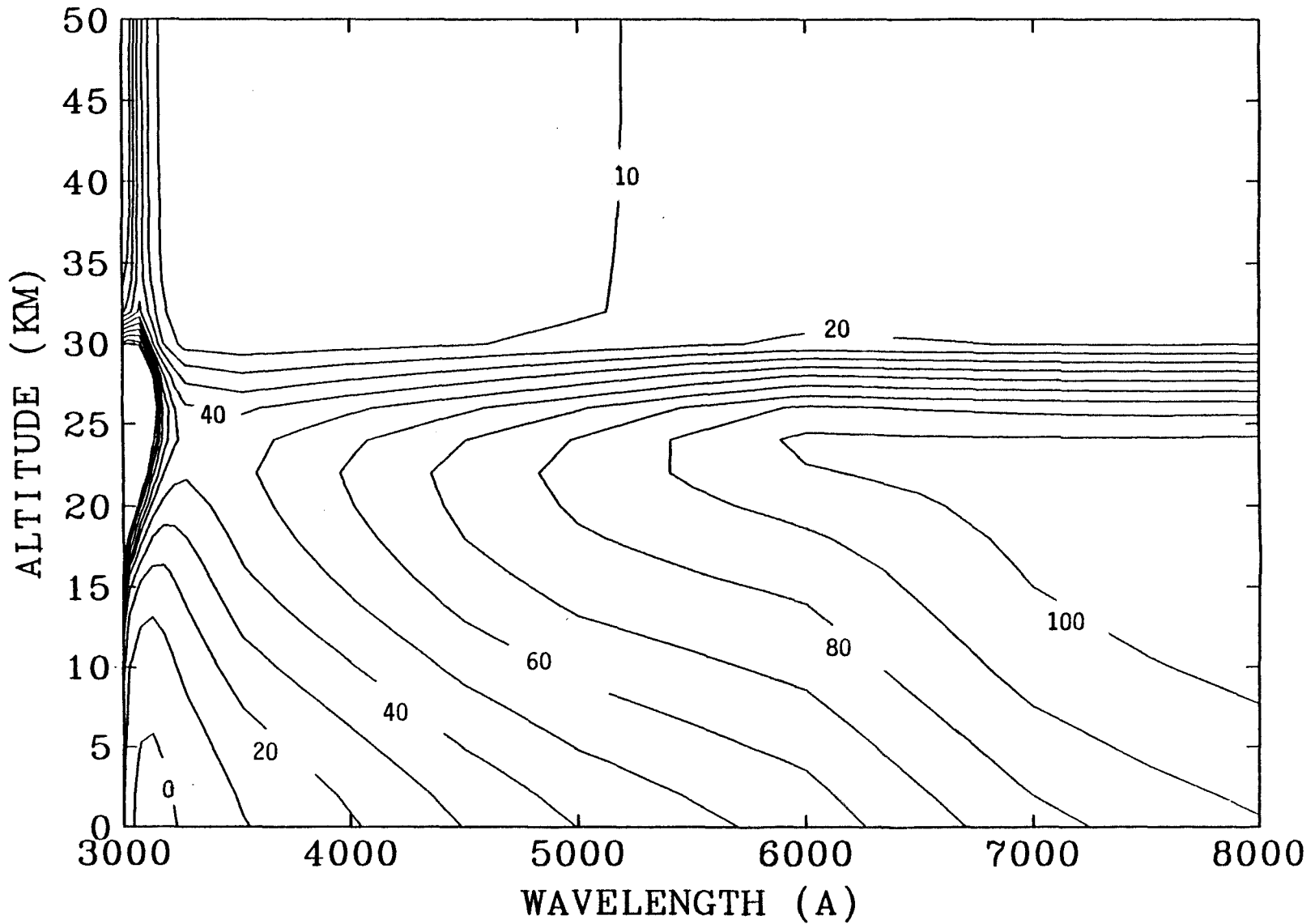
Figure 2a
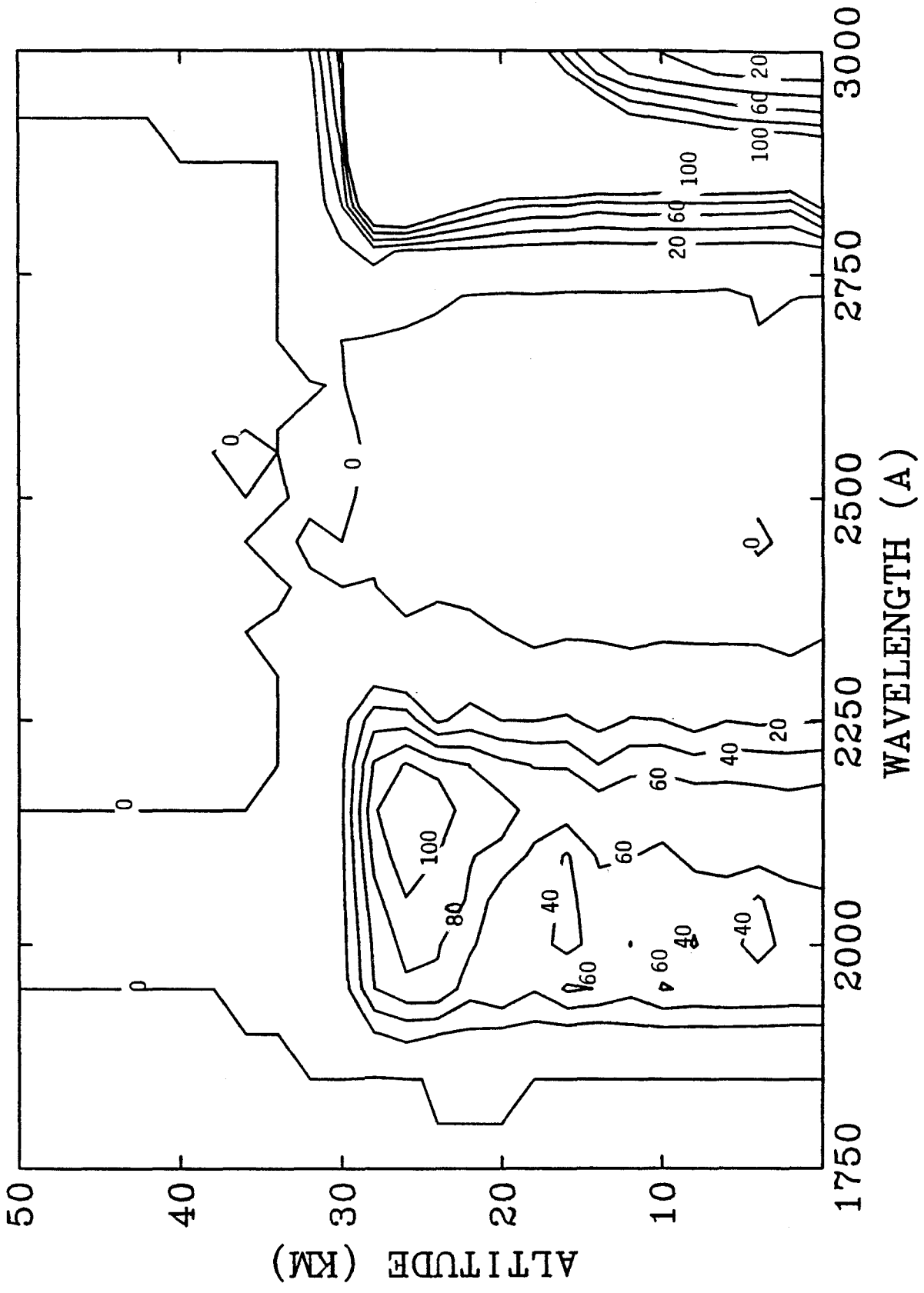
Figure 2b
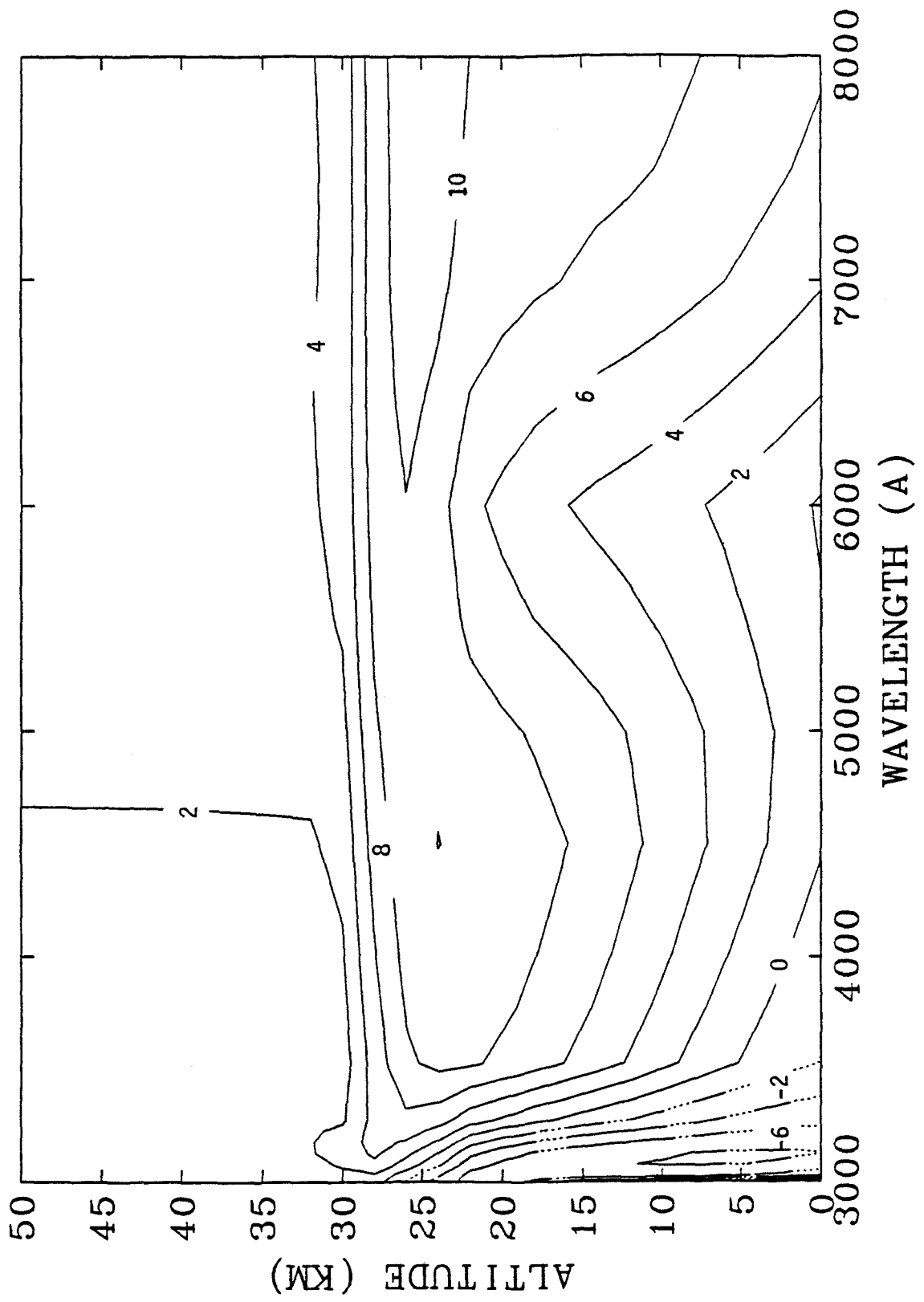
Figure 3a
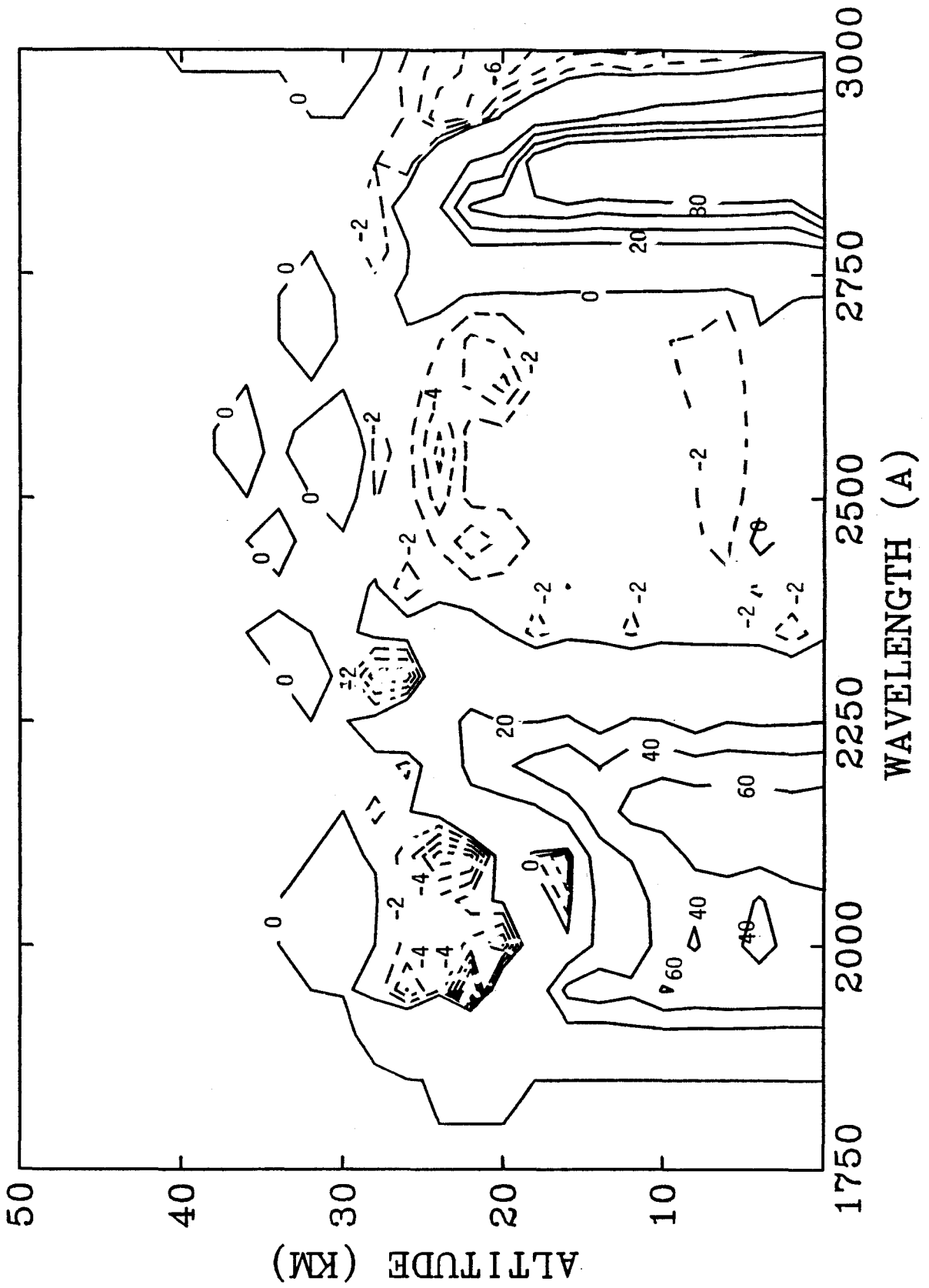
Figure 3b

## 1.3  Photochemical Model

We used the one-dimensional stratospheric chemistry model described by Froidevaux *et al.* (1985), in which chemical production and loss is coupled to transport, parameterized by the eddy diffusion coefficient. The rate constants used in the calculations are similar to those adopted by Froidevaux *et al.* (1985). Tables 1(a) and 1(b) contain the reactions with updated rate constants as well as additional reactions refered to in the text. The boundary conditions are identical to those in Froidevaux *et al.* (1985). A change to the 1985 model is the extention to 1750 Å of the shortward wavelength cutoff for the inclusion of the diffuse radiation field.

The background model atmosphere used is that of the U.S. Standard Atmosphere 1976. The latitude ($20°N$) and season (summer solstice) are chosen to correspond to the position and date of the aerosol observations used in our calculations and certain species measurements. The water-vapor mixing ratio is fixed from 0 to 16 km. All calculations are performed from 0 to 80 km and 0 to 60 km for diurnally averaged and diurnally varying radiation fields, respectively.

The calculations are run to a steady-state, even though the observations were made three months after the injection of $SO_2$ into the stratosphere. We are able to make this steady-state approximation, because, by comparing our results to runs marched forward in time by three months, the differences are small ($<2\%$). This simplification enables us to perform the calculations using a diurnally varying radiation field, while marching forward in time until convergence ($<2\%$ difference in concentrations from day to day).

Five basic cases were studied, starting with a standard, "clear" steady-state

atmosphere, to which we compare all other calculations. The second case considered the radiative effects of the aerosols, while the third case investigated the combined effects of the radiation change and the temperature variation. For all subsequent cases, the calculation of the diurnally varying radiation field was not included, since the hypotheses under investigation were more speculative. The calculations that included injections of $Cl_2$, HCl or $H_2O$ were marched forward in time for three months, because at steady–state, all the effect of a one–time event would dissappear. Finally, all calculations involving heterogeneous reactions also included the radiation and the temperature variations, and were steady state, diurnal average runs.

An important issue in doing these calculations is the question of whether or not a one–dimensional representation is valid. We have compared our calculations to observations three months after the eruption. In this region of the stratosphere, the mixing time scale is about 4–6 months (Rosenfield $et$ $al.$, 1987) from equator to pole. Vertical transport, by eddy diffusion, has a time scale of 1.4 years at 26 km. This is longer than the time scale of 1–3 months for $[O_x] = [O]+[O_3]$ to reach equilibrium (Brasseur and Solomon, 1984). It is clear that transport is not important and that local chemistry dominates and that therefore, our one-dimensional model is valid between 25 and 50 km for the first three months.

## TABLE 1(a): Partial List of Photochemical Reactions

| Reaction Number* | Reactions | | |
|---|---|---|---|
| 3 | $O_3 + h\nu$ | $\rightarrow$ | $O_2 + O$ |
| 4 | $O_3 + h\nu$ | $\rightarrow$ | $O_2 + O^1D$ |
| 6 | $H_2O_2 + h\nu$ | $\rightarrow$ | $2OH$ |
| 8 | $NO + h\nu$ | $\rightarrow$ | $N + O$ |
| 9 | $NO_2 + h\nu$ | $\rightarrow$ | $NO + O$ |
| 10 | $NO_3 + h\nu$ | $\rightarrow$ | $NO_2 + O$ |
| 11 | $NO_3 + h\nu$ | $\rightarrow$ | $NO + O_2$ |
| 12 | $N_2O_5 + h\nu$ | $\rightarrow$ | $2NO_2 + O$ |
| 23 | $ClNO_3 + h\nu$ | $\rightarrow$ | $Cl + NO_3$ |
| 24 | $HOCl + h\nu$ | $\rightarrow$ | $OH + Cl$ |
| 25 | $ClO + h\nu$ | $\rightarrow$ | $Cl + O$ |
| 26 | $HCl + h\nu$ | $\rightarrow$ | $H + Cl$ |

* All reaction numbers and cross section references correspond to those in Table IIb in Froidevaux *et al.* (1985).

## TABLE 1(b): Partial List of Chemical Reactions

| Reaction Number[*] | Reactions | | |
|---|---|---|---|
| 1 | $O + O_2 + M$ | $\rightarrow$ | $O_3 + M$ | |
| 29 | $OH + HO_2$ | $\rightarrow$ | $H_2O + O_2$ | ++ |
| 32 | $O + NO_2$ | $\rightarrow$ | $NO + O_2$ | |
| 33 | $O_3 + NO$ | $\rightarrow$ | $NO_2 + O_2$ | |
| 34 | $HO_2 + NO$ | $\rightarrow$ | $NO_2 + OH$ | |
| 35 | $NO + O + M$ | $\rightarrow$ | $NO_2 + M$ | ++ |
| 38 | $NO_3 + NO$ | $\rightarrow$ | $2NO_2$ | ++ |
| 40 | $NO_3 + NO_2 + M$ | $\rightarrow$ | $N_2O_5 + M$ | ++ |
| 46 | $OH + HNO_3$ | $\rightarrow$ | $NO_3 + H_2O$ | ++ |
| 47 | $HO_2 + NO_2 + M$ | $\rightarrow$ | $HO_2NO_2 + M$ | ++ |
| 54 | $Cl + O_3$ | $\rightarrow$ | $ClO + O_2$ | |
| 55 | $O + ClO$ | $\rightarrow$ | $Cl + O_2$ | ++ |
| 56 | $ClO + NO$ | $\rightarrow$ | $Cl + NO_2$ | |
| 57 | $ClO + OH$ | $\rightarrow$ | $Cl + HO_2$ | ++ |
| 58 | $Cl + O_2 + M$ | $\rightarrow$ | $ClOO + M$ | |
| 60 | $OH + HCl$ | $\rightarrow$ | $Cl + H_2O$ | ++ |
| 61 | $Cl + CH_4$ | $\rightarrow$ | $HCl + CH_3$ | |
| 74 | $CH_3 + O_2 + M$ | $\rightarrow$ | $CH_3O_2 + M$ | ++ |
| 77 | $CH_3O + O_2$ | $\rightarrow$ | $H_2CO + HO_2$ | ++ |
| 84 | $CH_3OOH + OH$ | $\rightarrow$ | $CH_3O_2 + H_2O$ | ++ |
| 88 | $OH + C_2H_2$ | $\rightarrow$ | products | ++ |
| 89 | $OH + C_2H_6$ | $\rightarrow$ | $H_2O + products$ | ++ |

---

* All reaction numbers correspond to those in Table IIa in Froidevaux *et al.* (1985).

++ Reactions for which the rate constants have been updated using the values from DeMore *et al.* (1985); all others were taken from Froidevaux *et al.* (1985).

## 1.4  Results of Photochemical Calculations

### 1.4.1    Photodissociation Rates

The diffuse fluxes obtained from the detailed radiative transfer calculations are entered into the photochemical model. This change in radiation field causes the photodissociation coefficients ($J$ values) to increase by as much as 10% or to decrease by 15 % in some cases. All photodissociation rate constants that changed by more than 1% are reported in Figures 4a, b, and c. Not all species respond to the change in radiation field in the same way. The absorption cross section of $NO_2$ peaks ($7 \times 10^{-19}$ cm$^2$) near 4000 Å, and that of $ClNO_3$ is large ($10^{-22}$–$10^{-19}$ cm$^2$) between 3000 and 4500 Å. $N_2O_5$ absorbs strongly up to 3825 Å. These species are the most affected by any change in the radiation below 4000 Å (see Figures 4b and 4c). $O_3$ (Chappuis bands), and $NO_3$, whose peak cross section ($4.9 \times 10^{-18}$ cm$^2$) occurs at 5900 Å, are sensitive to a variation in the radiation field, between 4000 and 8000 Å (see Figures 4a and 4b). The same is true for $HOCl$, whose absorption extends out to 4200 Å (Fig. 4c). $ClO$ and $H_2O_2$ dissociate below 3425 Å and 3525 Å, respectively, and will be only slightly affected by the change in the flux in the visible region of the spectrum (Figs. 4a, 4c). In Figures 4a, b and c we can see clearly that the highest increase in the photodissociation coefficients occurs for the species with the highest absorption cross sections between 3000 and 8000 Å.

The species whose photodissociation rate constants decrease ($H_2O$, $NO$, $HNO_3$, $HCl$) have their peak absorption cross section below 3000 Å, where the total radiation decreases by up to 15% within the aerosol layer. More specifically, $NO$ and $H_2O$ have large absorption cross sections up to 2000 Å, where the total radiation

decreases by 15% above 15 km. HCl absorbs shortward of 2300 Å, where the total radiation also decreases by 15%. In these three cases, the photodissociation rate constants decrease by up to 15% from 15 to 30 km. For $HNO_3$, the absorption ranges from 1900 to 3275 Å, covering a wide wavelength region of increasing and decreasing total radiation. Therefore, the decrease in the photodissociation rate constant is only 7%. Also the decrease is limited to the 20–30 km region, because the peak in $HNO_3$ concentration is above 20 km.

In contrast with our large change in $O_3$ photodissociation rate constant, Adriani et al. (1987) obtained a 1% increase at 20°N. This small change is due to the fact that the aerosol data used were taken in December 1982, nine months after the eruption, when the optical depth had decreased substantially because of coagulation and fallout of the aerosols. It is therefore not surprising that they obtain very little change in ozone concentration (<1%).

Figure 4. The percent difference (as defined in Figure 1) in the photodissociation rate constants as a function of altitude (km) for a local time of 2 p.m (solar zenith angle of 45°) for a) $H_2O$, $H_2O_2$, and $O_3 \rightarrow O + O^1D$, b) NO, $NO_2$, $HNO_3$, $N_2O_5$, and $NO_3 \rightarrow NO + NO_2$, and c) HCl, ClO, HOCl, and $ClNO_3$.
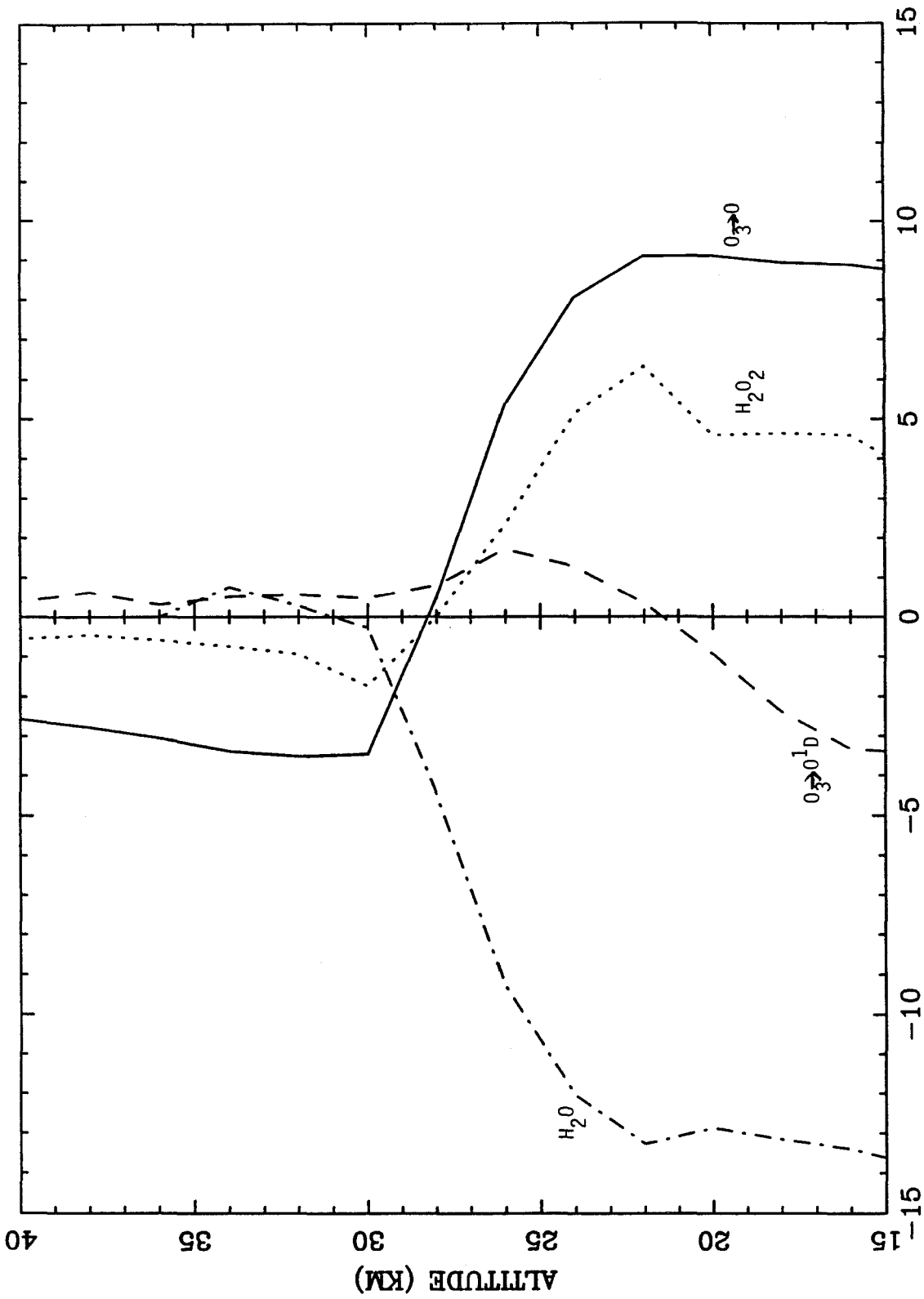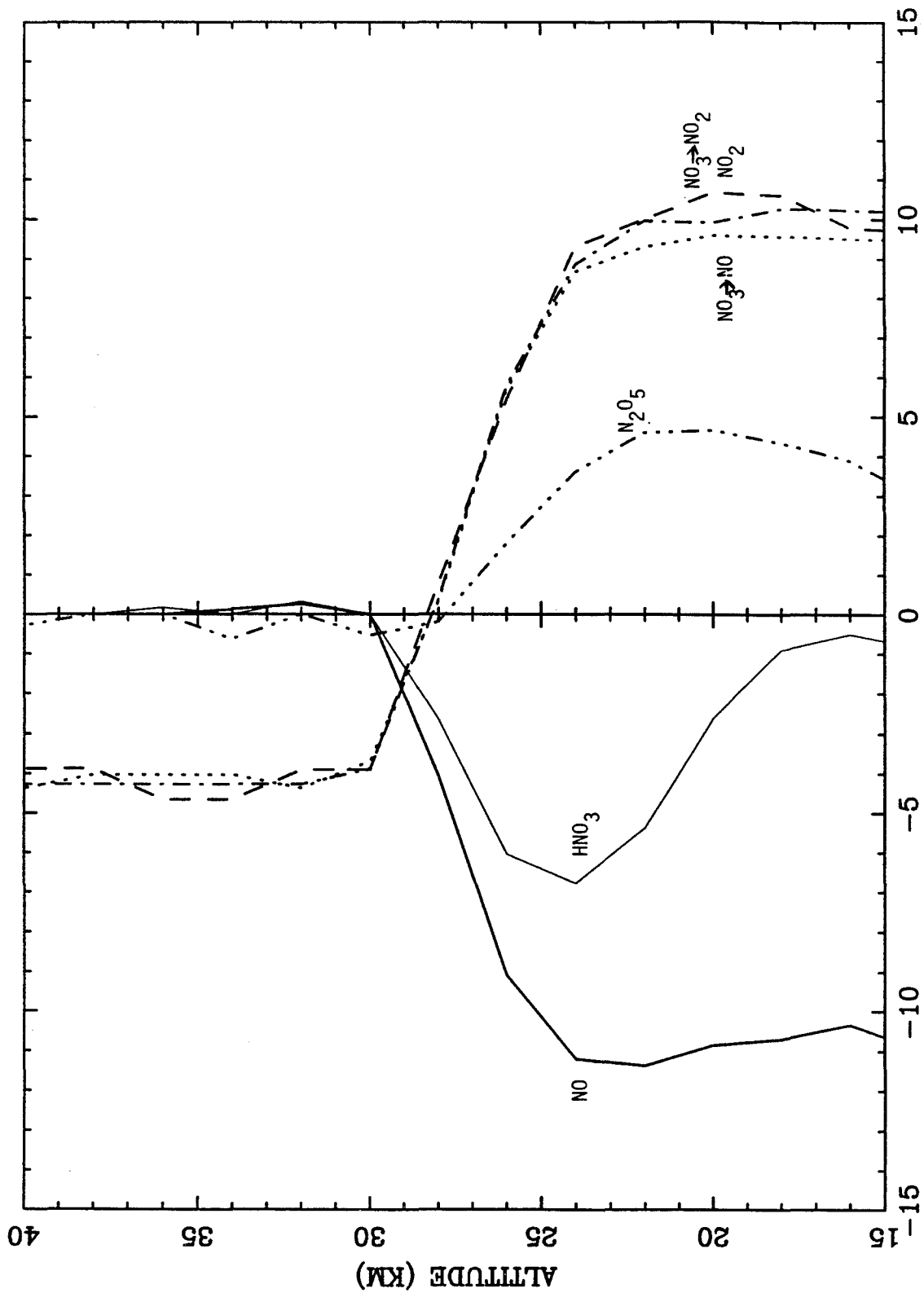
% DIFFERENCE

Figure 4a
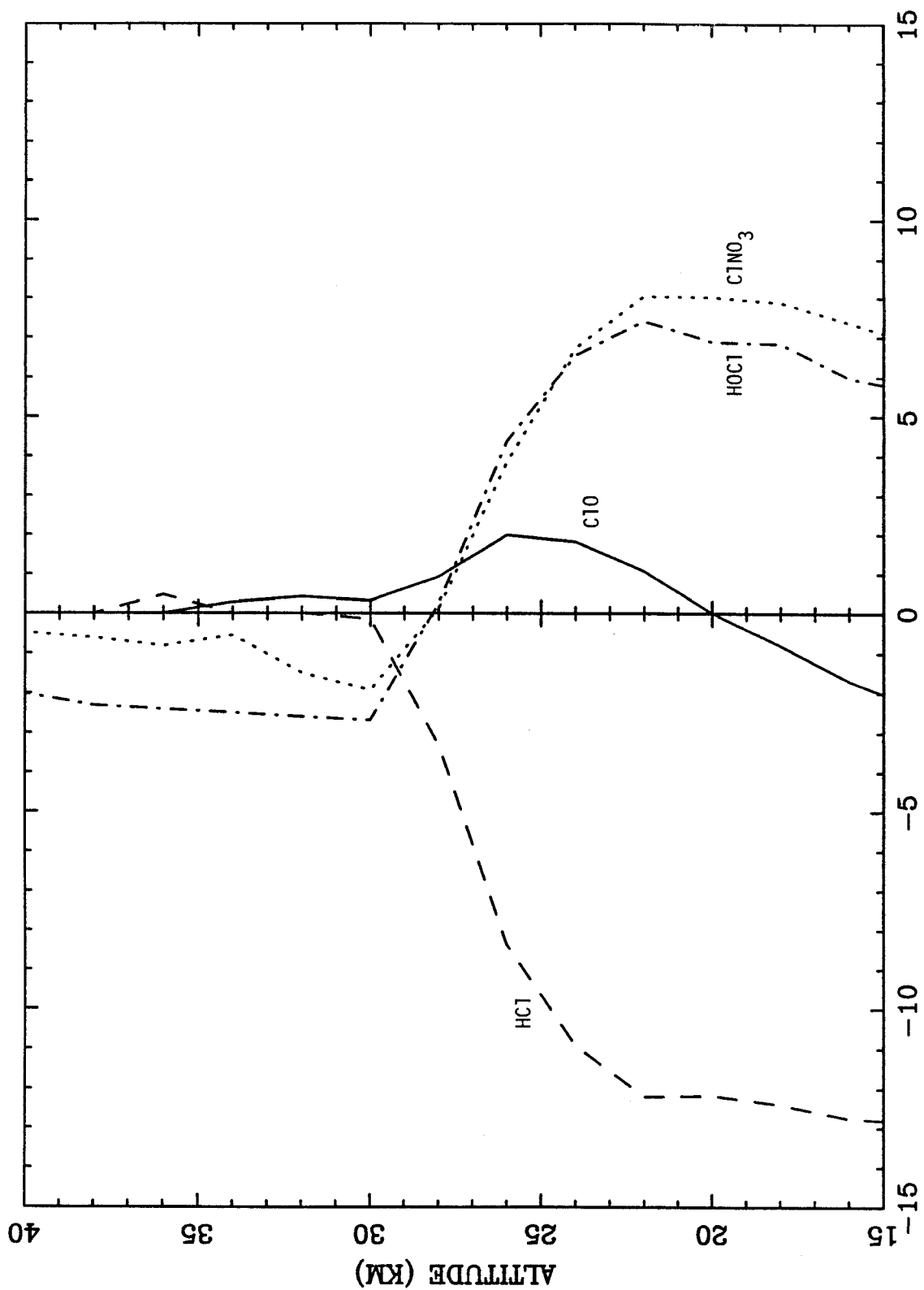
Figure 4b

Figure 4c

## 1.4.2   Concentration Changes

Because of the changes in photodissociation rate constants, the abundances of certain molecules changed. While changes in column abundances between 0 and 60 km were small, when we focus our attention on specific altitude levels, in particular within the aerosol layer, larger variations can occur (Figs. 5–10). We chose to report the concentration results at 2 p.m., corresponding to the solar zenith angle ($45°$), chosen for the figures of radiation changes (Figs. 1, 2, and 3).

The ozone abundance is controlled by the four radical groups: $O_x$, $HO_x$, $NO_x$, and $ClO_x$ (Brasseur and Solomon, 1984). The relative importance of each depends on the altitude. In the stratosphere, the ozone formation is via R1, while its loss is through photodissociation ($J_3$ and $J_4$). The $[O]/[O_3]$ ratio described by the equation

$$\frac{[O]}{[O_3]} = \frac{J_3 + J_4}{k_1[O_2][M]}$$

increases by 3.5% at 26 km and 2 p.m, because $J_3 + J_4$ increases by 3.5% (Fig. 4a), while $k_1$, $[O_2]$, and $[M]$ remain unchanged when the aerosols are added, resulting in an $O_3$ decrease of 2.6%..

The atomic oxygen released from $O_3$ dissociation reacts with $NO_2$ as in reaction R32,

$$O + NO_2 \;\rightarrow\; NO + O_2 \quad , \tag{R32}$$

which is the rate–determining step for the $NO_x$ cycle (Johnston and Podolske, 1978). Thus, NO increases because of increased photodissociation of $NO_2$ (Fig. 4b) and increased reaction of $NO_2$ with O (R32). The NO also contributes to the $O_3$

decrease between 16 and 30 km through R33.

$$O_3 + NO \rightarrow NO_2 + O_2 \quad . \tag{R33}$$

The ratio

$$\frac{[NO_2]}{[NO]} = \frac{k_{33}[O_3]}{J_9 + k_{32}[O]}$$

decreases by 10.7% at 24 km. This is due to the 10% increase of $J_9$ and $[O]$ as well as the lower $[O_3]$ (Fig. 5), while $k_{33}$ and $k_{32}$ are unchanged.

It is important to consider any effect that the increase in the stratospheric temperature observed after the eruption would have on the chemical reactions. For this reason, we repeated the calculations of concentrations and photolysis rates as described above, but also included a temperature variation within the aerosol layer, as calculated by Pollack and Ackerman (1983). The change ranges from $+0.9°$C at 14 km, to $+3.2°$ C at 24 km, and back down to $-3.1°$ C at 38 km, above which the temperature did not change. The decrease above 30 km is probably an overestimate of the change in temperature. Because of the lack of data in this region, we should not put too much importance on the results above 30 km. The results (Figs. 5–10) show that the temperature change has a significant effect. There are substantial differences in the percent changes for the species whose concentrations are primarily determined by non–photochemical processes, such as $O_3$, $HO_2$, $NO$, $NO_2$, $NO_3$, $ClO$, and $ClNO_3$.

By simply adding the temperature perturbation to our model, we obtain a 5.8% decrease in ozone at 26 km. The only reaction for the formation of ozone is R1,

$$O + O_2 + M \rightarrow O_3 + M \quad , \tag{R1}$$
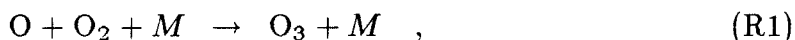
which has a negative, temperature–dependent rate constant. Therefore, increasing the stratospheric temperature by a few degrees decreases the rate constant of R1

by 3.5%, and therefore decreases the total $O_3$ even more than with the radiation change alone. (The $[O]/[O_3]$ ratio becomes larger with smaller $k_1$.) This agrees with the results of Adriani $et$ $al.$ (1987), who also conclude that a small temperature perturbation will increase the ozone loss.

$O^1D$ and $HO_2$ are directly affected by the decrease in ozone, while OH responds to the NO increase. The NO, $NO_2$, and $NO_3$ are mostly affected by photodissociation changes, while $HNO_3$ is controlled by the OH increase. The concentrations are affected by temperature via the temperature–dependent rate constants in a straightforward way.

For the chlorine species, the mechanism is somewhat simpler than for ozone. The atomic chlorine partitions itself between the major reservoir species $ClNO_3$, HOCl, and HCl. The first has a weak $Cl–ONO_2$ bond (20 Kcal/mole), and dissociates easily at long wavelengths (up to 4500 Å). HOCl is also weakly bounded and dissociates shortward of 4200 Å. The aerosols have the effect of increasing the total radiation by about 10% at these wavelengths. Therefore, the photodissociation rate constants for $ClNO_3$ and HOCl increase by 8 and 7%, respectively, at 26 km (Fig. 4c). As a consequence, the abundances of $ClNO_3$ and HOCl drop by 8 and 7%, respectively, at 26 km, and the Cl liberated reacts with methane to form HCl (R61), which increases by 6% at 26 km,

$$Cl + CH_4 \quad \rightarrow \quad HCl + CH_3 \quad . \tag{R61}$$

The only other important reactions that might destroy Cl are

$$Cl + O_2 + M \quad \rightarrow \quad ClO_2 + M \tag{R58}$$

and

$$Cl + O_3 \quad \rightarrow \quad ClO + O_2 \quad . \tag{R54}$$

The $ClO_2$ is rapidly converted back to Cl by the reverse reaction of R58, and therefore is unimportant, and the loss of ClO occurs via the fast reaction

$$ClO + NO \rightarrow Cl + NO_2, \qquad (R56)$$
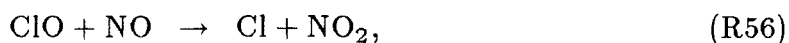
which regenerates the Cl, which then reacts with $CH_4$ to form HCl (R61).

The total of $[ClNO_3] + [HOCl] + [HCl]$ remains constant; therefore, the changes are due strictly to a "reshuffling" of the chlorine between its reservoirs. The methane does not show any change because its concentration is much larger than that of HCl. Hydrochloric acid does not dissociate at wavelengths longer than 2300 Å. Below this level there is a decrease in the radiation from 16 to 30 km. Its photodissociation rate constant actually decreases, contributing to the HCl increase. This contribution is not very large, since the photodissociation is not the major loss process of the HCl at these altitudes. The ClO does not play an important role in this mechanism, because its photodissociation rate constant does not change a great deal (Fig. 4c).

The temperature perturbation enhances the HCl change to 10%, because of the positive temperature dependence of R61, increasing the production of HCl in the cloud, where the temperature increases. The ClO increase, due to the positive temperature dependence of R54, leads to an HOCl increase.

The concentrations of the freons in our model do not show any appreciable change. On the other hand, the hydrocarbons ($C_2H_2$, $C_2H_6$, $C_3H_8$) decrease by more than 50% above 16 km. This is due mainly to the increases in Cl and OH and to the small abundances of the hydrocarbons.

Figure 5. The percent difference in the concentrations of O, $O(^1D)$, $O_3$ as a function of altitude (km) for a local time of 2 p.m. (solar zenith angle of 45°) for species noted. The curves identified by a * represent the results when the temperature perturbation was added to the radiation change.

Figure 6. Same as Figure 5 except for OH, $HO_2$, $H_2O_2$.

Figure 7. Same as Figure 5 except for NO, $NO_2$, $NO_3$.

Figure 8. Same as Figure 5 except for $N_2O_5$, $HNO_3$, $HO_2NO_2$.

Figure 9. Same as Figure 5 except for Cl, ClO, $ClO_2$.

Figure 10. Same as Figure 5 except for HCl, HOCl, $ClNO_3$.
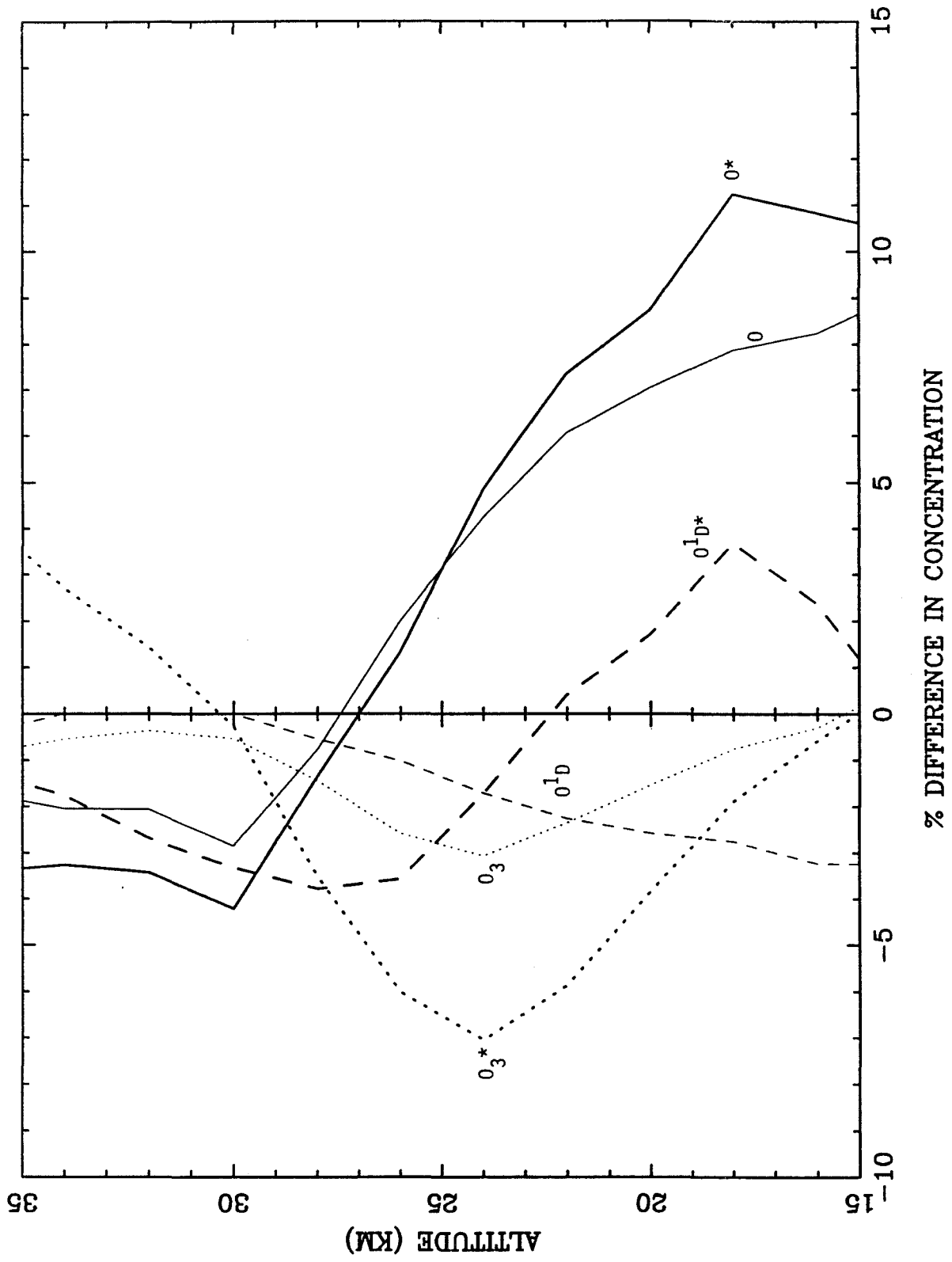
Figure 5
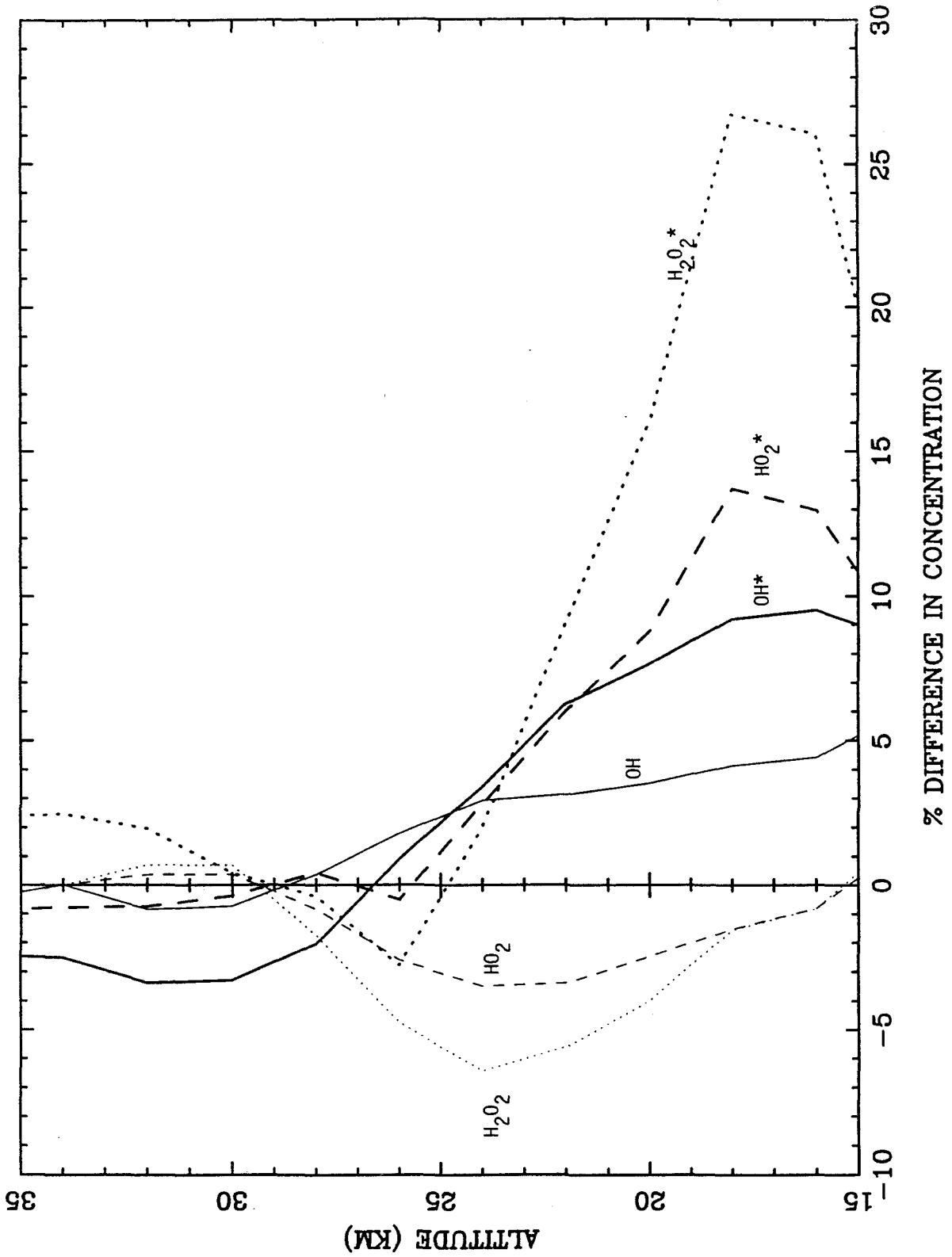
Figure 6
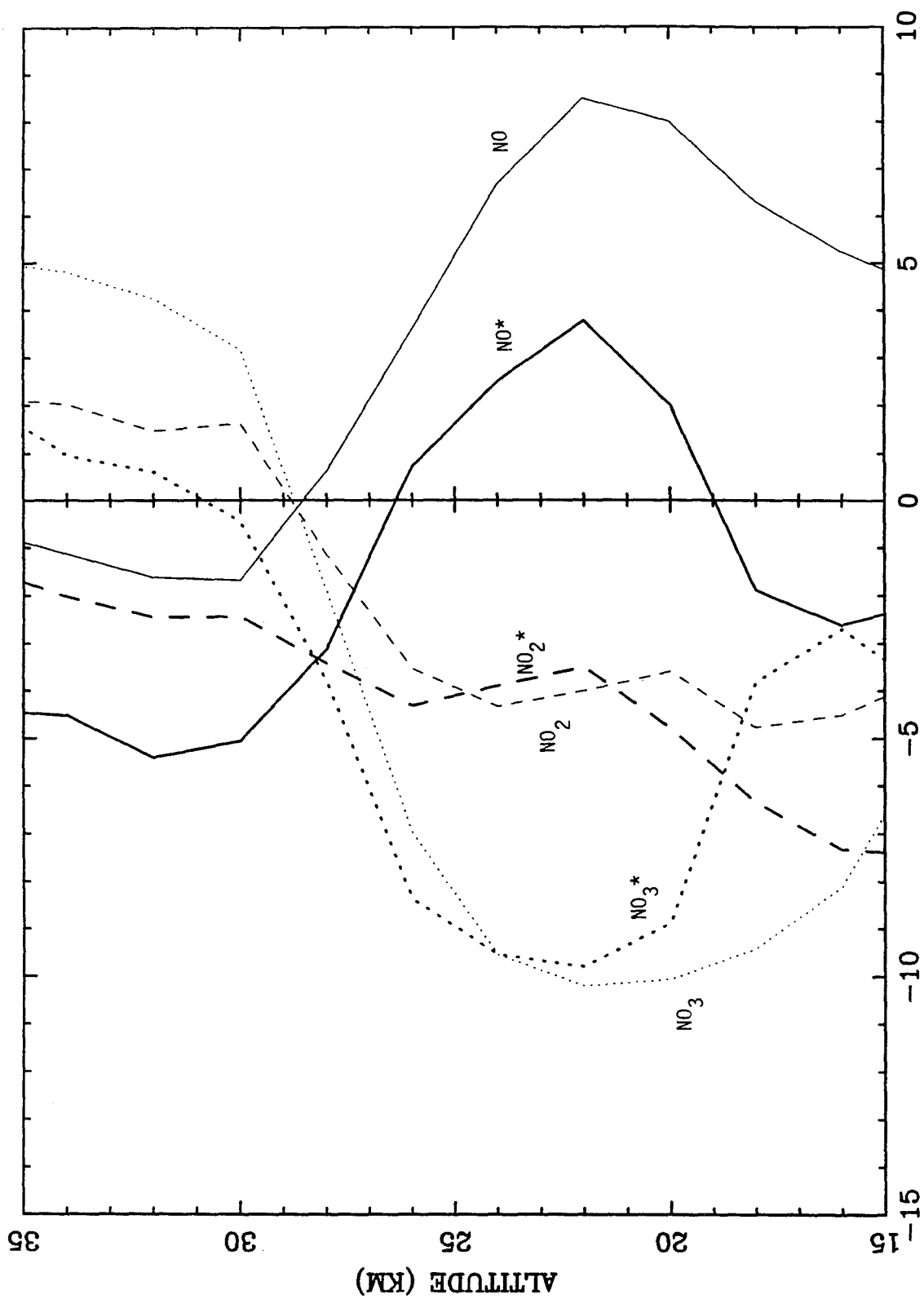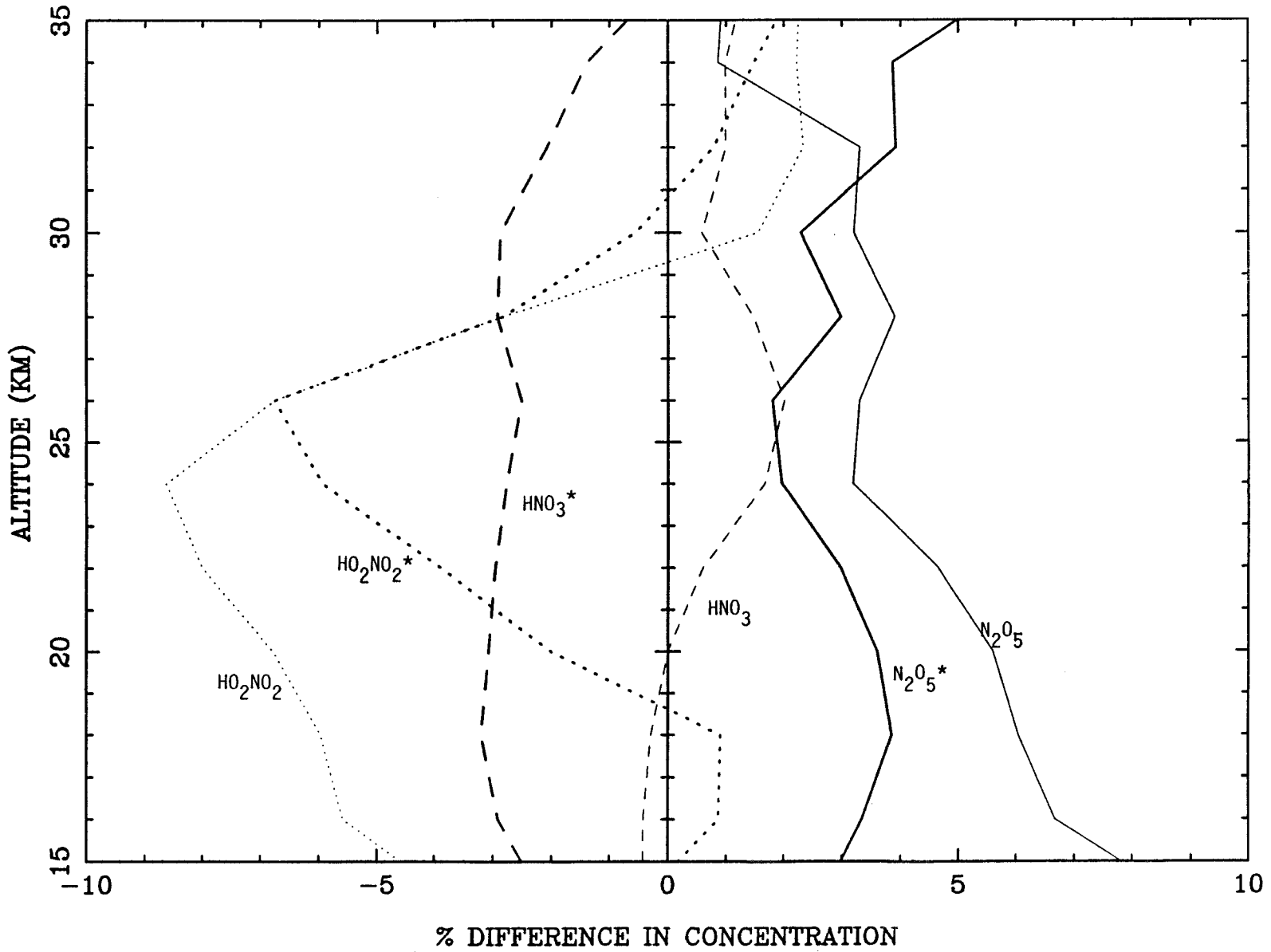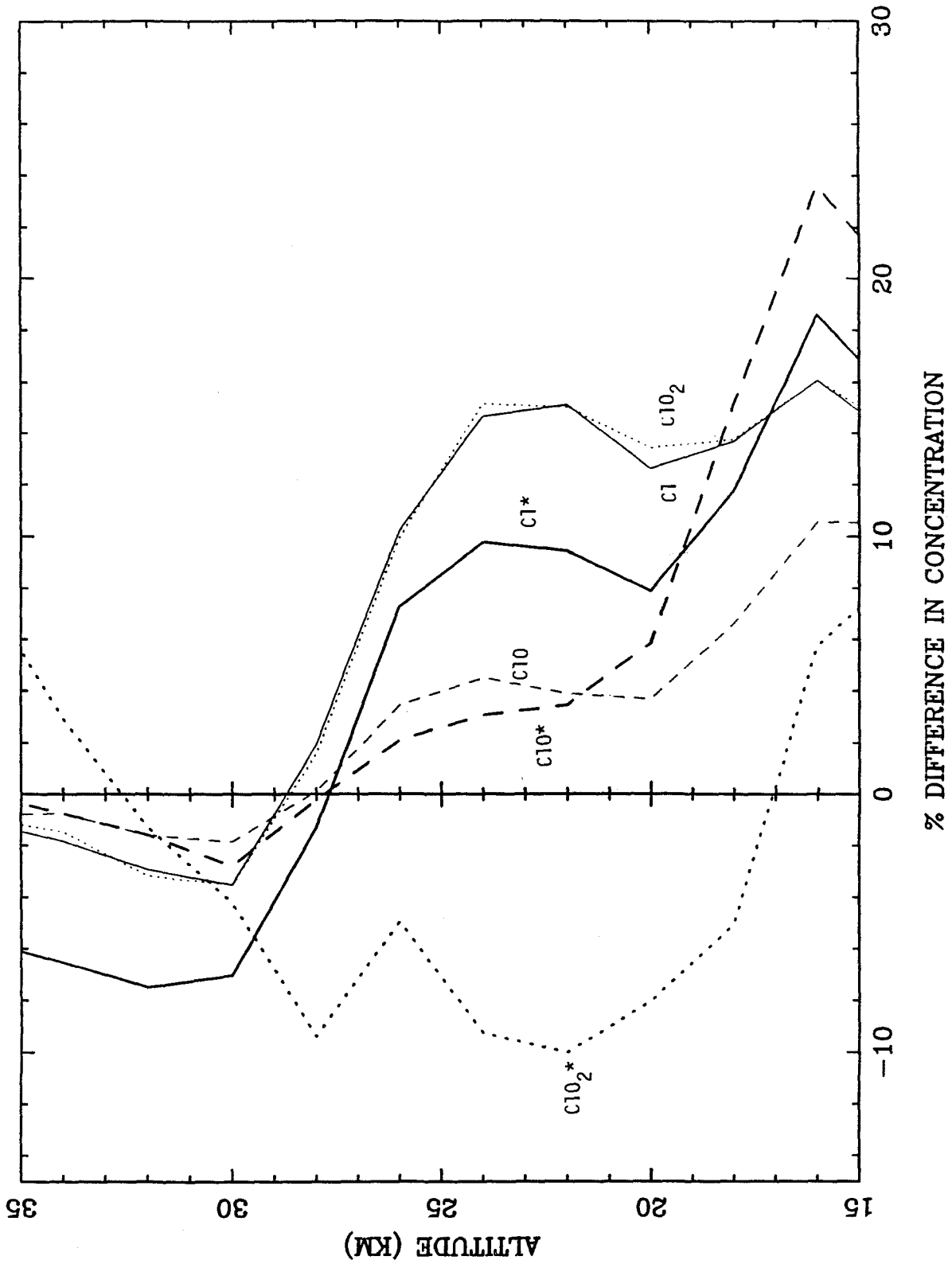
Figure 7

Figure 8

Figure 9
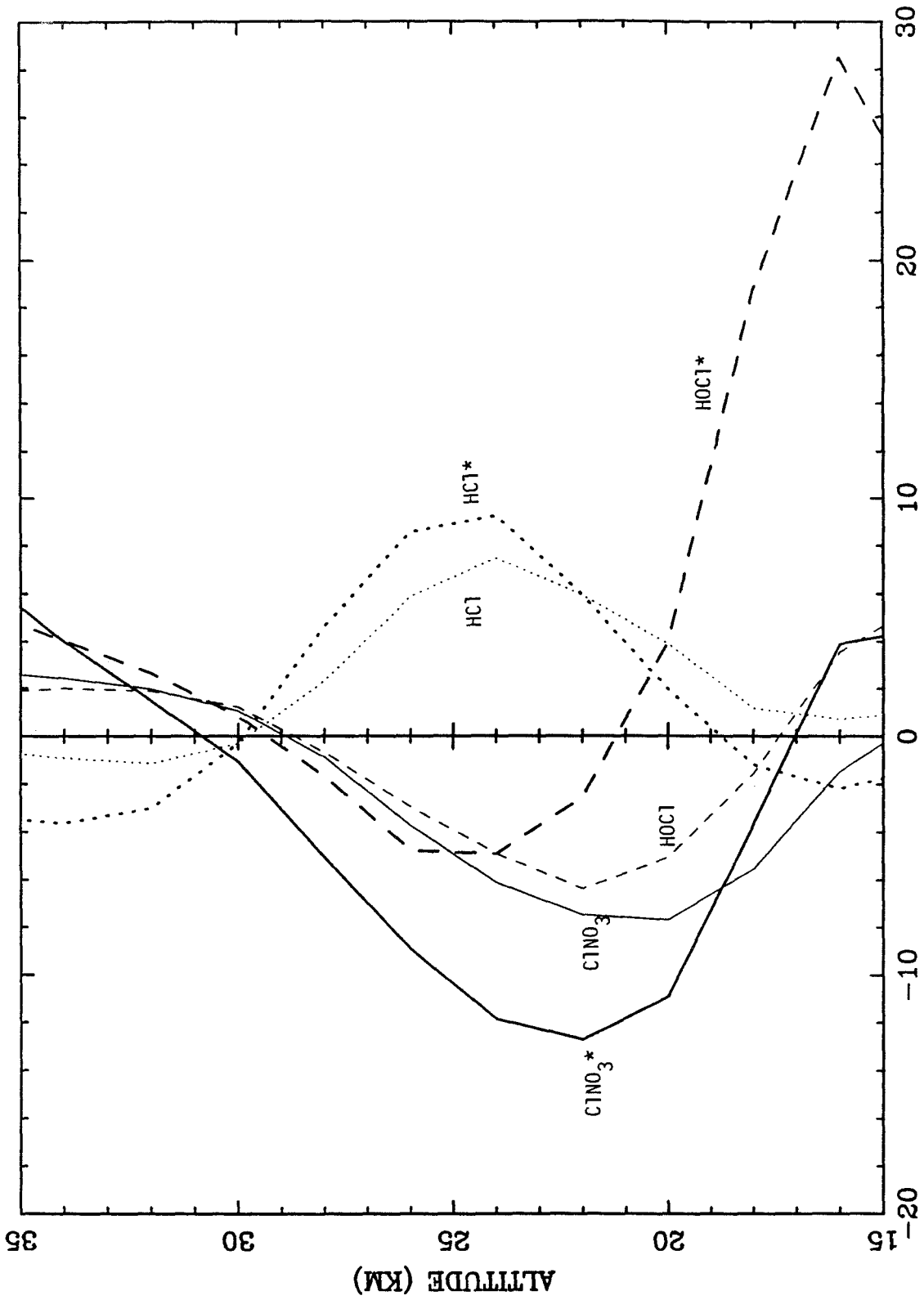
Figure 10

## 1.5  Comparison with Observations

Our discussion will now focus on the species for which we have relevant observations: $O_3$, HCl, $NO_2$, NO, and OH. We have specifically chosen measurements taken near 20°N and 3–6 months after the eruption of the volcano. We also required that the same instrument measure the abundance of the species before and after the eruption. Therefore, even though there were many observations after April 1982, we limit our comparisons to the measurements summarized in Table 2.

### 1.5.1  Ozone

Heath and Schlesinger (1984) reported a 6% and 13% decrease in $O_3$ concentration at 24 and 30 km, respectively, at 20°N in June–July, 1982. Chandra (1987), also analyzing the SBUV data, found a decrease of 4–6% at 20°N, 25 km, in June–July 1982. Komhyr et al. (1985) reported an ozone deficiency near 25 km, in Hilo, Hawaii. DeLuisi et al. (1985) obtained an ozone decrease after analyzing Umkher data. Chandra (1987) also presented results of a 2–3% decrease at higher latitudes (50°N), which he compared to Dobson measurements and theoretical calculations by Adriani et al. (1987).

Unfortunately, the evidence for an ozone depletion after the eruption is not completely convincing. There was no unusual variation noticed at low latitudes, where the aerosol cloud was the thickest for the longest period of time. Both Heath and Schlesinger (1984) and Chandra (1987), analyzing the SBUV data, had to consider the uncertainty in evaluating the contribution of the aerosols to their signal. A comparison of SME (Solar Mesospheric Explorer) and SBUV radiances led Clancy

(1988) to suggest that ozone increased above 35 km, contrary to the assessment of Chandra (1987). It is also crucial to determine the effect of the quasi–biennial oscillation (QBO) (see for example, Mantis et al., 1986). Komhyr et al. believe this to be the main cause for their observed ozone decrease. Angell et al. (1985) show that the ozone reduction was greater than expected from QBO variations. On the other hand, it seems clear from the correlation between aerosol maximum and ozone depletion (Bais et al., 1985) that a volcanic effect is present. Therefore, a few percent decrease in ozone between 25 and 30 km, at 20°N, in June–July 1982 seems to be a reasonable conclusion of the volcanic impact. Fortunately, this agrees well with our estimates of the ozone concentration changes: at 26 km, a 3.5% decrease with the new radiation field, and a 7.0% decrease with the temperature perturbation (see Table 2).

TABLE 2: Observations of Species after the
Eruption of the Volcano and Model Calculation Results

| Species | Observation | | | Model | | |
| | Altitude | Change | Reference | Altitude | + Radiation | + Radiation + Temperature |
|---|---|---|---|---|---|---|
| $O_3$ | 24–30 km 25 km | −6–10% −4.6% | Heath (1984) Chandra (1987) DeLuisi (1985) Komhyr (1985) | 24 km | −3.0% | −7% |
| HCl | 21.6– 27.4 km column above 12 km | +30–40% +40% | Gandrud and Lazrus (1983) Mankin and Coffey (1984) | 24 km column above 12 km | +8% +2.7% | +10% +1.7% |
| NO | 30 km | −75% | Roscoe *et al.* (1986) | 30 km | −2% | −5% |
| $NO_2$ | 25–32 km | −50% | Roscoe *et al.* (1986) | 25 km | −3.5% | −4% |
| $NO + NO_2$ | column above 12 km | −50% | Mankin and Coffey (1986) | column above 12 km | −0.03% | −2.8% |
| $HNO_3$ | column above 12 km | ~0% | Mankin and Coffey (1986) | column above 12 km | +0.5% | −2.9% |
| OH | column above 0 km | +35% | Burnett and Burnett (1983) | column above 0 km | −0.1% | −0.8% |

## 1.5.2    HCl and chlorine injection

Mankin and Coffey (1984) reported a hydrogen chloride column increase of approximately 40% above 12 km, from 20° to 40°N latitude in September, 1982, which they attributed to direct injection of chlorine from the volcano. Also, Gandrud and Lazrus (1983) reported a 30–40% HCl increase from 21.6 to 27.4 km (32°52'N and 105°57'W) in August, 1982, from *in situ* measurements. Our maximum increase in HCl is 10% at 24 km with the temperature perturbation, which is low compared with the observations of Gandrud and Lazrus (1983) (Table 2). To compare our results to those of Mankin and Coffey (1984), we evaluated our HCl column abundance above 12 km and found a 2.0% increase, with the temperature effect. This is not enough to match the observations (Table 2). Mankin and Coffey (1984) suggest that there was a direct injection of chlorine from the volcano into the stratosphere. This was substantiated by the fact that many volcanoes are known to eject gases other than $SO_2$, such as $Cl_2$, HCl, or $H_2O$ (Cadle, 1975, 1980). Woods *et al.*, (1985) discussed the implications of the difference in NaCl concentrations they observed in the volcanic plume on April 15 and May 5, 1982. This argument was used to explain the observations of Mankin and Coffey (1984), and Gandrud and Lazrus (1983). We estimated the amount of Cl injected using the difference in halite concentrations in the volcanic plume measured by Woods *et al.* (1985). This implied that 500 ng.m$^{-3}$ of Cl were injected, resulting in a 0.2 ppb extra chlorine loading between 18 and 21 km. The extra Cl for other altitudes was estimated relative to the amount of aerosol at that level. The chlorine was first added to our model in the form of Cl atoms corresponding to a maximum HCl increase of 40% at 28 km. The calculations were performed as in the two previous cases, with aerosols as extra scatterers, and the temperature perturbation, but for a diurnally averaged radiation

field, and a three month time step instead of steady–state. This Cl amount makes very little impact on the HCl concentration. We can also assume that the volcano injected HCl directly into the stratosphere. In order to obtain a 40% increase in HCl at 28 km three months after the eruption, we need to consider an HCl column increase of 60% (or an even greater amount of $Cl_2$). The HCl injected reacts with OH (R60) to form Cl, which rapidly equilibrates with ClO (R54, R55). With normal atmospheric $NO_2$ concentrations, the formation of $ClNO_3$ is much faster than that of HCl. Therefore, $ClNO_3$ is preferentially formed when Cl or HCl is injected into the stratosphere. Besides this "chemical" loss of HCl, there is also a loss because of rainout in the troposphere. The large gradient in HCl concentration after the injection increases the downward flux of species. The rainout represents 70% of the loss of HCl when we consider a 60% column injection. This large injection is difficult to accept, since we have no basis for this conclusion. It is clear that we need good measurements of gaseous species that were injected into the stratosphere.

### 1.5.3 NO, $NO_2$, and $HNO_3$

Roscoe *et al.* (1986) measured large NO and $NO_2$ decreases above 30 km. They saw a maximum of 70% $NO_2$ decrease at 26 km, and of 75% in NO above 30 km (see Table 2). Also, Mankin and Coffey (1986) obtained a 50% decrease in the total $NO + NO_2$ column abundance above 12 km, but saw no change in $HNO_3$ (Table 2). The radiation and temperature changes produce only a few percent $NO_2$ decrease, a slight NO increase, and little $HNO_3$ change. It might be possible, on the other hand, to decrease the NO and $NO_2$ content of the atmosphere by a direct injection of $H_2O$ from the volcano. Thomas *et al.* (1983) suggested that there was less than 20% of the naturally occurring water injected into the stratosphere. On the

other hand, Roscoe *et al.* (1986) suggested that 20 ppmv of $H_2O$ should have been injected. This value agrees well with the estimate of water vapor injection made by Burnett and Burnett (1984), based on their OH measurements after the eruption. 20 ppmv of $H_2O$ added to our model bring the NO and $NO_2$ concentrations down by about 20% (after a three–month time step), but is still not sufficient to explain the observations.

McFarland *et al.* (1986) measured $[NO_2]/[NO]$ in Texas in July, 1982, and found that $([NO_2]/[NO])_{calculated}/([NO_2]/[NO])_{measured}$ varied from 0.7 to 1.3 from 20 to 30 km. (Their "calculated" ratio does not include the aerosol effect.) They obtained a ratio of 1.0 at 28 km. Our diurnal results produce the exact same trend at noon: a ratio of 0.9 and 1.05 below and above 28 km, respectively, when we take the "no aerosol" and "aerosol–containing" cases to be the "calculated" and "observed" cases, respectively. Unfortunately, this is not a strong constraint on the calculation.

### 1.5.4    OH and water injection

There have also been observations of a OH column (above the ground) abundance increase of 30% reported by Burnett and Burnett (1984) (Table 2). Unfortunately, these measurements were taken at a different latitude ($40°N$, $105°W$). Our calculations do not show any change in the column abundance of OH (Table 2). We do, however, observe a 6% increase at 24 km. The peak in the OH concentration is near 40 km; therefore, this 6% change should not affect overall column abundance. In any case, the volcanic aerosol layer extended only up to 30 km, so any change at 40 km, which would affect the column, has to be due to another mechanism. Also, McKeen *et al.* (1984) predicted a decrease in hydroxyl by a factor of 10 at

24 km and 20°N. If we take into account the chemical changes that are due to the increase in $SO_2$, as well as those caused by the optical depth changes, we do not obtain the results of Burnett and Burnett (1984). Adding the temperature effect does not significantly increase the OH change. Including 20 ppmv of water in our model produces a 20% OH increase at 24 km, but the column changes by only a few percent. In order to obtain a 30% column increase in OH, a much more substantial amount of water has to be injected around 40 km. This hypothesis seems unlikely. Also, any large OH increase has a direct impact on the HCl destruction. The inclusion of 20 ppmv of $H_2O$ leads to a 15% HCl loss, in contradiction with the observations.

There are two points that lead us to believe that we should not worry too much about this OH discrepancy. The first is that the measurements were made at 40°N, not at the latitude corresponding to our calculation (20°N). The second point is that Burnett and Burnett (private communication) suggested that they were located on the edge of the aerosol cloud, resulting in a "non-uniform" aerosol distribution, and in "unusual" chemistry in that region.

### 1.5.5    Heterogeneous reactions involving the volcanic aerosols

It is clear from the above discussion, and from Table 2, that problems remain regarding the explanations for the HCl, OH, NO, and $NO_2$ observations. The final explanation given for this discrepancy between the model and observations involves heterogeneous reactions on, or in, the sulfuric acid aerosols. There is a great deal of interest in these reactions because of their possible importance on the polar stratospheric clouds (PSC's) in the Antarctic spring destruction of ozone. To

solve the "ozone hole" problem, experimental physical chemists have focussed their attention on heterogeneous reactions on water ice surfaces (Molina *et al.*, 1987; Leu 1988) and on $H_2SO_4/H_2O$ drops (Rossi *et al.*, 1987). More precisely of interest for the volcanic aerosols, Rossi *et al.* (1987) investigated the reaction of chlorine nitrate on 95.6% $H_2SO_4$, which can be considered as a lower limit for the more aqueous aerosol, since as the aerosol contains more water it becomes more reactive as a catalyst. The results on pure $H_2O$ can be taken as upper limits.

We investigated the following heterogeneous reactions, which have been proposed to explain the antarctic ozone hole problem:

$$ClONO_2 + HCl \;\rightarrow\; Cl_2 + HNO_3 \tag{H1}$$

$$ClONO_2 + H_2O \;\rightarrow\; HOCl + HNO_3 \tag{H2}$$

$$ClONO_2 \;\rightarrow\; HCl + HNO_3 \quad * \tag{H3}$$

$$Cl \;\rightarrow\; HCl \quad * \tag{H4}$$

$$N_2O_5 + H_2O \;\rightarrow\; 2HNO_3 \tag{H5}$$
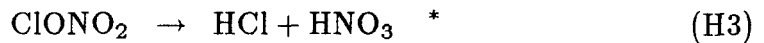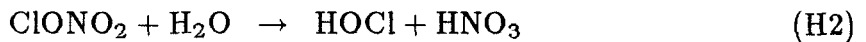
(*: unbalanced, speculated reactions in order to increase HCl directly.) In these reactions, the $H_2O$ and HCl are absorbed in the aerosols. All other molecules are in the gas phase. It is uncertain whether or not the $HNO_3$ would remain in the aerosol or escape the gas phase. Our model assumes that it is released. The experimental data regarding these reactions are very sparse.

The loss rate of a species because of the aerosols is:

$$J = \frac{1}{4}\gamma v A N_a$$

where $\gamma$ is the sticking coefficient, $v$ the thermal velocity of the gas ($3 \times 10^4$ cm s$^{-1}$), $A$ the mean surface area ($6.4 \times 10^{-8}$ cm$^2$, assuming that the geometrical

and optical cross sections are the same), and $N_a$, the number density of aerosols. At each altitude, and for various $\gamma$'s and each reaction, the loss rates are evaluated and entered into the program, with the scattering properties of the aerosols, as well as the temperature perturbation. The experiments on water ice give sticking coefficients near 0.02. This is a typical value used, which yields a first-order rate of $2.5 \times 10^{-4}$ s$^{-1}$ at the altitude of maximum aerosol concentration. It is important to keep in mind that this is an upper limit.

The results of the heterogeneous reactions studied are summarized in Table 3. It is important to note that all these calculations were performed in a diurnally averaged, time–marching mode until steady state was reached. The absolute concentrations of the "clear" case species are the same as in Froidevaux et al. (1985). (H1) is clearly unimportant, because even with a small ($10^{-4}$) sticking coefficient, all HCl is rapidly lost. This is in conflict with the observations of a large HCl increase after the eruption of the volcano. This result does not disprove the importance of (H1) on the PSC's, because the HCl is observed to decrease in the Antarctic stratosphere. Our conclusion for (H1) is that its sticking coefficient must be much smaller than $10^{-4}$ on sulfuric acid aerosols and is therefore unimportant in the atmosphere everywhere else but in Antarctica, where the aerosols have a different composition.

(H2) also decreases the HCl, because HOCl is more stable than ClNO$_3$; therefore, less Cl is released when it is in the HOCl form. On the other hand, this reaction is very efficient at reproducing the observed NO, NO$_2$, and OH changes with $\gamma = 0.02$. The large ozone decrease obtained might not contradict the observations, since there is still an uncertainty as to the exact volcanic effect measured. Besides the HCl change, which contradicts the observations, there is a huge increase in HNO$_3$, which is not confirmed by the measurements of Mankin and Coffey (1986).

TABLE 3: Percent changes in concentrations of species listed
when new radiation and temperature perturbations are combined
with the heterogeneous reactions with sticking coefficients ($\gamma$) noted.

| Reaction | $\gamma$ | $O_3$ | OH | $ClNO_3$ | ClO | HCl | NO | $NO_2$ | $HNO_3$ |
|----------|----------|-------|------|----------|------|------|------|--------|---------|
| H2 | 0.02 | −50 | +600 | −90 | +4000 | −22 | −95 | −96 | +106 |
| H3 | $10^{-4}$ | −17 | −13 | −73 | −67 | +225 | +74 | +15 | −7 |
|    | 0.02 | −17 | −13 | −99 | −98 | +376 | +78 | +16 | −2 |
| H4 | $10^{-4}$ | −17 | −13 | −50 | −50 | +99 | +55 | +14 | −13 |
| H5 | 0.02 | −12 | −11 | −48 | −46 | +82 | +29 | −16 | +7 |

This can be explained by the asumption that the $HNO_3$ remains dissolved or adsorbed on the aerosols, but this seems unlikely, considering the already high acidic state of the volcanic aerosols. As for Antarctica, at first glance, this reaction produces results consistent with the observations of a large $O_3$, NO, $NO_2$ and HCl decrease and a large ClO increase. The PSC's are known to contain a large amount of $HNO_3$, which could accommodate the $HNO_3$ increase obtained from this reaction. It is clear that (H2), even though it could be important on the PSC's, seems not to be occurring on the volcanic aerosols.

Reactions (H3) and (H4) are investigated in order to establish whether or not we could enhance the HCl by producing it directly by some unknown heterogeneous mechanism. This is possible with $\gamma = 10^{-4}$ (or $J = 1.2 \times 10^{-6}$ s$^{-1}$) for (H3) and $\gamma = 0.01$ (or $J = 1.2 \times 10^{-4}$ s$^{-1}$) for (H4). These reactions produce changes in NO and $NO_2$ in the opposite direction of what the observations show. NO and $NO_2$ increase, because the Cl, which would normally keep them in the $ClNO_3$ form, is now tied up in HCl. Therefore, we conclude that such reactions are not important on the volcanic aerosols.

Reaction (H5) was suggested by Roscoe *et al.* (1986) as a possible mechanism for the NO and $NO_2$ destruction observed. Using a $\gamma$ of 0.02, we destroy all the $N_2O_5$, decreasing $NO_2$ by about 15%, and increasing HCl by about 20%. The $NO_2$ is unavailable to form $ClNO_3$, since $HNO_3$ is a $NO_x$ reservoir species; therefore, Cl is free to form HCl. The slight $HNO_3$ increase, which is not observed, can be explained by keeping it in the aerosols and therefore removing it from the gas phase. The loss of NO, and gain of OH were not obtained. For NO, this discrepency can be explained by the fact that the Roscoe *et al.* (1986) measurements were above 30 km, where the aerosol cloud ended. Therefore, another loss mechanism must be invoked. The

uncertainty in the validity of the OH measurements limits the importance of this discrepancy. Therefore, (H5) seems to be the best candidate to explain part of the observations of concentration changes after the volcanic eruption. Unfortunately, the HCl and $NO_2$ changes must be larger. Reaction (H5) has been suggested to remove the $NO_x$ species from the Antarctic stratosphere. Our results show that, while $NO_2$ decreases, HCl increases, contradicting observations in Antarctica. Also, we do not obtain a large ozone decrease, which occurs in Antarctica.

A final suggestion, which is even more speculative than the previous explanations, is that NO and $NO_2$ are adsorbed onto the aerosols. This is consistent with the observed large $NO_x$ decrease. In this case, Cl from $ClNO_3$ dissociation is free and reacts with the large $CH_4$ reservoir to form the HCl that is in excess in the observations. As for the OH, its fate is unknown, owing to the uncertainty of the observations. McKeen *et al.* (1984) calculated the loss rate of vapor to a distribution of particles and found that $NO_x$ would be depleted in a few days. The problem remains, that any mechanism that depletes NO a great deal will decrease OH, since its primary production path is via

$$HO_2 + NO \quad \rightarrow \quad OH + NO_2 \quad . \tag{R34}$$
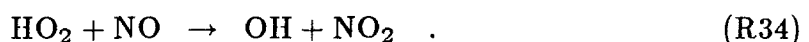
This result contradicts the OH 30% column increase observed, but as we have seen previously, this measurement is not an important constraint.

The heterogeneous mechanisms we proposed affect mostly the $NO_x$ and $ClO_x$ species. The ozone concentration is not affected a great deal by these heterogeneous reactions, except when NO is substantially decreased (by (H2) or direct NO absorption in the aerosols), in which case the ozone decreases (Table 3). Owing to the possible uncertainty in the ozone measurements, this might turn out not to

be a problem since Chandra (1987) does see a 30% ozone decrease. Our conclusion is that the heterogeneous reactions that are proposed to explain the Antarctic ozone hole problem do not completely explain the El Chichon volcanic effects. The heterogeneous reaction involving $N_2O_5$ and $H_2O$ (H5) produces results that agree reasonably well with the observations after the volcanic eruption. The problem is that the sticking coefficient of $\gamma = 0.02$ we used is probably an overestimate of the true value on sulfuric acid aerosols. Therefore, the true effect is probably smaller, worsening the agreement with the measurements. As for Antarctica, this reaction alone does not explain the observations either.

## 1.6   Conclusion

According to our model, the sudden increase in stratospheric aerosols caused a 10% increase in the radiation field between 16 and 30 km and longward of 3500 Å. In regions of low flux, the total radiation decreased by 15% within the volcanic aerosol layer. These changes have a direct impact on the photodissociation rate constants. $O_3$, $NO_2$, $NO_3$, $ClNO_3$ and $HOCl$ are among the species whose photodissociation rate constants increase by 10%, while those of $H_2O$, $NO$, and $HCl$ decrease by 15%. These changes, as well as the temperature perturbation of a few degrees lead to an $O_3$ decrease of 7% at 24 km, in agreement with observations. The 10% increase in $HCl$ is explained by an enhanced release of $Cl$ from the $ClNO_3$ and $HOCl$ reservoirs. If the observation of a 40% $HCl$ increase is caused by a direct injection into the stratosphere, we conclude that an initial $HCl$ column increase of 60% is required. To explain the $NO$, $NO_2$, $HCl$, and $OH$ observations at once, we have to investigate heterogeneous reactions. We find that the decomposition of $N_2O_5$, in the presence of water and the direct absorption of $NO_x$ in the aerosols, are the most efficient mechanisms for decreasing $NO_x$. We conclude that, if they are important, the heterogeneous reactions leading to an ozone destruction in Antarctica do not play an important role in chemistry at other latitudes or during a volcanic eruption such as El Chichon. Our model also predicts changes in the other species, such as $ClO$ and $ClNO_3$. More observations relevant to these latitudes, altitudes, and dates would therefore be essential in checking the model.

These investigations proved to be challenging for our model. It seems to respond well, since we can understand the results we obtain after including each perturbation. Unfortunately, the atmosphere contains a lot of physical and chemical

phenomena occurring at the same time, making the unraveling and understanding process difficult.

It is worth noting that these results are of some importance with regard to the nuclear winter problem of debris thrown up into the atmosphere (Turco *et al.*, 1983). It might also be interesting to adapt these results to a case of an early earth, with many active volcanoes erupting every year. The consequences on the chemistry, radiation, and temperature of the atmosphere might be very significant.

One of the least understood aspects of the chemistry of the earth's stratosphere is that of the aerosols. The optical and chemical properties of these particles are not yet fully understood. Therefore, their effect on other atmospheric species and on the radiation field is not clearly known. This makes it difficult to include them in realistic theoretical models of the atmosphere. To do this, we need more laboratory studies of aerosols and other sulfur compounds. These should include critical information on heterogeneous, aqueous–phase reaction rates. It is becoming clearer that aerosols may play a critical role in various aspects of heterogeneous atmospheric chemistry.

## Acknowledgements

# References

Adriani, A., F. Congeduti, G. Fiocco, and G.P. Gobbi, One–year observations of the stratospheric aerosol at Frascati, March 1982—March 1983. *Geophys. Res. Lett.* **10**, 1005–1008, 1983.

Adriani, A., G. Fiocco, G.P. Gobbi, and F. Congeduti, Correlated behavior of the aerosol and ozone contents of the stratosphere after the El Chichon eruption. *J. Geophys. Res.* **92**, 8365–8372, 1987.

Aiken, A.C., J.R. Herman, E.J. Maier, and C.J. McQuillan, Atmospheric chemistry of ethane and ethylene. *J. Geophys. Res.* **87**, 3105–3118, 1982.

Anderson, J.G., N.L. Mazen, B.E. McLaren, S.P. Rowe, C.M. Schiller, M.J. Schwab, L. Solomon, E.E. Thompson, and E.M. Weinstock, Free radicals in the stratosphere: A new observational technique. *Science* **228**, 1309–1311, 1985.

Angell, J.K. and J. Korshover, Global temperature variations in the troposphere and stratosphere. *Monthly Weather Review* **111**, 901–921, 1983.

Angell, J. K., J. Korshover, and W. G. Planet, Ground–based and satellite evidence for a pronounced total–ozone minimum in early 1983 and responsible atmospheric layers *Monthly Weather Review* **113**, 641–646, 1985.

Bais, A. F., C. S. Zerefos, T. C. Ziomas, N. Zoumakis, H. T. Mantis, D. J. Hofman, and G. Fiocco, Decrease in the ozone and the $SO_2$ columns following the appearance of the El Chichon aerosol cloud at midlatitude. In *Atmospheric Ozone*, C.S. Zerefos and A. Ghazi (ed.), D. Reidel, Bingham, Mass., pp. 353–356, 1985.

Barth, C.A., R.W. Sanders, R.J. Thomas, G.E. Thomas, B.M. Jakosky, and R.A. West, Formation of the El Chichon aerosol cloud. *Geophys. Res. Lett.* **10**, 993–996, 1983.

Bischof, W., R. Borchers, P. Fabian, and B.C. Kruger, Increased concentration and vertical distribution of carbon dioxide in the stratosphere. *Nature* **316**, 708–710, 1985.

Brasseur, G. and S. Solomon, *Aeronomy of the Middle Atmosphere*, Reidel Publishing Company, pp. 207–208, 1984.

Brune, Wm. H., E.M. Weinstock, M.J. Schwab, R.M. Stimpfle, and J.G. Anderson, Stratospheric ClO: *In situ* detection with a new approach. *Geophys. Res. Lett.* **12**, 441–444, 1985.

Burnett, C.R. and E.B. Burnett, Observational results on the vertical column abundance of atmospheric hydroxyl: Description of its seasonal behavior 1977–1982 and of the 1982 El Chichon perturbation. *J. Geophys. Res.* **89**, 9603–9611, 1984.

Burnett, C.R. and E.B. Burnett, Private communication, 1986.

Cadle, R.D., Volcanic emissions of halides and sulfure compounds to the troposphere and stratosphere. *J. Geophys. Res.* **80**, 1650–1652, 1975.

Cadle, R.D., Some effects of the emissions of explosive volcanoes on the stratosphere. *J. Geophys. Res.* **85**, 4495–4498, 1980.

Chandra, S., The aerosol effects on ozone measurements following the eruption of El Chichon *EOS: Transactions, American Geophysical Union* **68**, 370, 1987.

Cicerone, R.J., S. Walters, and S.C. Liu,  Nonlinear response of stratospheric ozone column to chlorine injections  *J. Geophys. Res.* **88**, 3647–3661, 1983.

Clancy, T.,  Private communication, 1988.

Clarke, A.D., R.J. Charlson, and J.A. Ogren,  Stratospheric aerosol light absorption before and after El Chichon.  *Geophys. Res. Lett.* **10**, 1017–1020, 1983.

DeLuisi, J.J., E.G. Dutton, K.L. Coulson, T.E. DeFoor, and B.G. Mendonca,  On some radiative features of the El Chichon volcanic stratospheric dust cloud and a cloud of unknown origin observed at Mauna Loa.  *J. Geophys. Res.* **88**, 6769–6772, 1983.

DeLuisi, J. J., C. L. Mateer, and W.D. Komhyr,  Effects of the El Chichon aerosol cloud on Umkehr measurements at Mauna Loa, Hawaii. In *Atmospheric Ozone,* C.S. Zerefos and A. Ghazi (ed.), D. Reidel, Hingham, Mass., pp. 316–320, 1985.

DeMore, W.B., J.J. Margitan, M.J. Molina, R.T. Watson, D.M. Golden, R.F. Hampson, M.J. Kurylo, C.J. Howard, and A.R. Ravishankara, Chemical kinetics and photochemical data for use in stratospheric modeling.  *JPL Publication* 85–37, Jet Propulsion Laboratory, Pasadena, California, 1985.

Farman, J.C., B.G. Gardiner, and J.D. Shanklin,  Large losses of total ozone in Antarctica reveal seasonal $ClO_x/NO_x$ interaction. *Nature* **315**, 207–210, 1985.

Froidevaux, L., M. Allen, and Y.L. Yung,  A critical analysis of ClO and $O_3$ in the midlatitude stratosphere. *J. Geophys. Res.* **90**, 12999–13029, 1985.

Gandrud, B.W. and A.L. Lazrus,  Measured enhancement of stratospheric sulfate and hydrochloric acid vapor attributed to El Chichon, 1983.

Gladstone, G.R., Radiative transfer with partial frequency redistribution in inhomogeneous atmosphere: Application to the Jovian aurora. *J. Quant. Spectrosc. Radiat. Transfer* **27**, 545-576, 1982.

Hansen, J.E. and L.D. Travis, Light scattering in planetary atmospheres. *Sp. Sci. Rev.* **16**, 527-610, 1974.

Heath, D.F. and B.H. Schlesinger, Global response of stratospheric ozone to natural perturbations on climatological time scales by variations of UV solar flux and the eruption of El Chichon. *EOS: Transactions, American Geophysical Union* **65**, 836-837, 1984.

Hofmann, D.J. and J.M. Rosen, Stratospheric sulfuric acid fraction and mass estimate for the 1982 volcanic eruption of El Chichon. *Geophys. Res. Lett.* **10**, 313-316, 1983.

Hofmann, D.J. and R.M. Rosen, On the temporal variation of stratospheric aerosol size and mass during the first 18 months following the 1982 eruptions of El Chichon. *J. Geophys. Res.* **89**, 4883-4890, 1984.

Jäger, H. and W. Carnuth, The decay of the El Chichon stratospheric perturbation, observed by Lidar at Northern midlatitudes. *Geophys. Res. Lett.* **14**, 696-699, 1987.

Johnston, H.S. and J. Podolske, Interpretation of stratospheric photochemistry. *Rev. Geophys. Space Phys.* **16**, 491-519, 1978.

Knollenberg, R.G. and D. Huffman, Measurements of the aerosol size distributions in the El Chichon cloud. *Geophys. Res. Lett.* **10**, 1025-1028, 1983.

Komhyr, W.D., S.J. Oltmans, A.N. Chopra, R.K. Leonard, T.E. Garcia, and C. McFee, Results of Umkehr, ozonesonde, total ozone, and sulfur dioxide observations in Hawaii following the eruption of El Chichon volcano in 1982 In *Atmospheric Ozone*, C.S. Zerefos and A. Ghazi (ed.), D. Reidel, Hingham, Mass., pp. 305–310, 1985.

Krueger, A.J., and R.A. Minzner, A midlatitude ozone model for the 1976 U.S. Standard Atmosphere. *J. Geophys. Res.* **81**, 4477–4481, 1976.

Krueger, A.J., Sighting of El Chichon sulfur dioxide clouds with Nimbus 7 total ozone mapping spectrometer. *Science* **220**, 1377, 1983.

Labitzke, K., B. Naujokat, and M.P. McCormick, Temperature effects on the stratosphere of the April 4, 1982 eruption of El Chichon, Mexico. *Geophys. Res. Lett.* **10**, 24–26, 1983.

Leu, M.-T., Laboratory studies of sticking coefficients and heterogeneous reactions important in the Antarctic stratosphere. *Geophys. Res. Lett.* **15**, 17–20, 1988.

Liou, K.-N., *An Introduction to Atmospheric Radiation*, Academic Press, **26**, pp. 55, 1980.

London, J., *Proceedings of the NATO Advanced Study Institute on Atmospheric Ozone: Its Variation and Human Influences*, report no. FAA-EE-80-20, U.S. Dept. of Transportation, pp. 31–44, 1979.

Luther, F.M. and R.J. Gelinas, Effect of molecular multiple scattering and surface albedo on atmospheric photodissociation rates. *J. Geophys. Res.* **81**, 1125–1132, 1976.

Mankin, W.G. and M.T. Coffey, Increased stratospheric hydrogen chloride in the El Chichon cloud. *Science* **226**, 170–172, 1984.

Mankin, W.G. and M.T. Coffey, *The Impact of El Chichon on the Chemistry of the Stratosphere*, Abstracts volume from the Norman D. Watkins symposium on the environmental impact of volcanism, Graduate school of oceanography, Rhode Island, March 1986.

Mantis, H.T., C.S. Zerefos, A. Bais, I. Ziomas, and A. Kelessis, The northern hemisphere ozone minimum in 1982–1983. In press, *Arch. Meteorol. Geophys. Bioclimatol., Ser. B*, 1986.

McElroy, M. B., R. J. Salawitch, and S. C. Wofsy, Antarctic ozone: Reduction due to synergistic interactions of chlorine and bromine. *Nature* **321**, 759–762, 1986.

McFarland, M., B.A. Ridley, M.H. Proffitt, D.L. Albritton, T.L. Thompson, W.J. Harrop, R.H. Winkler, and A.L. Schmeltekopf, Simultaneous *in situ* measurements of $NO_2$, NO, and $O_3$ between 20 and 31 km. *J. Geophys. Res.* **91**, 5421–5437, 1986.

McKeen, S.A., S.C. Liu, and C.S. Kiang, On the chemistry of stratospheric $SO_2$ from volcanic eruptions. *J. Geophys. Res.* **89**, 4873–4831, 1984.

Michelangeli, D.V., M. Allen, Y.L. Yung, Enhancement of the actinic flux by an aerosol layer, 1988.

Molina, M.J., and F.S. Rowland, Stratospheric sink for chlorofluoromethanes: Chlorine atom catalyzed destruction of ozone *Nature* **249**, 810–812, 1974.

Molina, M. J., T. L. Tso, L. T. Molina, and F. C. Y. Wang, Antarctic stratospheric chemistry of chlorine nitrate, hydrogen chloride and ice: Release of active chlorine. *Science* **238**, 1253–1257, 1987.

Pollack, J.B., O.B. Toon, E.F. Danielson, D.J. Hofmann, and J.M. Rosen, The El Chichon volcanic cloud: An introduction. *Geophys. Res. Lett.* **10**, 989–992, 1983.

Pollack, J.B. and T.P. Ackerman, Possible effects of the El Chichon volcanic cloud on the radiation budget of the northern tropics. *Geophys. Res. Lett.* **10**, 1057–1060, 1983.

Prather, M.J., M.B. McElroy, and S.C. Wofsy, Reductions in ozone at high concentrations of stratospheric halogens. *Nature* **312**, 227–231, 1984.

Quiroz, R.S., The isolation of stratospheric temperature change due to the El Chichon volcanic eruption from nonvolcanic signals. *J. Geophys. Res.* **88**, 6773–6780, 1983.

Roscoe, H.K., B.J. Kerridge, L.J. Gray, R.J. Wells, and J.A. Pyle, Simultaneous measurements of stratospheric NO and $NO_2$ and their comparison with model predictions. *J. Geophys. Res.* **91**, 5405–5419, 1986.

Rosenfield, J.E., M.R. Schoeberl, and M.A. Geller, A computation of the diabatic circulation using an accurate radiative transfer model. *J. Atmos. Sci.* **44**, 859–876, 1987.

Rossi, M.J., R. Malhotra, and D.M. Golden, Heterogeneous chemical reaction of chlorine nitrate and water on sulfuric–acid surfaces at room temperature. *Geo-*

*phys. Res. Lett.* **14**, 127–130, 1987.

Rowland, F.S. and M.J. Molina, Chlorofluoromethanes in the environment *Rev. Geophys. Space Phys.* **13**, 1–35, 1975.

Schoeberl, M.R. and A.J. Krueger, Overview of the Antarctic ozone depletion issue *Geophys. Res. Lett.* **13**, 1191–1192, 1986.

Solomon, P.M., R. de Zafra, A. Parrish, and J.W. Barrett, Diurnal variation of stratospheric chlorine monoxide: A critical test of chlorine chemistry in the ozone layer. *Science* **224**, 1210–1214, 1984.

Solomon, S., R. R. Garcia, F. S. Rowland, and D. J. Wuebbles, On the depletion of Antarctic ozone. *Nature* **321**, 755–758, 1986.

Spinhirne, J.D. and M.D. King, Latitude variation of spectral thickness and columnar size distribution of the El Chichon stratospheric aerosol layer. *J. Geophys. Res.* **90**, 10607–10619, 1985.

Thomas, G.E., B.M. Jakosky, R.A. West, and R.W. Sanders, Satellite limb-scanning thermal infrared observations of the El Chichon stratospheric aerosol: First results. *Geophys. Res. Lett.* **10**, 997–1000, 1983.

Turco, R.P., O.B. Toon, T.P. Ackerman, J.B. Pollack, and C. Sagan, Nuclear Winter: Global consequences of multiple nuclear explosions. *Science* **222**, 1283–1292, 1983.

*U.S. Standard Atmosphere*, U.S. Government Printing Office, Washington, D.C.

Van de Hulst, H.C., *Multiple Light Scattering: Tables, Formulas, and Applications*,

Academic Press, **2**, pp. 303–317, 1980.

Wang, P.W. and M.P. McCormick, Variations in stratospheric aerosol optical depth during northern warmings. *J. Geophys. Res.* **90**, 10597–10606, 1985.

Watson, R.T. (editor-in-chief), *et al.* (16 editors), *Atmosphere ozone 1985: Assessment of our understanding of the processes controlling its present distribution and change. WMO global ozone research and monitoring project report*, No. 16, 1985.

Woods, D.C., R.L. Chuan, and W.I. Rose, Halite particles injected into the stratosphere by the 1982 El Chichon eruption. *Science* **230**, 170–172, 1985.

# PAPER II

# Yields of $O_2(^1\Sigma g^+)$ and $O_2(^1\Delta g)$ in the $H + O_2$ Reaction System, and the Quenching of $O_2(^1\Sigma g^+)$ by Atomic Hydrogen

# Yields of $O_2(^1\Sigma g^+)$ and $O_2(^1\Delta g)$ in the H + $O_2$ Reaction System, and the Quenching of $O_2(^1\Sigma g^+)$ by Atomic Hydrogen

Diane V. Michelangeli

Division of Geological and Planetary Sciences

California Institute of Technology

Pasadena, California   91125

Kuang-Yul Choo* and Ming-Taun Leu

Earth and Space Sciences Division

Jet Propulsion Laboratory

California Institute of Technology

Pasadena, California   91109

* NASA/NRC Resident Research Associate, on leave from the Department of Chemistry, Seoul National University, Seoul, Korea (1984–1985).

## ABSTRACT

The generation of metastable $O_2(^1\Sigma g^+)$ and $O_2(^1\Delta g)$ in the $H + O_2$ system of reactions was studied by the flow discharge chemiluminescence detection method. In addition to the $O_2(^1\Sigma g^+)$ and $O_2(^1\Delta g)$ emissions, strong $OH\,(\nu = 2) \rightarrow OH\,(\nu = 0)$, $OH\,(\nu = 3) \rightarrow OH\,(\nu = 1)$, $HO_2\,(^2A'_{000}) \rightarrow HO_2\,(^2A''_{000})$, $HO_2\,(^2A'_{001}) \rightarrow HO_2\,(^2A''_{000})$, and $HO_2\,(^2A''_{200}) \rightarrow HO_2\,(^2A''_{000})$ emissions were detected in the $H + O_2$ system. The rate constants for the quenching of $O_2(^1\Sigma g^+)$ by $H$ and $H_2$ were determined to be $(5.1 \pm 1.4) \times 10^{-13}$ and $(7.1 \pm 0.1) \times 10^{-13}$ cm$^3$ s$^{-1}$, respectively. An upper limit for the branching ratio to produce $O_2(^1\Sigma g^+)$ by the $H + HO_2$ reaction was calculated to be 2.1%. The contributions from other reactions producing singlet oxygen were investigated.

## 2.1 Introduction

Recent attempts to delineate the chemical mechanisms responsible for singlet oxygen emissions in the atmospheres of Earth, Venus, and Mars have focussed on reactions involving the production of $O_2$. For instance, above 80 km in the terrestrial atmosphere, the chemistry is dominated by the $HO_x$ radicals and the reactions between them. Thus, in modeling the airglow, it is imperative to establish the yields of $O_2(^1\Sigma g^+)$ and $O_2(^1\Delta g)$ in all reactions involving O, H, OH, and $HO_2$. The reaction of H atoms with $O_2$, the dominant source of $HO_2$ in the terrestrial atmosphere, as well as in laboratory studies of $HO_2$ kinetics, has been observed in the laboratory to give rise to singlet oxygen emission.

Hislop and Wayne (1977) first reported the detection of $O_2(^1\Sigma g^+)$ in the $H + O_2$ reaction system by observing the $O_2(^1\Sigma g^+) \rightarrow O_2(^3\Sigma g)$ (0–0) transition at 762 nm. From analyses of the emission intensities they suggested that the step responsible for $O_2(^1\Sigma g^+)$ generation was

$$H + HO_2 \quad \rightarrow \quad H_2 + O_2(^1\Sigma g^+), \tag{1}$$
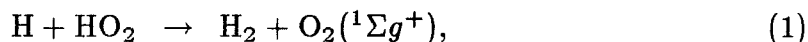
with a branching ratio of $2.8 \times 10^{-4}$. Subsequently, the yields of $O_2(^1\Sigma g^+)$ from reactions of $HO_2$ with a variety of species have been studied by Keyser, Choo and Leu (1985). In these studies, $HO_2$ was produced by reaction of F with $H_2O_2$. An upper limit of $8 \times 10^{-3}$ for the yield of $O_2(^1\Sigma g^+)$ from $H + HO_2$ was reported. However, vibrationally excited HF produced in their system limited the sensitivity. The method chosen in our study to produce $HO_2$ from $H + O_2 + M \rightarrow HO_2 + M$ removed that effect.

$O_2(^1\Delta g)$ has been detected in only one study of $H + O_2$. Washida *et al.* (1978), using photoionization–mass spectrometry for the detection of singlet oxygen, re-

ported a branching ratio of 0.015 for

$$H + HO_2 \rightarrow H_2 + O_2(^1\Delta g) \quad . \tag{2}$$
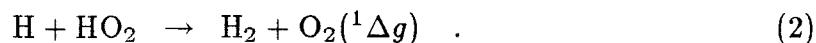
The mass–spectral signals detected by Washida $et$ $al.$ (1978) were not unique to $O_2(^1\Delta g)$. Therefore, a contribution from $O_2(^1\Sigma_g^+)$ could not be distinguished. In addition, part of the $O_2(^1\Delta g)$ detected could be the product from $O_2(^1\Sigma_g^+)$ quenching.

We have constructed a flow–discharge–chemiluminescence detection system with the capacity of detecting $O_2(^1\Sigma_g^+)$ and $O_2(^1\Delta g)$ in the concentration ranges of $> 5 \times 10^8$ cm$^{-3}$ and $> 6 \times 10^{10}$ cm$^{-3}$, respectively, with a moderate spectral resolution (5 nm). The system can also give detailed information about the pressure (1–10 torr) and reaction time (1–200 ms) dependences of the chemiluminescence signal.

The resolution and sensitivity of the currently employed detection system, being significantly better than those employed by Hislop and Wayne (1977) and Keyser $et$ $al.$ (1985), provides for an improved attempt at understanding the complex chemistry initiated by reaction of H with $O_2$. In addition, time- and concentration-dependent studies of the $O_2(^1\Sigma_g^+)$ signal can be accomplished, which will test for the possibility of lowered $O_2(^1\Sigma_g^+)$ yields because of efficient quenching by H atoms or perhaps the reactor wall. Finally, this study represents the first attempt to detect $O_2(^1\Delta g)$ by optical techniques, and the first attempt to measure simultaneously both excited oxygen species in the reaction of H + $HO_2$.

This paper includes the experimental procedures, results, and discussions of the quenching reactions of $O_2(^1\Sigma_g^+)$ by H and $H_2$, and the yields of $O_2(^1\Sigma_g^+)$ and $O_2(^1\Delta g)$ from reactions in the H + $O_2$ system. The atmospheric implications of these results are also discussed.

## 2.2 Experimental

### 2.2.1 Apparatus and Procedure

The details of the detection system and fast–flow discharge setup are described elsewhere (Leu and Smith, 1981; Leu, 1984). The inside wall of the flow reactor was coated with halocarbon wax. Hydrogen atoms were generated by microwave discharge of $H_2$–He mixtures. He was also added at a point in the reactor, which bypassed the discharge cavity to bring the total pressure in the reactor between 1 and 5 torr. In order to vary the reaction time, $O_2$ was added through a movable injector, fitted at the upstream end with a microwave discharge cavity for the production of $O_2(^1\Sigma g^+)$ in the quenching experiments.

The concentrations of $O_2$, $H_2$, He and NO were measured, using calibrated mass flowmeters. The concentrations of $O_2(^1\Sigma g^+)$ and $O_2(^1\Delta g)$ were measured by monitoring the characteristic emission bands at 762 nm and 1.27 $\mu$m, respectively. The calibration of the signals was carried out by comparison with the $NO_2{}^*$ signal from the reaction $O + NO \rightarrow NO_2{}^*$, using the well known procedure (Fontijin $et$ $al.$, 1964; Golde $et$ $al.$, 1973; Vanpee $et$ $al.$, 1971). The sensitivities for $O_2(^1\Sigma g^+)$ and $O_2(^1\Delta g)$ were approximately $5 \times 10^8$ cm$^{-3}$ and $6 \times 10^{10}$ cm$^{-3}$, respectively.

Atomic hydrogen concentrations were measured by two independent methods. First, the difference between mass–spectrometer signals at $m/e = 2$ amu ($H_2$) with the microwave discharge on and off were obtained. Typically, dissociation efficiencies were 5–30%. For the quenching experiments, H atom concentrations were obtained by stoichiometric titration with measured amounts of NOCl, which entered the flow system through a side inlet. The end point of the titration was detected by the lack of HNO$^*$ emission at 762.5 nm upon addition of NO into the reactor, following the

reactions:

$$H + NOCl \rightarrow HCl + NO$$

$$H + NO + M \rightarrow HNO^* + M.$$
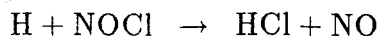
NO concentrations on the order of $3 \times 10^{14}$ cm$^{-3}$, added through the slide injector, were measured, since the reaction to form HNO$^*$ is relatively slow.

Flow rates of NOCl were determined from pressure drops in a calibrated volume. Care was taken to ensure that the temperature remained constant by good insulation, and that the NOCl was exposed to glass or monel surfaces only.

One complication in the H atom calibrations was that NO and NOCl were very efficient at changing the conditions of the flow tube walls. After a few experiments, the H atom wall loss increased over a factor of two, because of efficient adsorption on the walls. For this reason, wall loss measurements were taken before and after each experiment.

Quenching experiments of $O_2(^1\Sigma g^+)$ by H were accomplished as follows: 1) wall loss measurement ($O_2$ discharge without H$_2$ in the system); 2) H titration (H$_2$ discharge with NO and NOCl present, without O$_2$); 3) measurement of the $O_2(^1\Sigma g^+)$ signal at 762 nm (with H$_2$ and O$_2$ discharges, without NO and NOCl); 4) evaluation of the effect of the reactions:

$$H + O_2 + M \rightarrow HO_2 + M \tag{7}$$

$$H + HO_2 \rightarrow H_2 + O_2(^1\Sigma g^+) \tag{1}$$
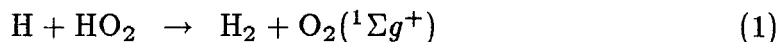
(by turning off the O$_2$ discharge and looking at the background $O_2(^1\Sigma g^+)$ signal); 5) second titration; and 6) second wall loss measurement. The same procedure was repeated for various [H$_2$] and [H] concentrations.

The conditions of the H atom quenching experiments were: $P = 3\text{--}5$ torr, $\bar{v} \simeq 3100$ cm/s, $[M] = 1 \times 10^{17}$ cm$^{-3}$, [NO] $= 3\text{--}5 \times 10^{14}$ cm$^{-3}$, [H$_2$] $\simeq 1\text{--}2 \times 10^{13}$ cm$^{-3}$, and [H] $= 0\text{--}2 \times 10^{13}$ cm$^{-3}$.

For the study of $O_2(^1\Sigma g^+)$ yields, the pressures employed were 1, 2, and 4 torr, with total reaction times ranging from 18 to 80 ms. At each pressure, $O_2$ concentrations were varied (from $5.7 \times 10^{14}$ to $1.0 \times 10^{16}$ $cm^{-3}$), while $[H_2] \simeq 8 \times 10^{13}$ $cm^{-3}$ and $[H] \simeq 1 \times 10^{12}$ $cm^{-3}$ were fixed.

For $O_2(^1\Delta g)$, the experiments were performed between 3 and 5 torr and with flow velocities between 350 and 2000 cm/s, $[O_2] = 2 \times 10^{15}$–$1 \times 10^{16}$ $cm^{-3}$, $[H_2] = 4 \times 10^{14}$–$1 \times 10^{15}$ $cm^{-3}$, and $[H] = 7 \times 10^{13}$–$7 \times 10^{14}$ $cm^{-3}$. CO was used in an attempt at scavenging the OH formed.

### 2.2.2  Materials

He (Matheson, 99.9999%), $H_2$ (Matheson, 99.999%), $O_2$ (Matheson, 99.9%), $N_2$ (Matheson, 99.9995%), NO (Matheson, 99.0%), and NOCl (Matheson, 97.0%) were all used without further purification. CO was purified by a two–stage trap system: first in liquid $N_2$ (77 K), and second in a molecular sieve in dry ice/alcohol slush (196 K).

## 2.3 Results

### 2.3.1 Quenching of $O_2(^1\Sigma g^+)$ by $H_2$ and H

In the absence of added quenchers, $O_2(^1\Sigma g^+)$ concentrations decayed because of wall collisions. $O_2(^1\Sigma g^+)$ wall loss rate measurements were performed by varying the slide injector position through which $O_2$ was flowing and excited by a microwave discharge.

The slope of a plot of $[O_2(^1\Sigma g^+)]$ as a function of reaction time gave the first–order wall loss rate. Typical wall loss rates for $O_2(^1\Sigma g^+)$ were 30 and 80 s$^{-1}$ in the new and old flow tubes, respectively.

As a test of our experimental apparatus, we reexamined the quenching of $O_2(^1\Sigma g^+)$ by $H_2$, investigated previously by Choo and Leu (1985). $O_2$ in He was passed through the microwave discharge cavity in the slide injector. Concentrations of $O_2$ were maintained below $< 1 \times 10^{14}$ cm$^{-3}$ in order to avoid secondary production of $O_2(^1\Sigma g^+)$ from the reactions:

$$O_2(^1\Delta g) + O_2(^1\Delta g) \rightarrow O_2(^1\Sigma g^+) + O_2 \tag{1}$$

$$O + O + M \rightarrow O_2(^1\Sigma g^+) + M.$$
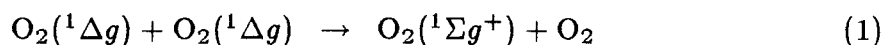
In addition, O atoms were removed by passing the flow of $O_2$ over mercuric oxide layers downstream of the discharge. The linearity of the pseudo first–order decay plot for the quenching of $O_2(^1\Sigma g^+)$ by $H_2$ (Fig. 1) shows that this condition was satisfied. From the plot of pseudo first–order decay rates as a function of $[H_2]$, a bimolecular rate for the quenching of $O_2(^1\Sigma g^+)$ by $H_2$ of $k_{24} = (7.1 \pm 0.1) \times 10^{-13}$ cm$^3$ s$^{-1}$ was obtained (see Fig. 2). The reported error represents one standard deviation (see Fig. 2). This value is in excellent agreement with the values reported

in the literature by Choo and Leu (1985) $(7.0 \pm 0.3) \times 10^{-13}$ cm$^3$ s$^{-1}$.

Preliminary measurements of $O_2(^1\Sigma g^+)$ yields in the H + O$_2$ system revealed that quenching of $O_2(^1\Sigma g^+)$ by H atoms significantly impacted the observed oxygen emission. Consequently, we attempted to quantify this process. 5% NOCl/He, of various flow rates, was added to the flow system, and the HNO$^*$ signals were monitored each time. Figure 3 represents a typical titration plot. Linear regressions were performed on each line to find the intercept with the [NOCl] axis, which gave the H atom concentration with an associated error of about 20%. The time dependent behavior of $O_2(^1\Sigma g^+)$ is shown in Figure 4. The values for $[O_2(^1\Sigma g^+)]$ were corrected for a small contribution from reactions (7) and (1) by removing the signal obtained when the O$_2$ discharge was turned off.

Extracting the rate constant for $O_2(^1\Sigma g^+)$ quenching by H atoms is not a straightforward process. One has to take into consideration the wall loss and the quenching by H$_2$. If $x$ is the dissociation efficiency of the microwave discharge in percent of H$_2$, then

$$[H_2] = \left(\frac{100 - x}{2x}\right)[H], \tag{I}$$

and it is straightforward to obtain the following relationship:

$$\ln[O_2(^1\Sigma g^+)] = -\left\{k_{H_2}[H_2] + k_H[H] + k_w\right\} t, \tag{II}$$

where $k_{H_2}$, $k_H$, and $k_w$ are the rate constants for quenching by H$_2$, H, and the wall, respectively. Since $k_w$ was measured in each experiment, $k_{H_2}$ was determined $(7.1 \times 10^{-13}$ cm$^3$ s$^{-1})$, and [H$_2$] was known from (I), from the slope of the $O_2(^1\Sigma g^+)$ vs. $t$ plots (Fig. 4), we were able to plot $k_{obs} - k_{H_2}[H_2]$ as a function of [H] (Fig. 5) where $k_{obs}$ is the negative of the slope from Figure 4 (line b), minus $k_w$. $k_H$ was obtained from the slope of Figure 5 and was found to be $(5.5 \pm 1.4) \times 10^{-13}$ cm$^3$ s$^{-1}$, where the error represents one standard deviation.

Figure 1. Pseudo first–order decays of $O_2(^1\Sigma g^+)$ for $T = 295$ K, $\bar{v} = 825$ cm/s, $P_T = 3.87$ torr, $[M] = 1.27 \times 10^{17}$ cm$^{-3}$, $[O_2] = 3.80 \times 10^{13}$ cm$^{-3}$ with $[H_2]$ = a) 0, b) $2.42 \times 10^{13}$ cm$^{-3}$, c) $4.75 \times 10^{13}$ cm$^{-3}$, d) $6.98 \times 10^{13}$ cm$^{-3}$, e) $9.78 \times 10^{13}$ cm$^{-3}$ and $1.38 \times 10^{14}$ cm$^{-3}$, where $d$ is the distance between the injector and the detection zone.

Figure 2. First–order rates $(s^{-1})$ as a function of $[H_2]$ $(cm^{-3})$ under the same conditions as in Figure 1.
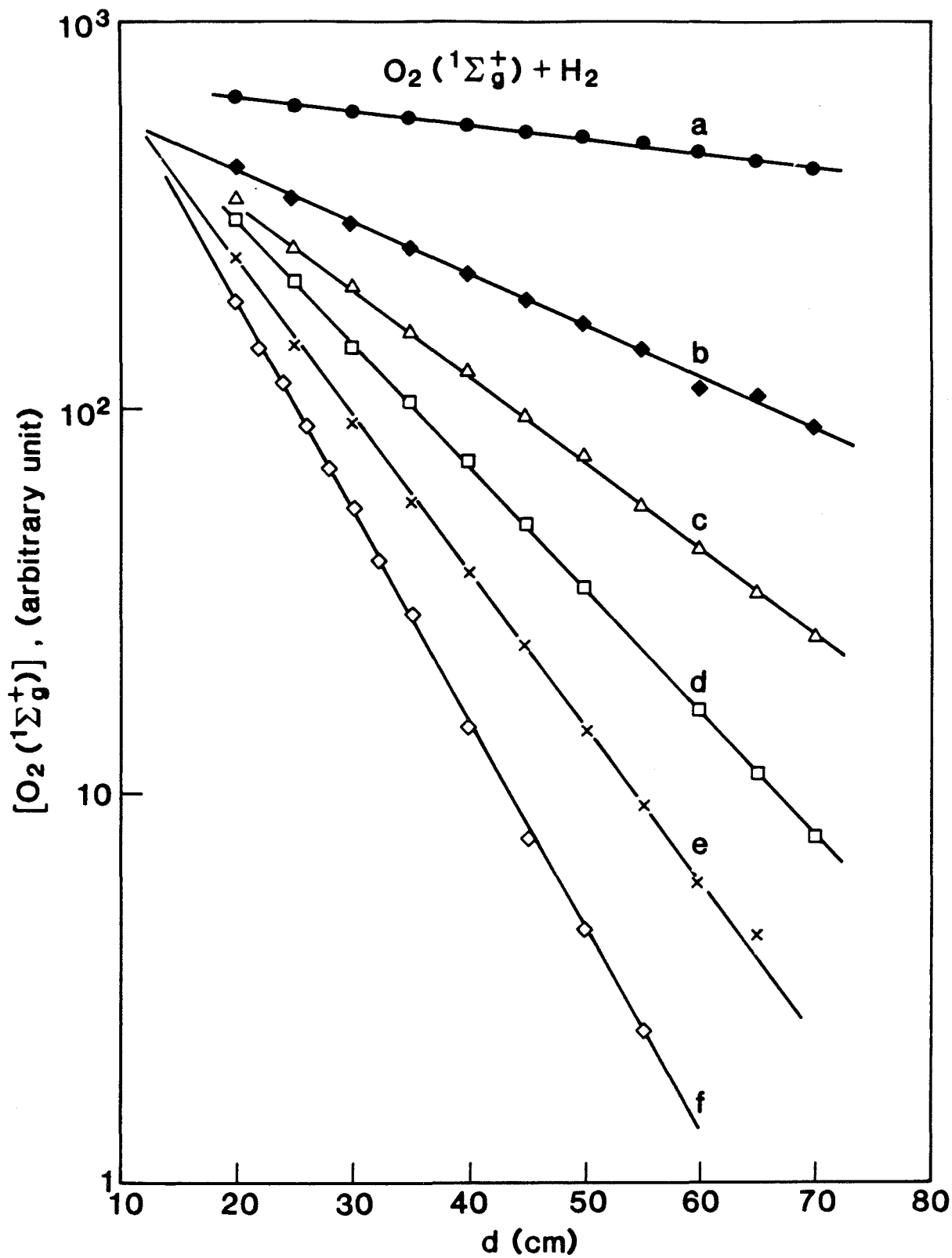
Figure 1
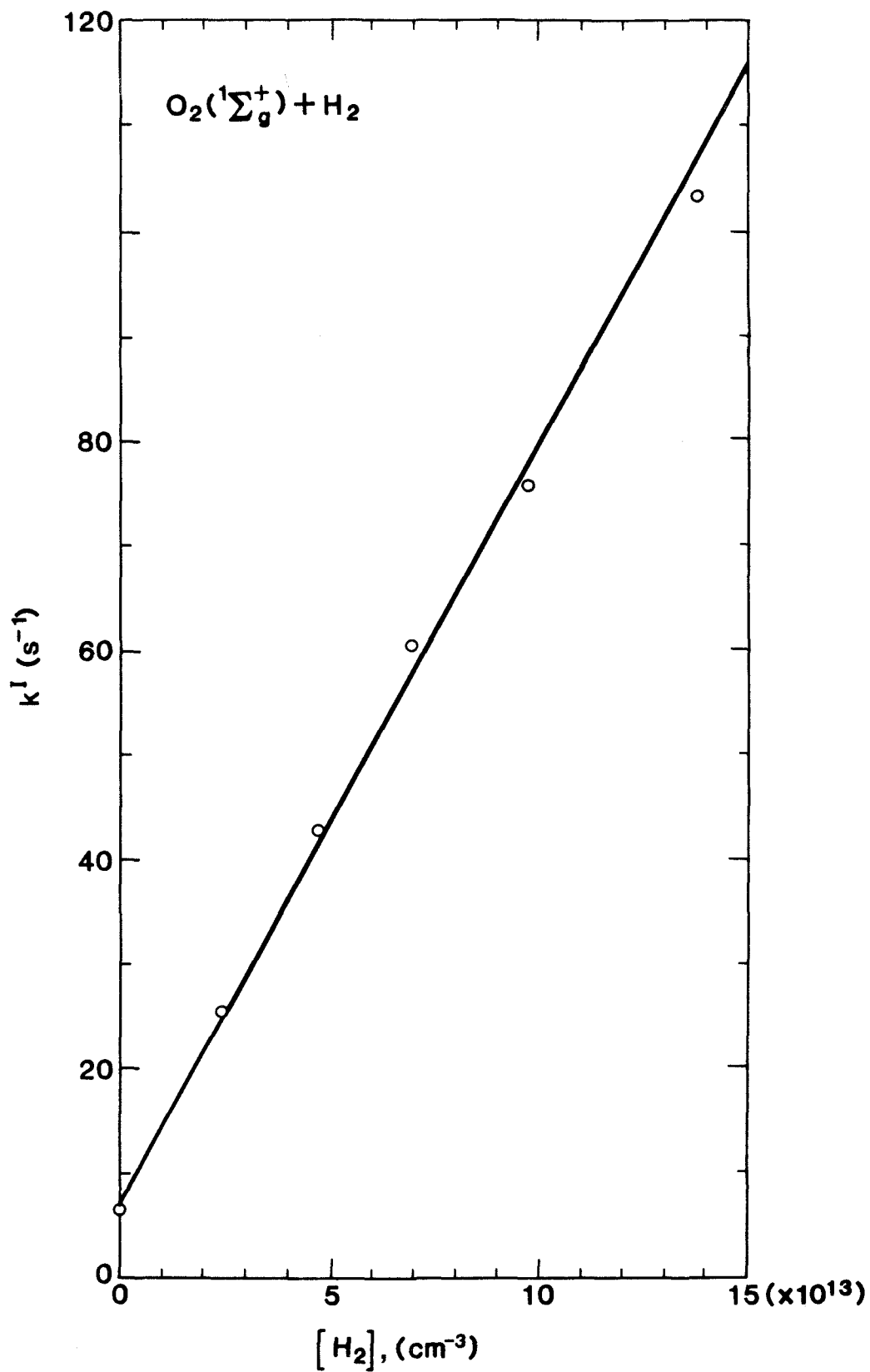
Figure 2

Figure 3. $[HNO^*]$ (arbitrary units), as a function of $[NOCl]$ ($cm^{-3}$) for titration of $[H]$ with $P = 3.50$ torr, and $\bar{v} = 3120$ cm/s.

Figure 4. Pseudo first–order decays of $O_2(^1\Sigma g^+)$ for $P = 4.05$ torr, $\bar{v} = 3174$ cm/s, $[M] = 1.3 \times 10^{17}$ $cm^{-3}$, $[O_2] = 6.1 \times 10^{13}$ $cm^{-3}$, and a) $[H_2] = [H] = 0$, b) $[H_2] = 6.8 \times 10^{13}$ $cm^{-3}$, $[H] = 1.8 \times 10^{13}$ $cm^{-3}$, and c) $[H_2] = 7 \times 10^{13}$ $cm^{-3}$, $[H] = 0$.

Figure 5. $k_{obs} - k_{H_2}[H_2]$ as a function of $[H]$ ($cm^{-3}$), where $k_{obs}$ is the negative of the slope of line $b$ in Figure 4.
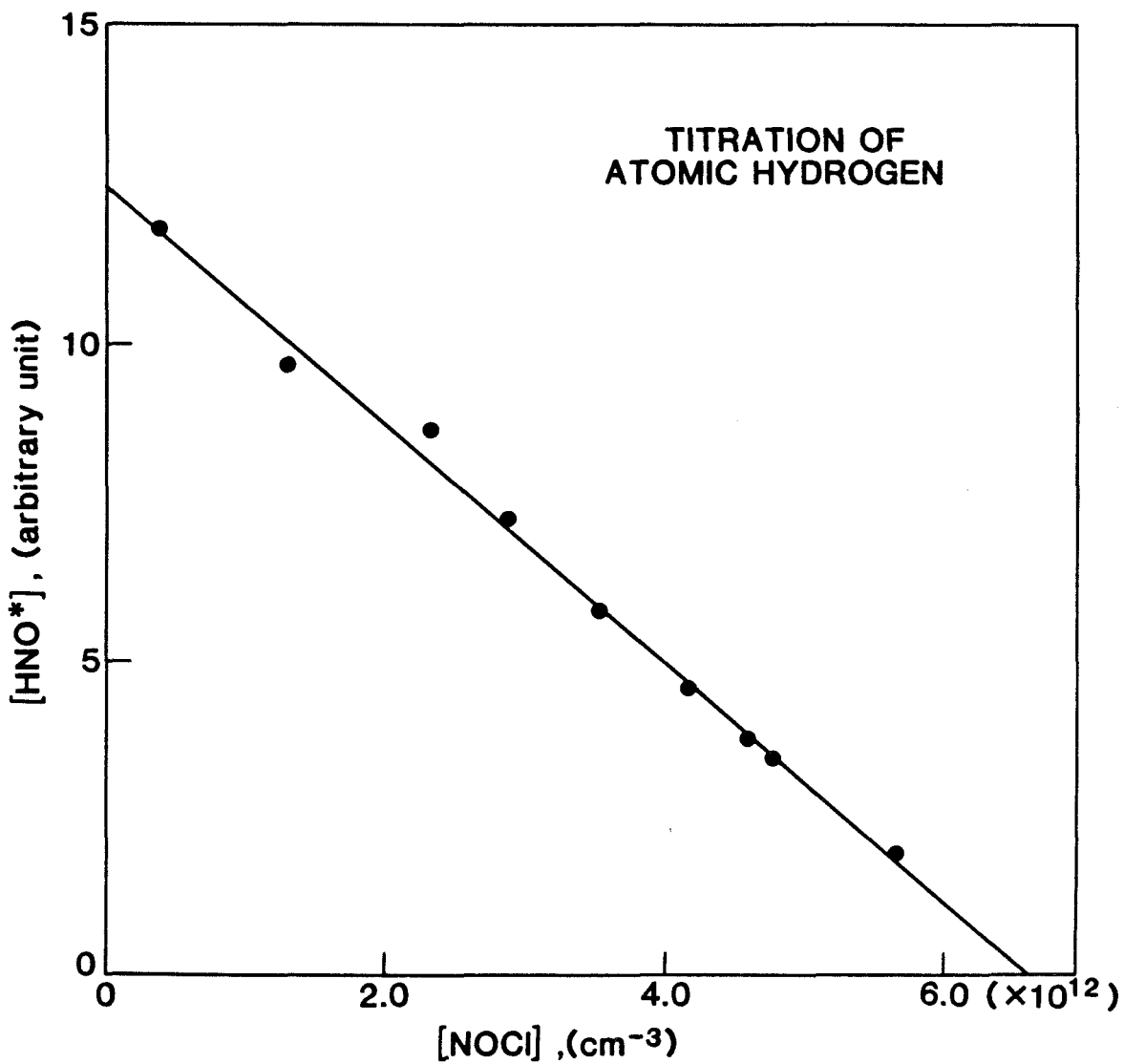
Figure 3
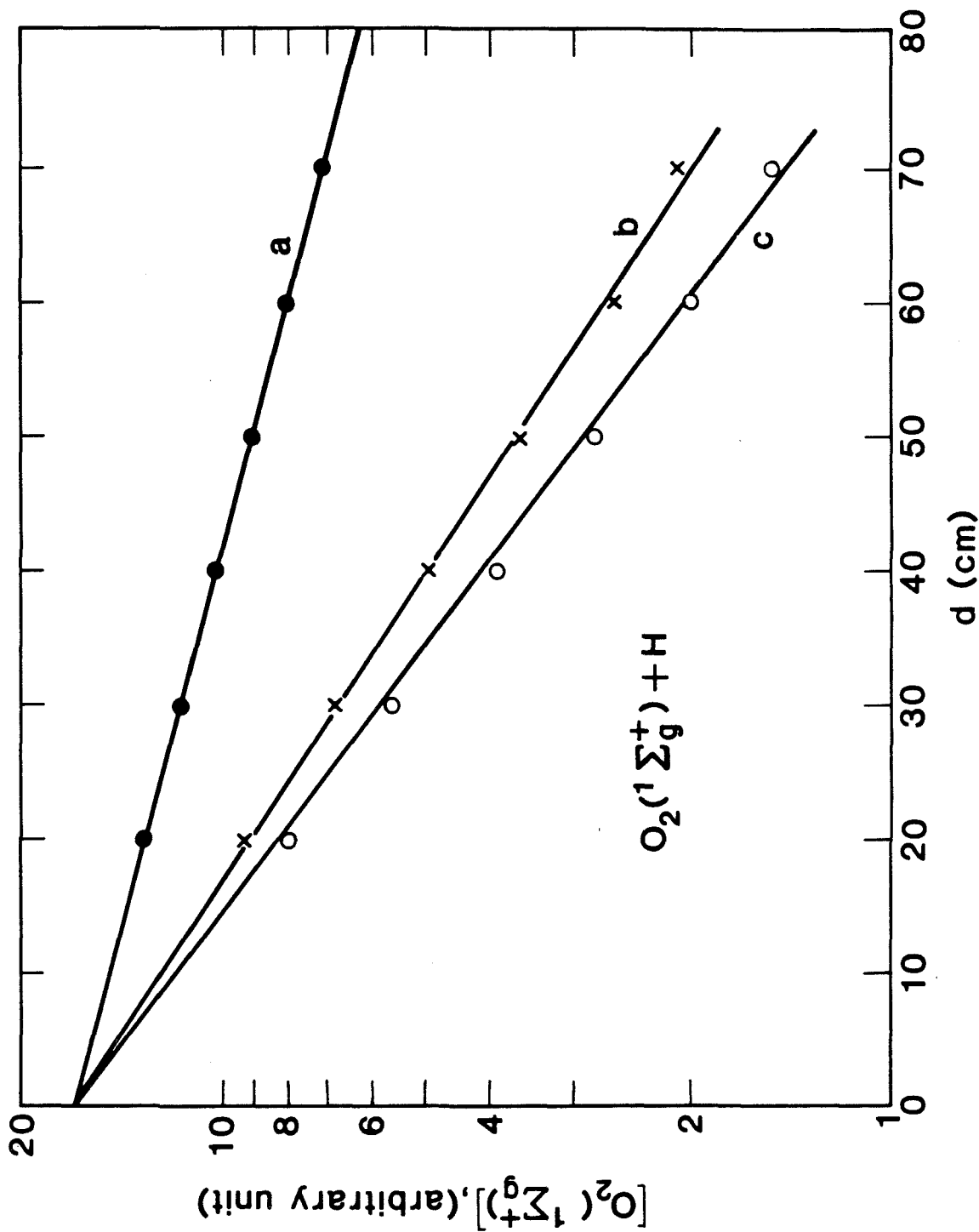
Figure 4
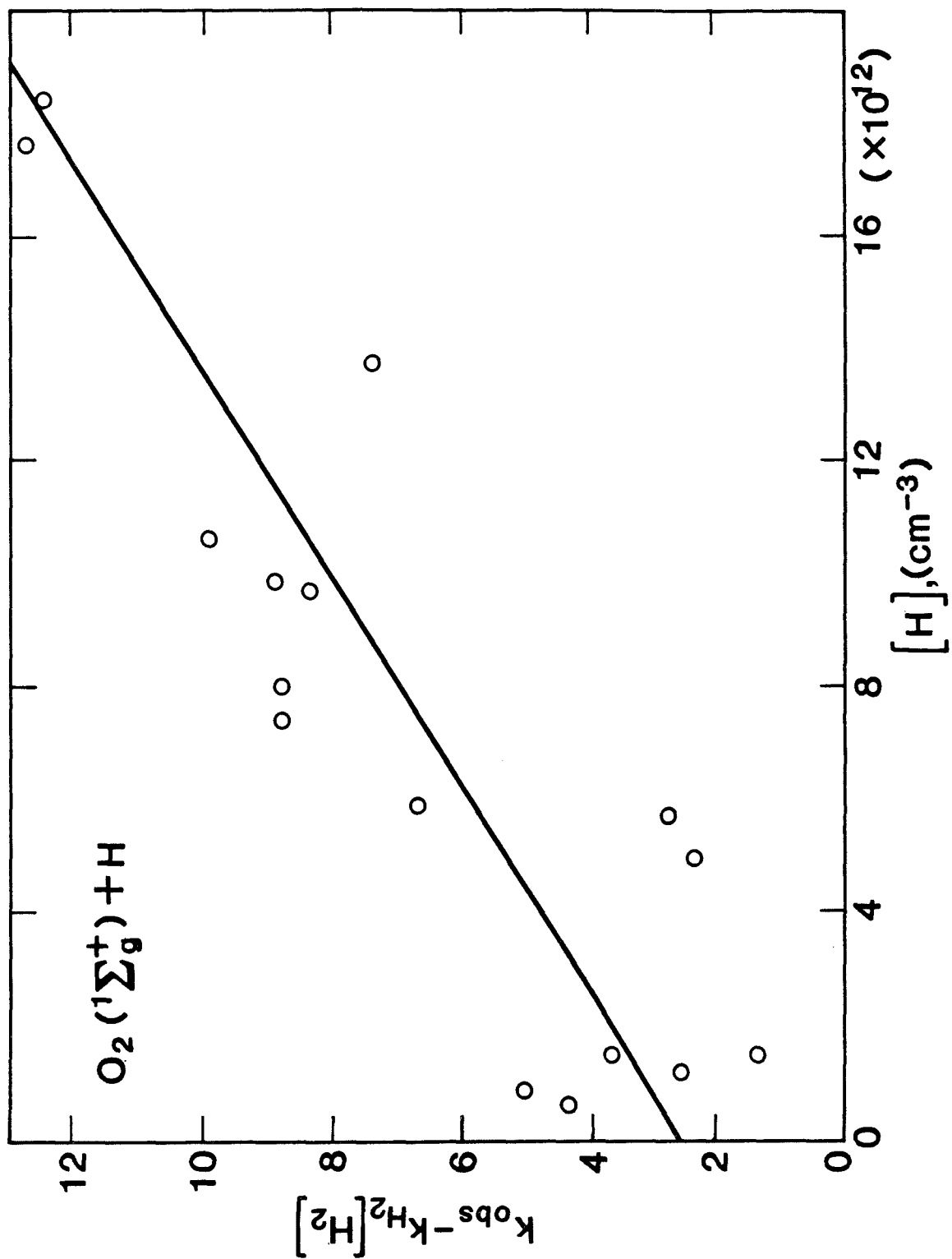
Figure 5

## 2.3.2    Yields of $O_2(^1\Sigma g^+)$ and $O_2(^1\Delta g)$

The chemiluminescence spectra from 600 nm to 2 $\mu$m revealed not only the presence of the metastable states of $O_2$, but also of various vibrationally and electronically excited states of OH and $HO_2$ (denoted $OH^*$ and $HO_2^*$ in a general way). In the spectral region around the $O_2(^1\Sigma g^+)$ emission at 762 nm, we observed the (0–1) transition at 864 nm, and a broad band between 760–870nm, which we attribute to the $HO_2$ $(^2A', \nu_3' = 6 \rightarrow^2 A'', \nu_3'' = 0)$ transitions (Keyser, 1986). A spectrum from 1.25 to 1.55 $\mu$m is reproduced on Figure 6a. Figure 6b shows spectra of the $O_2(^1\Delta g)$ emission at 5 torr as a function of reaction time. As the pressure and/or the reaction time in the flow tube decreased, there was substantial interference from $HO_2^*$ to the $O_2(^1\Delta g)$ signal at 1.27 $\mu$m. The 1.43 $\mu$m band corresponds to $HO_2$ $(^2A'_{010} \rightarrow^2 A''_{000})$ (Fig. 4a). $OH^*$ (3,1) and $OH^*$ (2,0) are between 1.45 and 1.52 $\mu$m (Fig. 6c), while the 1.52 $\mu$m band also includes the $HO_2$ $(^2A''_{200} \rightarrow^2 A''_{000})$ overtone transitions of the H–OO stretching vibration in the $^2A''$ ground state (Fig. 6a). At 1.29 $\mu$m, the band corresponds to $HO_2$ $(^2A'_{001} \rightarrow^2 A''_{000})$. The band maximum at 1.27 $\mu$m shifted slightly to a longer wavelength at higher pressure. At a He pressure of 5 torr, the quenching of $OH^*$ and $HO_2^*$ by He, $O_2$ or $H_2$ is fast enough such that they cannot be detected. After 50 ms, the peak at 1.29 $\mu$m disappeared, while the peak at 1.52 $\mu$m was absent after 100 ms.

The $O_2(^1\Sigma g^+)$ signals were converted to concentrations and plotted as functions of time (see Fig. 7). The quenching of the metastable state is evident after 20 ms (see Fig. 7(b,c)).

In order to determine the $O_2(^1\Delta g)$ concentrations at low pressures (i.e., shorter reaction time), the $HO_2^*$ contribution to the emission near 1.29 $\mu$m was removed.

Figure 6a. Spectra of $HO_2{}^*$ from 1.35 to 1.55 $\mu$m at a reaction time of 20 ms.

Figure 6b. Spectra of $O_2(^1\Delta g)$ (1.27$\mu$m) and $HO_2{}^*$ (1.29$\mu$m) as a function of time (ms) at $P = 5$ torr.

Figure 6c. Spectra of $OH^*$ from 1.38 to 1.58 $\mu$m at a reaction time of 3 ms.
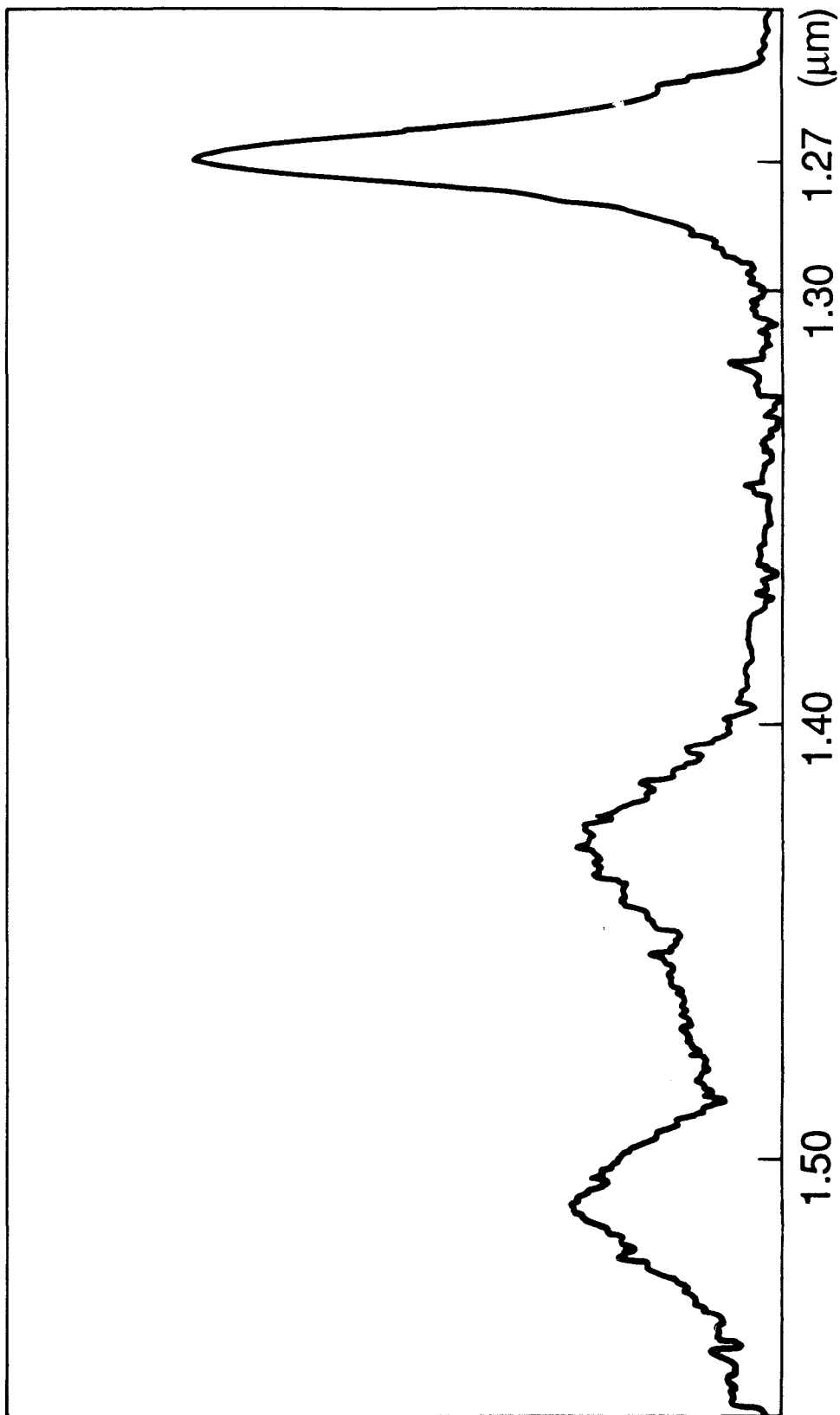
Figure 6a
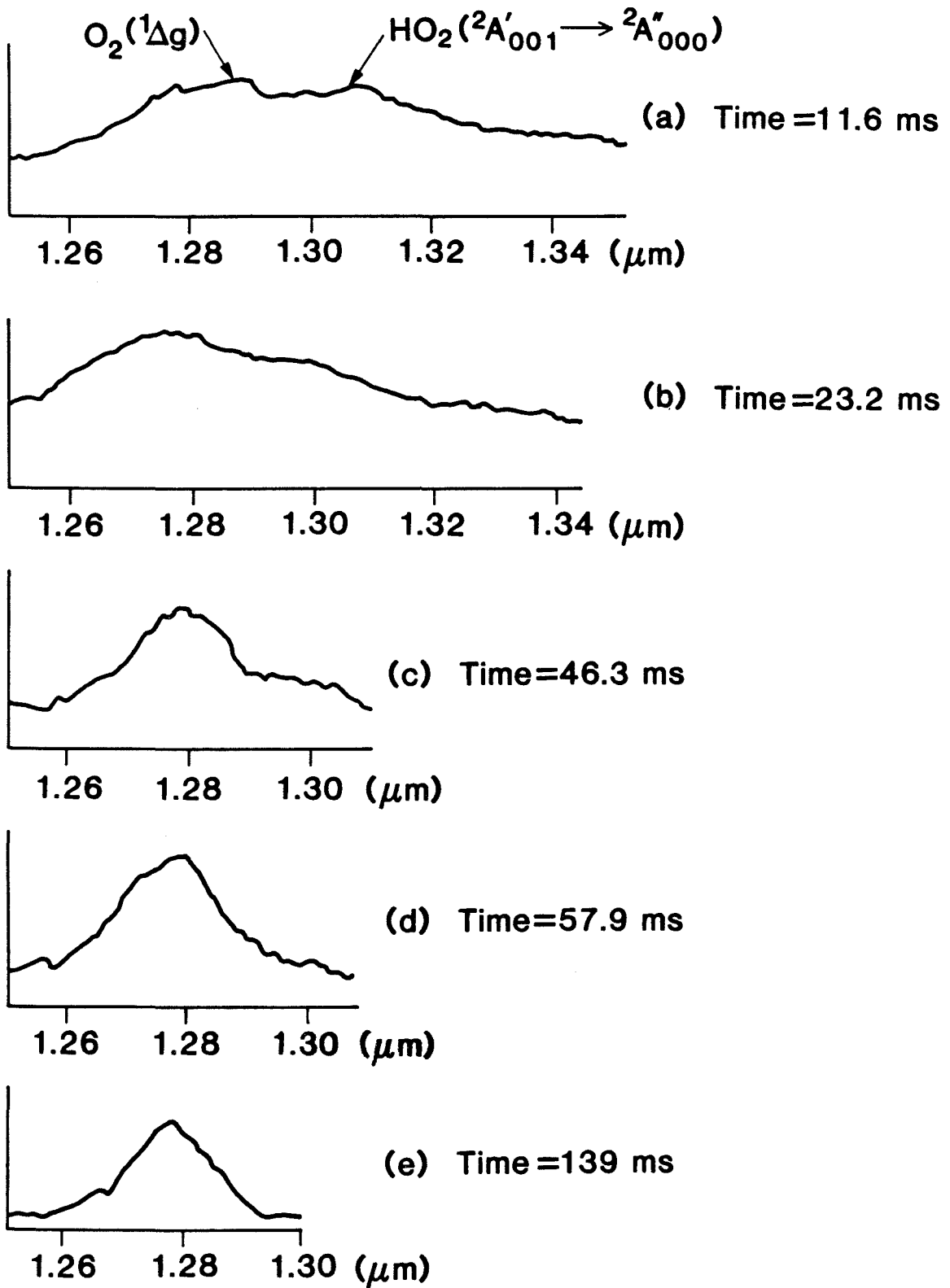
Figure 6b
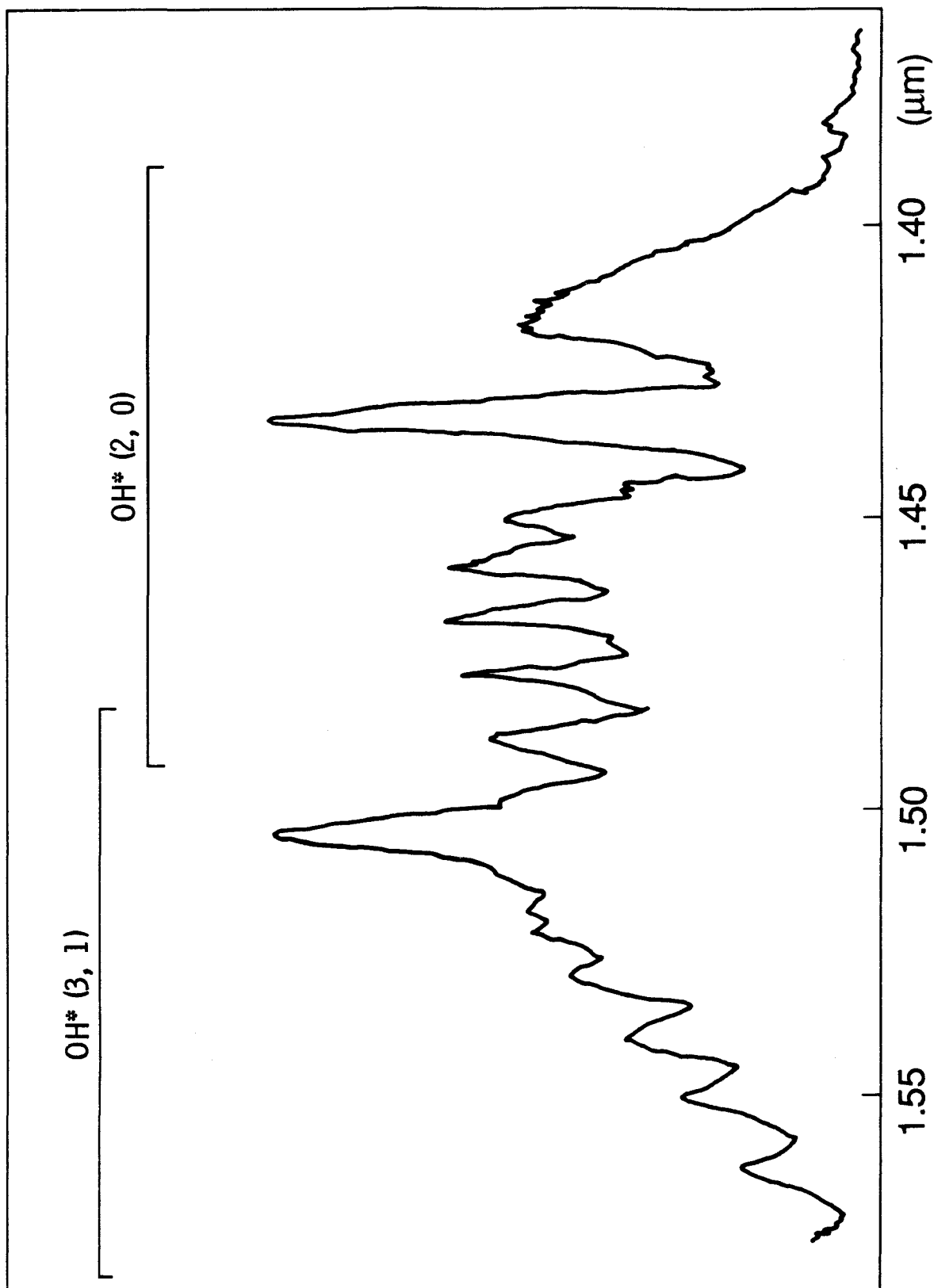
Figure 6c

This was done by drawing the shorter wavelength wing of the $HO_2^*$ peak, assuming it was symmetrical, and removing it from the $O_2(^1\Delta g)$ signal measured at $1.27\mu m$. At low pressure, the $HO_2^*$ contribution was significant relative to $O_2^*$; accordingly, a large error is associated with this deconvolution. At higher pressures or longer reaction times, both the $HO_2^*$ and the singlet oxygen were quenched.

In the $H + O_2$ system, there are many possible reactions that might produce $O_2(^1\Sigma g^+)$ and $O_2(^1\Delta g)$. Because of the complexity of this reaction system, the data were fit by computer simulations, which included a full set of reactions (Table 1).

## TABLE 1: Reactions Used in Computer Simulations.

| | Reaction | | $k^a$ | Reference |
|---|---|---|---|---|
| 1 | $H + HO_2$ | $\rightarrow$ $H_2 + O_2(^1\Sigma g^+)$ | | b |
| 2 | $H + HO_2$ | $\rightarrow$ $H_2 + O_2(^1\Delta g)$ | | b |
| 3 | $H + HO_2$ | $\rightarrow$ $H_2 + O_2$ | $7.0 \times 10^{-12}$ | c |
| 4 | $H + HO_2$ | $\rightarrow$ $2OH$ | | c |
| 5 | $H + HO_2$ | $\rightarrow$ $OH + OH^{*d}$ | $7.8 \times 10^{-11}$ | c |
| 6 | $H + HO_2$ | $\rightarrow$ $H_2O + O$ | $1.7 \times 10^{-12}$ | c |
| 7 | $H + O_2 + M$ | $\rightarrow$ $HO_2^d + M$ | $5.5 \times 10^{-32}$ | f |
| 8 | $O + OH$ | $\rightarrow$ $H + O_2$ | $3.3 \times 10^{-11}$ | f |
| 9 | $O + HO_2$ | $\rightarrow$ $OH + O_2$ | $5.9 \times 10^{-11}$ | f |
| 10 | $O + HO_2$ | $\rightarrow$ $OH + O_2(^1\Sigma g^+)$ | | b |
| 11 | $OH + OH$ | $\rightarrow$ $H_2O + O$ | $1.8 \times 10^{-12}$ | f |
| 12 | $HO_2 + HO_2$ | $\rightarrow$ $H_2O_2 + O_2$ | $1.7 \times 10^{-12}$ | f |
| 13 | $HO_2 + HO_2$ | $\rightarrow$ $H_2O_2 + O_2(^1\Sigma g^+)$ | | b |
| 14 | $OH + OH + M$ | $\rightarrow$ $H_2O_2 + M$ | $3.2 \times 10^{-28}$ | f |
| 15 | $H + H_2O_2$ | $\rightarrow$ $HO_2 + H_2$ | $2.0 \times 10^{-14}$ | f |
| 16 | $H + H_2O_2$ | $\rightarrow$ $H_2O + OH$ | $3.0 \times 10^{-14}$ | f |
| 17 | $OH + H_2O_2$ | $\rightarrow$ $H_2O + HO_2$ | $1.6 \times 10^{-12}$ | f |
| 18 | $O + H_2O_2$ | $\rightarrow$ $HO_2 + OH$ | $1.6 \times 10^{-15}$ | f |
| 19 | $OH + HO_2$ | $\rightarrow$ $H_2O + O_2$ | $1.0 \times 10^{-10}$ | g |
| 20 | $OH + HO_2$ | $\rightarrow$ $H_2O + O_2(^1\Sigma g^+)$ | | b |
| 21 | $OH + H_2$ | $\rightarrow$ $H_2O + H$ | $6.3 \times 10^{-15}$ | f |
| 22 | $O_2(^1\Sigma g^+)$ | $\rightarrow$ $O_2$ | 30 or 80 | h |

| 23 | $O_2(^1\Sigma g^+) + H$ | $\rightarrow$ | $O_2 + H$ | $5.7 \times 10^{-13}$ | h |
|----|---|---|---|---|---|
| 24 | $O_2(^1\Sigma g^+) + H_2$ | $\rightarrow$ | $O_2 + H_2$ | $7.1 \times 10^{-13}$ | h |
| 25 | $O_2(^1\Sigma g^+) + H_2O_2$ | $\rightarrow$ | $O_2 + H_2O_2$ | $1.0 \times 10^{-11}$ | i |
| 26 | $O_2(^1\Sigma g^+) + H_2O$ | $\rightarrow$ | $O_2 + H_2O$ | $5.0 \times 10^{-12}$ | j |
| 27 | $O_2(^1\Sigma g^+) + HO_2$ | $\rightarrow$ | $O_2 + HO_2$ | $1.0 \times 10^{-11}$ | i |
| 28 | $O_2(^1\Sigma g^+) + OH$ | $\rightarrow$ | $O_2 + OH$ | $1.0 \times 10^{-11}$ | j |
| 29 | $O_2(^1\Sigma g^+) + O$ | $\rightarrow$ | $O_2 + O$ | $8.0 \times 10^{-14}$ | j |
| 30 | $O_2(^1\Sigma g^+) + O_2$ | $\rightarrow$ | $O_2 + O_2$ | $3.8 \times 10^{-17}$ | j |
| 31 | $O_2(^1\Delta g) + H$ | $\rightarrow$ | $O_2 + H$ | $2.0 \times 10^{-14}$ | j |
| 32 | $O_2(^1\Delta g) + H$ | $\rightarrow$ | $OH + O$ | $1.0 \times 10^{-14}$ | k |
| 33 | $O_2(^1\Delta g) + H_2$ | $\rightarrow$ | $O_2 + H_2$ | $4.0 \times 10^{-18}$ | j |
| 34 | $O_2(^1\Delta g) + O_2$ | $\rightarrow$ | $O_2 + O_2$ | $1.0 \times 10^{-18}$ | j |
| 35 | $O_2(^1\Delta g) + O_2(^1\Delta g)$ | $\rightarrow$ | $O_2 + O_2(^1\Sigma g^+)$ | $2.0 \times 10^{-18}$ | j |
| 36 | $O$ | $\rightarrow$ | product[1] | 2 | c |
| 37 | $H$ | $\rightarrow$ | product[1] | 2 | h |
| 38 | $HO_2$ | $\rightarrow$ | products[1] | 5 | c |
| 39 | $OH$ | $\rightarrow$ | products[1] | 10 | c |
| 40 | $HO_2^*$ | $\rightarrow$ | products[1] | 100 | k |
| 41 | $HO_2^*$ | $\rightarrow$ | $HO_2$ | 500 | m |
| 42 | $HO_2^* + M$ | $\rightarrow$ | $HO_2 + M$ | $4.5 \times 10^{-12}$ | k |
| 43 | $HO_2^* + H_2$ | $\rightarrow$ | $HO_2 + H_2$ | $1.4 \times 10^{-11}$ | n |
| 44 | $HO_2^* + O_2$ | $\rightarrow$ | $HO_2 + O_2$ | $1.2 \times 10^{-11}$ | k |
| 45 | $HO_2^* + O_2$ | $\rightarrow$ | $HO_2 + O_2(^1\Sigma g^+)$ | | b |
| 46 | $HO_2^* + O_2$ | $\rightarrow$ | $HO_2 + O_2(^1\Delta g)$ | $1.2 \times 10^{-13}$ | o |
| 47 | $HO_2^* + H$ | $\rightarrow$ | $OH + OH$ | $3.3 \times 10^{-11}$ | k |
| 48 | $HO_2^* + H$ | $\rightarrow$ | $H_2O + O$ | $1.0 \times 10^{-12}$ | k |

| 49 | $HO_2^* + H$ | $\rightarrow$ | $H_2 + O_2(^1\Sigma g^+)$ | | b |
|---|---|---|---|---|---|
| 50 | $HO_2^* + H$ | $\rightarrow$ | $H_2 + O_2(^1\Delta g)$ | | b |
| 51 | $HO_2^* + O_2(^1\Delta g)$ | $\rightarrow$ | $O_2 + O_2 + H$ | $1.7 \times 10^{-10}$ | k |
| 52 | $HO_2 + O_2(^1\Delta g)$ | $\rightarrow$ | $HO_2^* + O_2$ | $1.7 \times 10^{-12}$ | k |
| 53 | $OH^*$ | $\rightarrow$ | products[l] | 50 | p |
| 54 | $OH^{*\,q}$ | $\rightarrow$ | $OH$ | 16 | r |
| 55 | $OH^* + H$ | $\rightarrow$ | $OH + H$ | $3.0 \times 10^{-10}$ | p |
| 56 | $OH^* + H$ | $\rightarrow$ | $O + H_2$ | $2.0 \times 10^{-11}$ | c |
| 57 | $OH^* + H_2O$ | $\rightarrow$ | $OH + H_2O$ | $5.0 \times 10^{-11}$ | c |
| 58 | $OH^* + O$ | $\rightarrow$ | $H + O_2$ | $1.0 \times 10^{-10}$ | s |
| 59 | $OH^* + O$ | $\rightarrow$ | $H + O_2(^1\Sigma g^+)$ | | b |
| 60 | $OH^* + O$ | $\rightarrow$ | $H + O_2(^1\Delta g)$ | | b |
| 61 | $OH^* + O_2$ | $\rightarrow$ | $OH + O_2$ | $1.4 \times 10^{-13}$ | t |
| 62 | $OH^* + H_2$ | $\rightarrow$ | $H + H_2O$ | $1.0 \times 10^{-14}$ | c |
| 63 | $OH^* + HO_2$ | $\rightarrow$ | $H_2O + O_2$ | $6.4 \times 10^{-11}$ | c |
| 64 | $OH^* + OH$ | $\rightarrow$ | $H_2O + O$ | $1.0 \times 10^{-10}$ | c |
| 65 | $OH^* + OH^*$ | $\rightarrow$ | $H_2O + O$ | $1.0 \times 10^{-10}$ | c |
| 66 | $OH^* + H_2O_2$ | $\rightarrow$ | $OH + H_2O_2$ | $1.5 \times 10^{-11}$ | c |
| 67 | $OH^* + H_2O_2$ | $\rightarrow$ | $H_2O + HO_2$ | $1.7 \times 10^{-12}$ | c |
| 68 | $H + CO + M$ | $\rightarrow$ | $HCO + M$ | $1.1 \times 10^{-34}$ | u |
| 69 | $CO + OH$ | $\rightarrow$ | $CO_2 + H$ | $1.5 \times 10^{-13}$ | f |
| 70 | $HCO + H$ | $\rightarrow$ | $H_2 + CO$ | $1.2 \times 10^{-10}$ | u |
| 71 | $HCO + O_2$ | $\rightarrow$ | $CO + HO_2$ | $5.5 \times 10^{-12}$ | f |
| 72 | $O_2(^1\Sigma g^+) + CO$ | $\rightarrow$ | $O_2 + CO$ | $4.5 \times 10^{-15}$ | j |
| 73 | $O_2(^1\Sigma g^+) + CO_2$ | $\rightarrow$ | $O_2 + CO_2$ | $4.6 \times 10^{-13}$ | j |
| 74 | $O_2(^1\Delta g)$ | $\rightarrow$ | $O_2$ | | b |

[a] Rate constant at 295 K with units of $s^{-1}$, $cm^3$ $s^{-1}$, and $cm^6$ $s^{-1}$ for first-, second-, and third-order reactions, respectively.

[b] Estimated by fitting experimental concentration profiles.

[c] Keyser, 1986.

[d] OH* is OH in the $\nu = 1$, 2, or 3 vibrational level of the ground electronic state.

[e] The product was considered to be 100% $HO_2$* in certain simulations.

[f] DeMore *et al.*, 1985.

[g] Keyser, 1988.

[h] Measured in this study.

[i] Keyser *et al.*, 1985.

[j] Wayne, 1985.

[k] Hack and Kurzke, 1986.

[l] Wall loss.

[m] Langhoff and Jaffe, 1979.

[n] Glaschik–Schimpf *et al.*, 1983.

[o] Podolske and Johnston, 1983.

[p] Spencer and Glass, 1976.

[q] The measured radiative lifetime was for the $\nu = 9$ state, not for the $\nu = 1 - 3$ states we observed.

[r] Potter *et al.*, 1971.

[s] Spencer and Glass, 1977.

[t] Streit and Johnston, 1976.

[u] Baulch *et al.*, 1976.

Figure 7. Concentrations of $O_2(^1\Sigma g^+)$ ($cm^{-3}$) as a function of reaction time (ms)

for a) $P = 1.05$ torr, $[M] = 3.1 \times 10^{16}$ $cm^{-3}$, $[H] = 4.8 \times 10^{12}$ $cm^{-3}$;

b) $P = 2.10$ torr, $[M] = 6.5 \times 10^{16}$ $cm^{-3}$, $[H] = 9.6 \times 10^{12}$ $cm^{-3}$; and

c) $P = 4.5$ torr, $[M] = 1.3 \times 10^{17}$ $cm^{-3}$, $[H] = 2.1 \times 10^{13}$ $cm^{-3}$ for various

$[O_2]$.
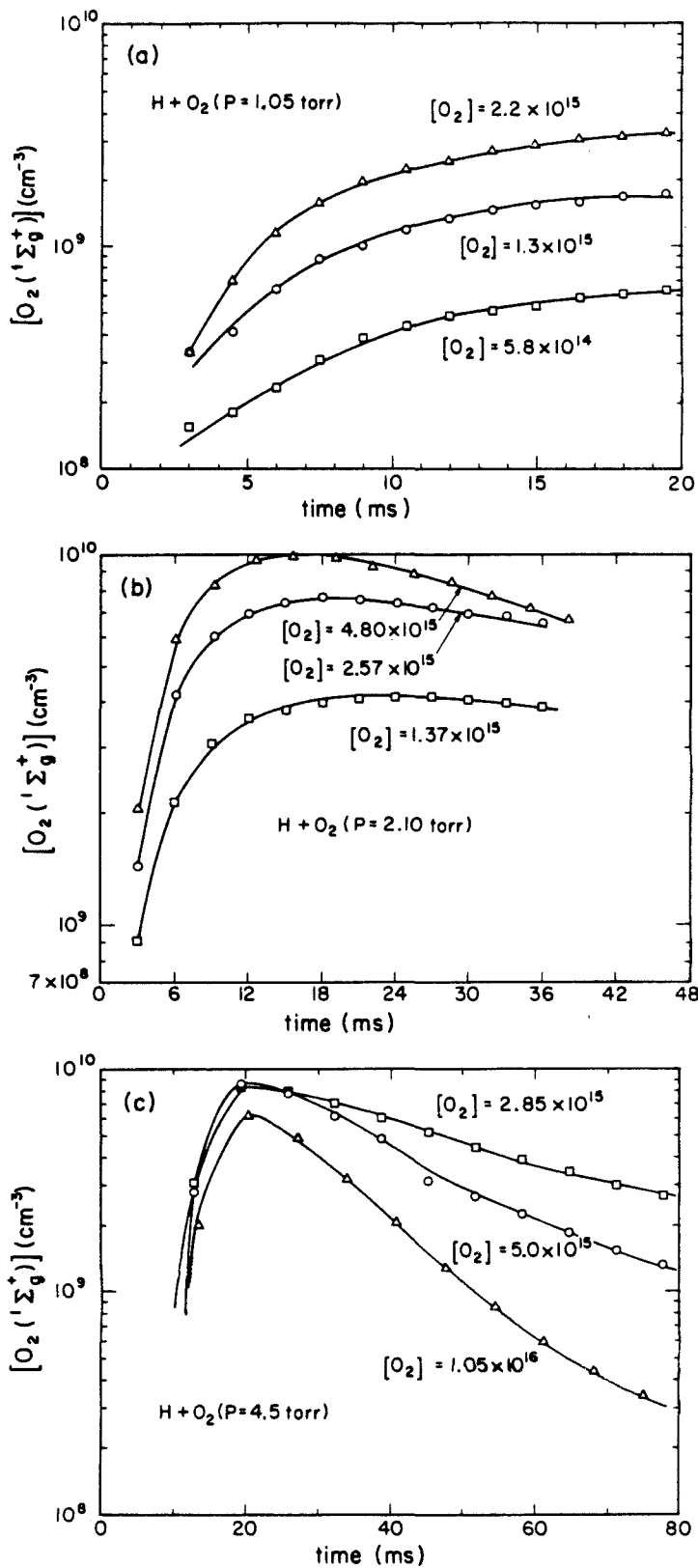
Figure 7

All simulations were done using a one–box model derived from the Caltech one–dimensional photochemical model by Allen *et al.* (1981). The concentrations of all species present were calculated in a time–stepping mode. The unknown rate constants of the reactions forming the singlet states were varied to obtain the best overall fits. The reactions involving $HO_2^*$ and $OH^*$ were included because of their presence in the spectra. The strategy of this study was to evaluate the contribution from various reactions producing $O_2(^1\Sigma g^+)$ and $O_2(^1\Delta g)$, by changing the rate constants and trying to fit the data. We concluded that reaction

$$H + HO_2 \quad \rightarrow \quad O_2 + H_2$$
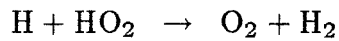
is the major source of singlet oxygen in this system. We have not completely ruled out the possibility of including a contribution from

$$OH + HO_2 \quad \rightarrow \quad O_2 + H_2O.$$
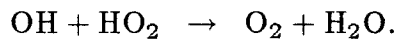
Table 2 is a summary of the data sets and the simulation results. The rate constant of reaction (1) was varied in order to fit the shape of the $O_2(^1\Sigma g^+)$ growth curves, as well as the steady–state concentrations. We added a contribution from reaction (20), keeping in mind the difficulties in modeling the results, because of the large uncertainty in the $[O_2(^1\Sigma g^+)]$ values (up to a factor of two). The average rate constant used was $k_1 = (1.85 \pm 0.14) \times 10^{-12}$ cm$^3$ s$^{-1}$ (with $k_{20} = (1.62 \pm 0.34) \times 10^{-11}$ cm$^3$ s$^{-1}$), which corresponds to a yield of $2.1 \pm 0.2\%$ (the error represents one standard deviation). It is clear that since these experiments were not specifically designed to measure the yield of $O_2(^1\Sigma g^+)$ from $OH + HO_2$, a yield cannot be obtained from these results. Nevertheless, inclusion of reaction (20) improves the fit considerably.

TABLE 2: Summary of Computer Simulations.

| P (Torr) | $\bar{v}$ (cm/s) | [H] ($cm^{-3}$) | [$O_2$] ($cm^{-3}$) | $k_1{}^a$ ($cm^3$ $s^{-1}$) |
|---|---|---|---|---|
| 1.040 | 3250 | $4.9 \times 10^{12}$ | $5.8 \times 10^{14}$ | $1.6 \times 10^{-12}$ |
| 1.060 | 3263 | $4.9 \times 10^{12}$ | $1.3 \times 10^{15}$ | $1.7 \times 10^{-12}$ |
| 1.070 | 3330 | $4.8 \times 10^{12}$ | $2.2 \times 10^{15}$ | $1.8 \times 10^{-12}$ |
| 1.002 | 3322 | $6.1 \times 10^{12}$ | $5.7 \times 10^{14}$ | $2.0 \times 10^{-12}$ |
| 1.023 | 3327 | $6.1 \times 10^{12}$ | $1.3 \times 10^{15}$ | $2.0 \times 10^{-12}$ |
| 1.057 | 3344 | $6.0 \times 10^{12}$ | $2.6 \times 10^{15}$ | $1.8 \times 10^{-12}$ |
| 1.997 | 1676 | $8.1 \times 10^{12}$ | $1.1 \times 10^{15}$ | $2.0 \times 10^{-12}$ |
| 2.099 | 1632 | $8.1 \times 10^{12}$ | $2.7 \times 10^{15}$ | $2.0 \times 10^{-12}$ |
| 2.263 | 1572 | $8.1 \times 10^{12}$ | $5.5 \times 10^{15}$ | $2.0 \times 10^{-12}$ |
| 4.048 | 832 | $1.5 \times 10^{13}$ | $3.1 \times 10^{15}$ | $1.7 \times 10^{-12}$ |
| 4.238 | 809 | $1.5 \times 10^{13}$ | $5.7 \times 10^{15}$ | $1.8 \times 10^{-12}$ |
| 4.574 | 775 | $1.5 \times 10^{13}$ | $1.1 \times 10^{16}$ | $1.8 \times 10^{-12}$ |

[a] $k_{20} = 1.6 \times 10^{-11}$ $cm^3$ $s^{-1}$ was adopted for these calculations.

The simulations of the $O_2(^1\Delta g)$ data were more difficult because of the larger uncertainty in its concentrations. Nevertheless, we attempted to fit our data with a simple mechanism of formation of $O_2(^1\Delta g)$ from reaction

$$H + HO_2 \quad \rightarrow \quad O_2(^1\Delta g) + H_2 \tag{6}$$
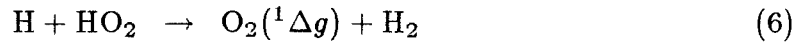
and destruction by quenching with atomic hydrogen:

$$O_2(^1\Delta g) + H \quad \rightarrow \quad O_2 + H. \tag{31}$$
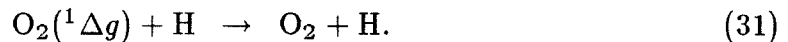
Figure 8a represents a simulation under these conditions, with an adopted rate constant for (2) of $k_2 = 4.15 \times 10^{-12}$ cm$^3$ s$^{-1}$ (Keyser, 1986). It is clear from Figure 8a that we underestimated the amount of $O_2(^1\Delta g)$ below 20 ms, but overestimated the concentration above that time. If we invoke, as we did for the $O_2(^1\Sigma g^+)$ case, the reaction

$$OH + HO_2 \quad \rightarrow \quad O_2(^1\Delta g) + H_2,$$
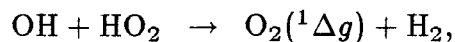
we increase the discrepancy at longer reaction times. It is therefore difficult to ascribe the observed behavior of $O_2(^1\Delta g)$ to a simple chemical scheme. The details of the simulation results are found in the next section.

Figure 8. a) Concentrations ($cm^{-3}$) as a function of reaction time (ms) of certain species calculated by simulation with $k_2 = 4.15 \times 10^{-12}$ $cm^3$ $s^{-1}$ and no production of OH and $HO_2$ excited states. The triangles are the data for $P = 4.0$ torr, $[M] = 1.3 \times 10^{17}$ $cm^{-3}$, $[O_2] = 1.67 \times 10^{15}$ $cm^{-3}$ and $[H] = 9.8 \times 10^{13}$ $cm^{-3}$. b) Same data as in a) but simulations with $k_2 = 4.15 \times 10^{-12}$ $cm^3$ $s^{-1}$, $k_{46} = 6.0 \times 10^{-12}$ $cm^3$ $s^{-1}$, and $k_{73} = 50$ $s^{-1}$.
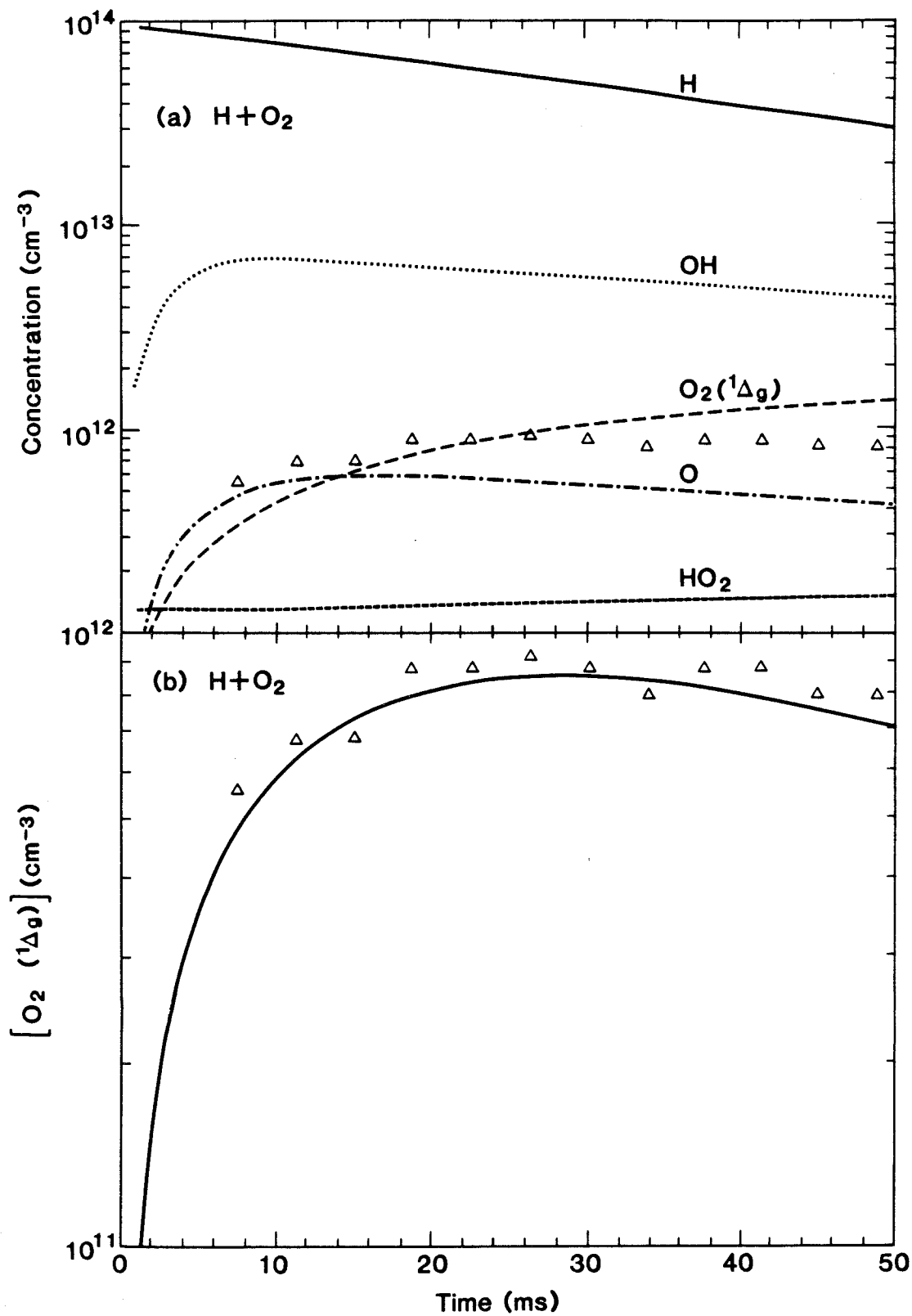
Figure 8

## 2.4  Discussion

As mentioned previously, our measurement of the quenching of $O_2(^1\Sigma g^+)$ by $H_2$ is in excellent agreement with the work of Choo and Leu (1985) and others (see Table 1 of Choo and Leu, 1985); therefore, we trust our new experimental apparatus and calibrations.

In the case of quenching by H, the scatter in the data because of inherent experimental difficulties, yields a large error bar. Most of the scatter in the data comes from the [H] measurements. The titration with NOCl contributed about 20% of the error for these measurements. Also, the dissociation efficiency of the microwave discharge and the wall loss varied, adding a few percent of uncertainty in the results. Nevertheless, for our modeling purposes, it was important to determine this rate, because of the large concentration of H atoms in the system. Sensitivity studies showed that changing this quenching rate constant by a factor of two did not affect the results for the yields of $O_2(^1\Sigma g^+)$ and $O_2(^1\Delta g)$.

The list of reactions (Table 1) needed to describe the system is long because of the presence of the excited states of $HO_2$ and OH, and their related reactions. If we assumed that $O_2(^1\Sigma g^+)$ was formed only in reaction (1), we would have significant problems fitting the observed data. We therefore investigated other possible formation processes such as:

$$HO_2 + O \rightarrow O_2(^1\Sigma g^+) + OH \tag{10}$$

$$HO_2 + HO_2 \rightarrow O_2(^1\Sigma g^+) + H_2O_2 \tag{13}$$

$$HO_2 + OH \rightarrow O_2(^1\Sigma g^+) + H_2O \tag{20}$$

$$HO_2^* + O_2 \rightarrow O_2(^1\Sigma g^+) + HO_2 \tag{45}$$

$$HO_2{}^* + H \quad \rightarrow \quad O_2(^1\Sigma g^+) + H_2 \tag{49}$$

$$OH^* + O \quad \rightarrow \quad O_2(^1\Sigma g^+) + H. \tag{59}$$
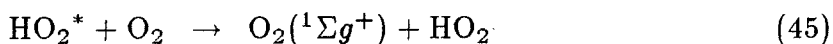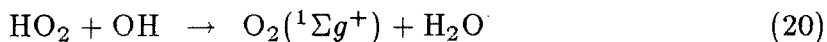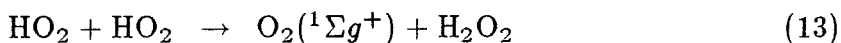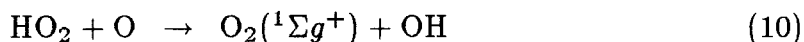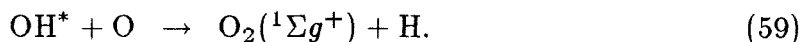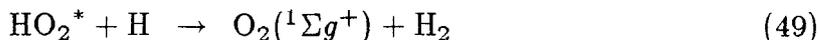
Reactions (10) and (13) proved to have little effect on the $O_2(^1\Sigma g^+)$ yield because of the low concentrations of O and $HO_2$ in the system (see Fig. 9a). On the other hand, reaction (20) could not be ignored. The OH concentration, which rose as reaction time increased in the experiment, was substantial at all times. Figure 9c shows an attempt at fitting a data set at $P = 1$ torr, where $O_2(^1\Sigma g^+)$ was formed only by reaction (1). Figure 9b is the same data set, with a model curve obtained after including reaction (20) only. There is no doubt that reaction (20) alone cannot fit both the temporal behavior and the steady–state concentration of $O_2(^1\Sigma g^+)$. At longer times, when OH becomes even more abundant than H, reaction (20) might become important. It was impossible to fit the data at $P = 2$ and 4 torr without considering reaction (20).

CO was added to the reaction system in an attempt to remove the contribution from OH in the formation of $O_2(^1\Sigma g^+)$. In these experiments, $[CO] \simeq 4 \times 10^{15}$ $cm^{-3}$ was added downstream of the mixing point for H and $O_2$, and the $O_2(^1\Sigma g^+)$ and $O_2(^1\Delta g)$ signals, with and without addition of CO, were compared. In order to fit the data, after assuming an atomic H concentration based on the previous experiments, we fit the data with CO by reducing $k_1$ to $1.0 \times 10^{-12}$ $cm^3$ $s^{-1}$, which corresponds to a branching ratio of 0.012. This fact suggests that OH might be a significant contributor to the $O_2(^1\Sigma g^+)$ yield, and therefore reaction (20) should be considered.

Figure 9. Concentrations ($cm^{-3}$) as a function of reaction time (ms) of certain species calculated by simulations with a) $k_1 = 1.60 \times 10^{-12}$ $cm^3$ $s^{-1}$ and $k_{20} = 2.0 \times 10^{-11}$ $cm^3$ $s^{-1}$; b) $k_1 = 0$ and $k_{20} = 1.0 \times 10^{-10}$ $cm^3$ $s^{-1}$; c) $k_1 = 1.6 \times 10^{-12}$ $cm^3$ $s^{-1}$, and $k_{20} = 0$. The triangles are the data for $P = 1.0$ torr; $[M] = 3.12 \times 10^{16}$ $cm^{-3}$; $[O_2] = 5.76 \times 10^{14}$ $cm^{-3}$; and $[H] = 4.9 \times 10^{12}$ $cm^{-3}$.
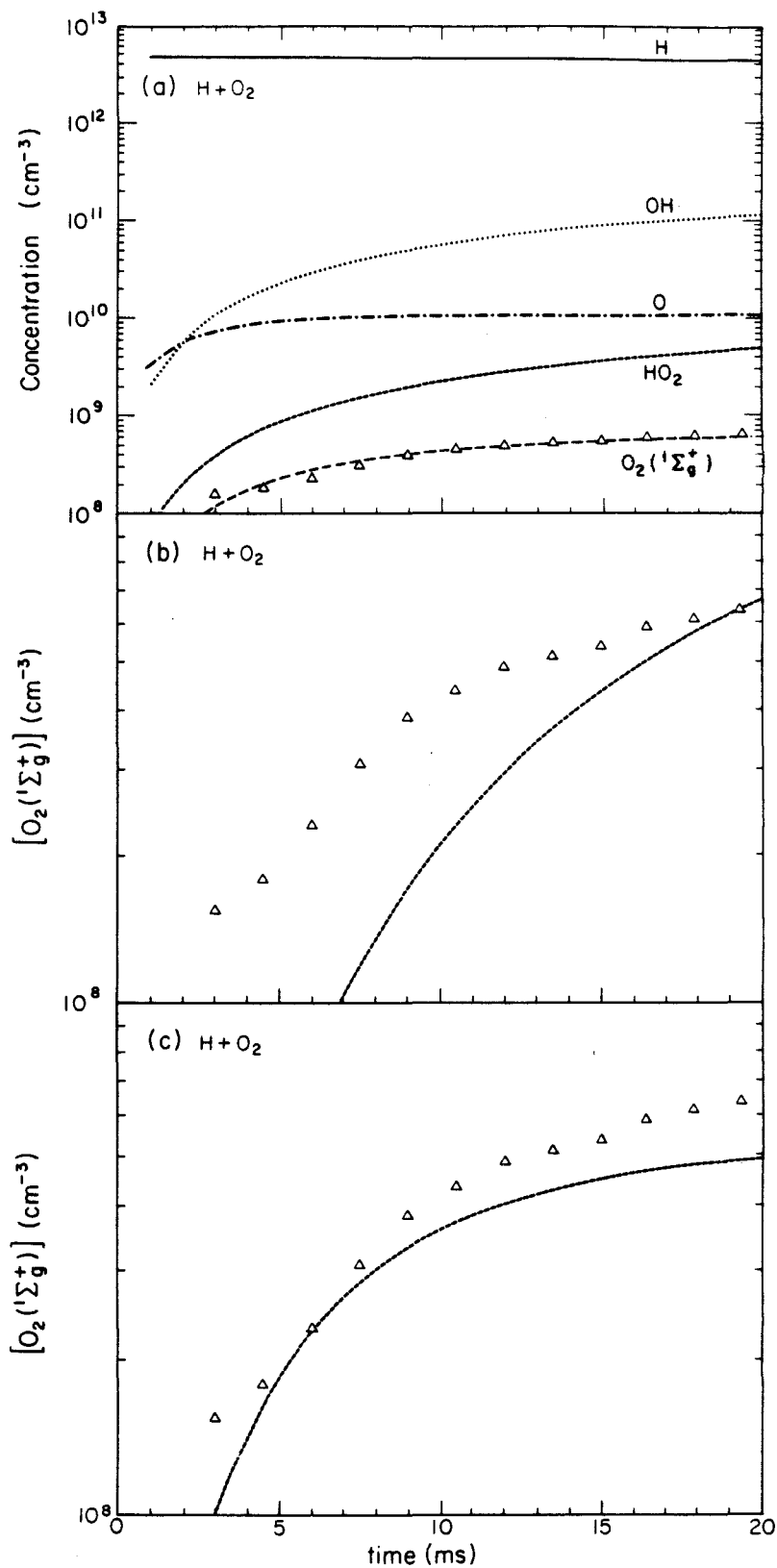
Figure 9

We conclude that the $O_2(^1\Sigma g^+)$ data are best fit by considering reaction (1) and possibly reaction (20), whose effect we could not entirely exclude. By doing this, we obtain a branching ratio of 0.021 for reaction (1), which corresponds to $k_1 = 1.85 \times 10^{-12}$ cm$^3$ s$^{-1}$ (with $k_{20} = 1.62 \times 10^{-11}$ cm$^3$ s$^{-1}$). In contrast, if $k_{20} = 0$, the best fit is obtained with $k_1 = 2.3 \times 10^{-12}$ cm$^3$ s$^{-1}$ (2.7% yield) and if $k_1 = 0$ then $k_{20} = 7.0 \times 10^{-11}$ cm$^3$ s$^{-1}$ (63% yield), but the shapes of the experimental curves are not fully reproduced (see Figure 9). The uncertainty in the $[O_2(^1\Sigma g^+)]$ and in the exact time of the reaction, because of the complicated geometry of the detection zone, leads to the ambiguity as to whether or not reaction (20) is necessary to explain the data. To be consistent with the measurements of Keyser *et al.* (1985), who gave an upper limit of $1 \times 10^{-3}$ for the $O_2(^1\Sigma g^+)$ yield from $OH + HO_2$, we should neglect the contribution from reaction (20) and consider only $H + HO_2$ as the $O_2(^1\Sigma g^+)$ source.

Reactions (45), (49) and (59) all involve excited states of $HO_2$ and $OH$, which were seen in the spectra. Because so little is known about the formation of these excited states as well as about the quenching and reactivity of each excited state, we considered only more general forms of $HO_2^*$ and $OH^*$ and their effect on the production of $O_2(^1\Sigma g^+)$.

We assumed that $HO_2^*$ was produced with 100% yield from reaction (7) with $\Delta H^o_{f298} = -207.5$ kJ/mol, and from the energy transfer reaction with $O_2(^1\Delta g)$ (52) with $\Delta H^o_{f298} = -10.2$ kJ/mol. The motivation for these assumptions was derived from Holstein *et al.* (1983), who studied the $H + O_2$ system and suggested these two mechanisms to explain the highly excited $HO_2$ in their experiments. They even proposed that two $O_2(^1\Delta g)$ are needed to excite the $HO_2$. Giachardi, Harris and Wayne (1975) also observed electronically and vibrationally excited $HO_2$ in

the $H + O_2$ system. The effect of $HO_2^*$ in this system was negligible with regard to $O_2(^1\Sigma g^+)$ yields. The rate constant for the reactions involving $HO_2^*$ (47–52) were taken from Hack and Kurzke (1984, 1986), and the quenching rate constants (41–44) were obtained from literature values (Hack and Kurzke, 1986; Langhoff and Jaffe, 1979; Glaschik–Schimpf et al., 1983). The wall losses of the excited $HO_2$ and OH were estimated. The rate constants of reactions (45) and (49) were varied, but had no effect on the results.

In order to consider the effect of $OH^*$ on $O_2(^1\Sigma g^+)$ yields, we assumed that 90% of the $H + HO_2$ reaction yields $OH^*$, as suggested by Keyser (1986) and Charters and Polanyi (1960). The radiative lifetime of $(6.4 \pm 1.4) \times 10^{-2}$ s was taken from Potter et al. (1971). Addition of the $OH^*$ contribution to the model did not have a significant effect on the $O_2(^1\Sigma g^+)$ results. Reaction (59) was suggested as a source of $O_2(^1\Sigma g^+)$, but was considered as unimportant, because of the low concentration of O atoms.

Although the above analysis indicates the lack of significance of $OH^*$ and $HO_2^*$ concerning $O_2^*$ yields in the $H + O_2$ system, the exact mechanism, states involved, and rate constants for all the $OH^*$ and $HO_2^*$ reactions are not well known. It is therefore premature to completely rule out any effect from them.

There are two published measurements of $O_2(^1\Sigma g^+)$ yields from reaction (1): Hislop and Wayne (1977) ($2.8 \times 10^{-4}$) and Keyser et al. (1985) ($< 8 \times 10^{-3}$). Our yields from $H + HO_2$ are larger than in both of these references. In the case of Keyser et al. (1985), their experiments involved formation of $HO_2$ from $F + H_2O_2 \rightarrow HF + HO_2$, which produced vibrationally excited HF with a large background emission in the spectral region near the $O_2(^1\Sigma g^+)$ emission. The second

major difference was the existence of $HO_2{}^*$ and $OH^*$ in our system. It is possible that chemistry involving these species is responsible for our higher $O_2(^1\Sigma g^+)$ yields.

Our model was used to simulate the results of Hislop and Wayne (1977), as well as the $O_2(^1\Delta g)$ results of Washida et al. (1978). In order to fit the hydrogen atom concentrations of Hislop and Wayne (1977), we found that $k_7$ needed to be set to $1.5 \times 10^{-32}$ cm$^6$ s$^{-1}$, a value that agrees with the value derived in their paper. We used $k_7 = 5.5 \times 10^{-32}$ cm$^3$ s$^{-1}$ (Table 1) to fit our experimental data, as suggested by DeMore et al. (1985). We obtained best fits to the $O_2(^1\Sigma g^+)$ data of Hislop and Wayne (1977), with an average $k_1$ of $2.1 \times 10^{-13}$ cm$^3$ s$^{-1}$. This gave a branching ratio of 0.002 for $O_2(^1\Sigma g^+)$, which is still ten times larger than their published value. This result did not change when we assumed, as Hislop and Wayne (1977) did, that 60% of the reaction between H and $HO_2$ yielded $O_2$ and $H_2$. The effects of changing various quenching rate constants ($k_{22}$, $k_{23}$, $k_{31}$) did not significantly alter the 0.002 branching ratio. The reason for the discrepancy between our model determination of the branching ratio based on the Hislop and Wayne (1977) data, and theirs, might be due to the assumption made by Hislop and Wayne (1977) that the $HO_2$ concentration was small. Also, the contact times of 52 and 127 ms were very long; therefore, the low yield they obtained was probably due to the rapid quenching of $O_2(^1\Sigma g^+)$. At these times, the quenching determines the $O_2(^1\Sigma g^+)$ concentration.

The $O_2(^1\Delta g)$ results are even more difficult to interpret. The $O_2(^1\Delta g)$ signal is separated from the $HO_2{}^*$ signal at 1.29 $\mu$m only at high pressure and slow flow, when the $HO_2{}^*$ has been quenched. Unfortunately, these are the same conditions under which we can model only the quenching of $O_2(^1\Delta g)$. For any information on the growth of the $O_2(^1\Delta g)$ signal, we must go to lower pressures and faster

flows, which are conditions under which $HO_2^*$ poses a significant interference to the $O_2(^1\Delta g)$ signal. We have attempted to remove the $HO_2^*$ contribution, but this method is approximate.

As in the case of $O_2(^1\Sigma g^+)$, we investigated various mechanisms of formation of $O_2(^1\Delta g)$:

$$HO_2 + H \rightarrow O_2(^1\Delta g) + H_2 \tag{2}$$

$$HO_2^* + O_2 \rightarrow O_2(^1\Delta g) + HO_2 \tag{46}$$

$$HO_2^* + H \rightarrow O_2(^1\Delta g) + H_2 \tag{50}$$

$$OH^* + O \rightarrow O_2(^1\Delta g) + H \quad . \tag{60}$$
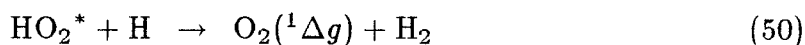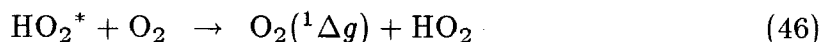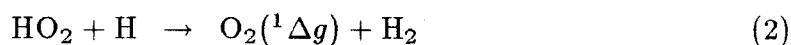
We also considered the possibility that $O_2(^1\Sigma g^+)$ was quenched to $O_2(^1\Delta g)$ by H, $H_2$, $H_2O_2$, $H_2O$, $HO_2$, and OH (1974). Reactions (50) and (60) were found to be insignificant because of the low concentrations of O, H, and the excited states of $HO_2$ and OH. The contribution of reaction (46) was not negligible and should be considered as a possibly important formation mechanism for $O_2(^1\Delta g)$. Unfortunately, there is little published information regarding this reaction. Podolske and Johnston (1983) estimated $k_{46}$ to be $1.2 \times 10^{-13}$ cm$^3$ s$^{-1}$ at 298 K. This value reduced the yield of reaction (2) from 4.7% to 2.7%. This is obviously an important effect that deserves further investigation. The quenching reactions of $O_2(^1\Sigma g^+)$ (23–28) acted to reduce the yield from reaction (2). The major problem remaining is that of the temporal behavior of $O_2(^1\Delta g)$. This can be obtained (Fig. 8b) only by assuming an unrealistically large loss rate of $O_2(^1\Delta g)$. It is nevertheless clear that $O_2(^1\Delta g)$ was formed in this system with a high yield, possibly caused by the presence of $HO_2^*$ or $OH^*$.

The modeling of Washida *et al.* 's $O_2(^1\Delta g)$ results was more straightforward.

We adjusted the values of $k_7$ and $k_4$ to be $k_7 = 1.5 \times 10^{-32}$ cm$^6$ s$^{-1}$ and $k_4 = 2.0 \times 10^{-13}$ cm$^3$ s$^{-1}$ to match their calculations. Consequently, we were able to fit the data of their Figures 2 and 3 quite well with an average $k_2$ of $1.5 \times 10^{-12}$ cm$^3$ s$^{-1}$, which corresponds to a branching ratio of 0.017, in good agreement with the value of 0.015 quoted in their paper. This argument lent credence to the validity of our model for the $O_2(^1\Delta g)$ simulations.

The interest in studying reactions of singlet oxygen formation extends further than the curiosity of the basic chemistry. Emissions of both $O_2(^1\Sigma g^+)$ and $O_2(^1\Delta g)$ in the airglow of the terrestrial planets have been reported in the literature (Wayne, 1985). The dayglow is dominated by $O_3$ photolysis, producing $O_2(^1\Delta g)$ and $O(^1D)$ at wavelengths shorter than 300 nm. In the nightglow, the $O_2(^1\Delta g)$ from photolysis persists because of its long lifetime. In the Earth's mesosphere, between 80 and 100 km, where the nightglow emissions are observed, the three major reactions forming $O_2$, which might also contribute to the $O_2(^1\Delta g)$ signal are:

$$O + O + M \;\rightarrow\; O_2 + M$$

$$H + HO_2 \;\rightarrow\; O_2 + H_2$$

$$OH + HO_2 \;\rightarrow\; O_2 + H_2O.$$
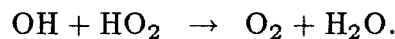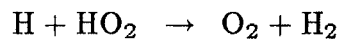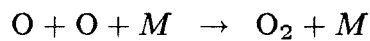
An estimate of the amount of $O_2(^1\Delta g)$ formed at 90 km by $O_3$ photolysis between 4 a.m. and 8 p.m. was made by adopting the photodissociation rate constant ($J_4 = 8 \times 10^{-3}$ s$^{-1}$) and $O_3$, $O_2$, and $N_2$ concentrations from the mesosphere and lower thermosphere model by Allen, Lunine and Yung (1984). Quenching by $O_2$ and $N_2$, as well as spontaneous emission, were included as the loss processes (Wayne, 1985). We obtained $[O_2(^1\Delta g)] = 8.4 \times 10^8$ cm$^{-3}$ at 8 p.m., which was then left to decay during the night. Until 10:10 p.m., the time of the observation by McDade

*et al.* (1987), the concentration was reduced to $[O_2(^1\Delta g)] = 8.9 \times 10^7$ cm$^{-3}$. This is below the observed value of $[O_2(^1\Delta g)] = 1.6 \times 10^8$ cm$^{-3}$ (40% error), derived from the volume emission rate at 90 km and 10:10 p.m. (McDade *et al.*, 1987). As an attempt at solving this possible discrepancy, we added a contribution from the three above reactions most likely to produce $O_2(^1\Delta g)$. We adopted a 4% yield of $O_2(^1\Delta g)$ from the atomic oxygen recombination (Wraight, 1982), a 1.5% yield from $H + HO_2$ (Washida *et al.*, 1978), and an estimated value of 0.1% from $OH + HO_2$. The concentrations of O, H, OH, $HO_2$, the total density, and the temperature at 90 km were taken from Allen, Lunine and Yung (1984). We obtained an additional $O_2(^1\Delta g)$ concentration of $4.9 \times 10^6$ cm$^{-3}$ from the above three chemical reactions, which, added to the product of photolysis ($8.9 \times 10^7$ cm$^{-3}$), yielded only $9.4 \times 10^7$ cm$^{-3}$. Within the error estimates, this value agrees with the observation. Our derivation of the yield of $O_2(^1\Delta g)$ from the experiments in this paper does not change the modeling result, because O atom is the most abundant species; therefore, the recombination of atomic oxygen is believed to be the most important reaction for producing $O_2(^1\Delta g)$ in the atmosphere.

In summary, it is interesting to investigate the yields of singlet oxygens in the $OH^*$ and $HO_2{}^*$ reactions by using direct experimental techniques. The branching ratios of upper states of molecular oxygen in the $O + O + M$ reaction and the relaxation processes of these excited species are also valuable. Finally, future observations of singlet oxygens need to be conducted with the simultaneous measurements of atoms, free radicals, and the other excited molecules in order to understand the nightglow mechanism in the planetary atmosphere.

## Acknowledgements

# References

Allen, M., Y.L. Yung, and J.W. Waters, *J. Geophys. Res.*, **86**, 3617, 1981.

Allen, M., J.I. Lunine and Y.L. Yung, *J. Geophys. Res.*, **89**, 4841, 1984.

Baulch, D.L., D.D. Drysdale, J. Duxbury, and S.J. Grant, *Evaluated Kinetic Data for High Temperature Reactions, Vol 3: Homogeneous Gas Phase Reactions of the $O_2$–$O_3$ system, the $CO$–$O_2$–$H_2$ System, and of Sulfur–containing* s. Butterworths, London, 1976.

Charters, P.E. and J.C. Polanyi, *Can. J. Chem.*, **38**, 1742, 1960.

Choo, K.Y. and M.T. Leu, *Int. J. Chem. Kinet.*, **17**, 1155, 1985.

DeMore, W.B., J.J. Margitan, M.J. Molina, R.T. Watson, D.M. Golden, R.F. Hampson, M.J. Kurylo, C.J. Howard, and A.R. Ravishankara, Jet Propulsion Laboratory, California Institute of Technology, Pasadena, CA, JPL Publication No. 85–37, 1985; and Baulch, D.L., R.A. Cox, R.F., Jr., Hampson, J.A. Kerr, J. Troe, and R.T. Watson, *J. Phys. Chem. Ref. Data*, **33**, 1259, 1984; and Hampson, R.F., Federal Aviation Administration Report No. FAA–EE–80–17, Washington, DC, 1980.

Fontijn, A., C.B. Meyer, and H.I. Schiff, *J. Chem. Phys.*, **40**, 64, 1964.

Giachardi, D.J., G.W. Harris and R.P. Wayne, *Chem. Phys. Lett.*, **32**, 586, 1975.

Glaschik-Schimpf, I., W. Hans, and U. Schurath, **84**, Bundebtagung, Bielefeld, 1983.

Golde, M.F., A.E. Roche, and F. Kaufman, *J. Chem. Phys.*, **59**, 3953, 1973.

Hack, W. and H. Kurzke, *Chem. Phys. Lett.*, **104**, 93, 1984.

Hack, W. and H. Kurzke, *J. Phys. Chem.*, **90**, 1900, 1986.

Hislop, J.R. and R.P. Wayne, *J. Chem. Soc., Faraday Trans. II*, **73**, 506, 1977.

Holstein, K.J., E.H. Fink, J. Wildt, R. Winter , and F. Zabel, *J. Phys. Chem.*, **87**, 3943, 1983.

Keyser, L.F., K.Y. Choo, and M.T. Leu, *Int. J. Chem. Kinet .*, **17**, 1169, 1985.

Keyser, L.F., *J. Phys. Chem.*, **90** , 2994, 1986.

Keyser, L.F., *J. Phys. Chem.*, **92** , 1193, 1988.

Langhoff, S.R. and R.L. Jaffe, *J. Chem. Phys.*, **71**, 1474, 1979.

Leu, M.T. and R.H. Smith, *J. Phys. Chem.*, **85**, 2570, 1981.

Leu, M.T., *J. Phys. Chem.*, **88**, 1394, 1984.

McDade, I.C., E.J. Llewellyn and R.G.H. Greer, *Planet. Space Sci.*, **35**, 1541, 1987.

Ogryzlo, E.A. and B.A. Thrush, *Chem. Phys. Lett.*, **24**, 314, 1974.

Podolske, J.R. and H.S. Johnston, *J. Phys. Chem.*, **87**, 628, 1983.

Potter, Jr., A.E., R.N. Coltharp, and S.D. Worley, *J. Chem. Phys.*, **54**, 992, 1971.

Spencer, J.E. and G.P. Glass, *Chem. Phys.*, **15**, 35, 1976.

Spencer, J.E. and G.P. Glass, *Int. J. Chem. Kinet.*, **9**, 111, 1977.

Streit, G.E. and H.S. Johnston, *J. Chem . Phys.*, **64**, 95, 1976.

Vanpee, M., K.D. Hill, and W.R. Kineyko, *A.I.A.A. J.*, **9**, 135, 1971.

Washida, N., H. Akimoto, and M. Okuda, *J. Phys. Chem.*, **82**, 18, 1978.

Wayne, R.P., *CRC Press, Physical–Chemical Aspects*, **I**, 81, 1985.

Wraight, P.C., *Planet. Space Sci.*, **30**, 251, 1982.

# PAPER III

# Barotropic Instability of Mid–latitude Zonal Jets on Mars, Earth and Venus

# Barotropic Instability of Mid–latitude Zonal Jets
# on Mars, Earth and Venus

Diane V. Michelangeli and Richard W. Zurek[1]

Division of Geological and Planetary Sciences

California Institute of Technology

Pasadena, California   91125

and

Lee S. Elson

Jet Propulsion Laboratory

California Institute of Technology

Pasadena, California   91109

[1] Visiting Associate Professor. Permanent Affiliation: Jet Propulsion Laboratory, California Institute of Technology, Pasadena, California 91109.

## ABSTRACT

We have used a linearized nondivergent barotropic vorticity model on a sphere to intercompare the fastest growing, barotropically unstable wave modes computed for zonal jets at high latitudes in the middle atmospheres of Venus, Earth, and Mars. Such zonal jets have been observed in the wintertime stratosphere on Earth and have been inferred from remotely-sensed temperatures in the Venus middle atmosphere and in the wintertime Martian atmosphere. The comparison was done by extending the results of Hartmann (1983) for his simple analytic profile of a latitudinally varying terrestrial zonal wind to zonal wind profiles characterized by the larger Rossby numbers $Ro$ appropriate to Mars and Venus. As Hartmann's results suggested, the fastest growing barotropic waves continue to grow more quickly as $Ro$ increases. Eventually, the fastest growing mode shifts from a zonal wavenumber $k = 1$ to a $k = 2$ mode, both located on the poleward flank of the high-latitude jet. However, for somewhat higher Rossby numbers, the $k = 2$ mode on the equatorward side of the zonal jet becomes the fastest growing planetary-scale barotropic mode, and this transition is marked by a discontinuous shift to longer wave periods. The Venus high-latitude zonal jet appears remarkably close to this transition $Ro$. For each of the three planets, satellite-borne instruments have detected wave patterns in the thermal radiance field in the vicinity of the high-latitude zonal jets. As reported earlier for the terrestrial wintertime stratosphere by Hartmann and for Venus by Elson (1982), these observed waves have characteristics similar to those computed for the fastest growing barotropic modes. For Mars, we find that such modes would have zonal wavenumbers 1 or 2, with $e$-folding times of 2–3 days and periods of 0.75–2.5 days; the longer period, $k = 2$ equatorward mode would dominate for the faster and narrower zonal jets. A poleward mode with $k = 1$ and a period of 1.2 days is the barotropic mode most likely to be consistent with the

Mariner 9 IRIS observations of thermal waves above the 1 mb ($\sim$ 20 km) level in the Martian atmosphere.

## 3.1 Introduction

Recent analyses of satellite radiance data have indicated the presence of planetary–scale waves in the middle atmospheres of Earth (Venne and Stanford, 1979, 1982), Venus (Taylor *et al.*, 1980), and Mars (Conrath, 1981; Martin and Kieffer, 1979). Often these large–scale waves exist where the latitudinal shear of the zonal wind is large, and this suggests that barotropic instability may be an important process in these regions.

For Venus, Elson (1982) used the linearized barotropic nondivergent vorticity equation to find the fastest growing, barotropically unstable wave mode. This mode had zonal wavenumber 2 and a period of about 3 terrestrial days, both characteristic of the high–latitude thermal wave observed in the upper cloud region of Venus by the Pioneer Venus Orbiter Infrared Radiometer (OIR). In a similar manner, Hartmann (1983) found that barotropic instability in the terrestrial stratosphere could produce a wave of the "4–day" variety detected by Venne and Stanford (1979). Using a quasi–geostrophic model on a sphere, Hartmann (1983) also investigated the effects of divergence and of vertical shear of the basic state zonal wind on the barotropically unstable modes. The period, relative *e*–folding time and zonal wavenumber of the most unstable mode were relatively unchanged by the inclusion of the velocity divergence and vertical shear in the model. The most important effects of the vertical variation of the zonal jet were that the absolute *e*–folding time of the fastest growing, wavenumber 1 wave increased by nearly 50%, and polar modes having larger longitudinal wavenumbers were no longer found to be unstable. Pfister (1979) had previously found, using a $\beta$–plane model, that the growth rates computed for essentially barotropic modes were markedly reduced when realistic vertical shear was included. For Mars, Conrath (1981) argued that the wave–like perturbations

found in the Mariner 9 temperature data for high latitudes during winter were more likely to be produced by vertical propagation of nearly stationary waves rather than by *in situ* instabilities, since the phase speeds of locally produced disturbances would be much faster than indicated by the observations. However, Conrath also noted that the thermal wind profile was probably barotropically unstable and that the observational coverage provided by Mariner 9 was subject to aliasing. Thus, barotropic instability was still a candidate mechanism.

In the work reported here, a linearized barotropic nondivergent vorticity model is used to find the fastest growing, barotropically unstable mode for zonal wind profiles which may be representative of the Martian high latitudes during winter. Our numerical method finds only the fastest growing mode for a given zonal wavenumber. These modes are the most likely to be observed, and Hartmann's (1983) analyses indicated that their computed period and spatial variations provide a reasonable first approximation to the streamfunction fields of their quasi–divergent counterparts. This is critical to our use of the nondivergent vorticity equation, since it is the quasi–divergent modes which can give rise to the patterns of thermal emission observed remotely by satellites. The same analytic form for the high–latitude jet is used here as in Hartmann. This facilitates comparison with his work, while also providing a reasonably good fit to the thermal winds constructed for Mars from the Mariner 9 Infrared Interferometer Spectrometer (IRIS) temperature profiles and for Venus from the Pioneer Venus OIR data.

The high–latitude zonal jet on Venus and the polar–night jets in the atmospheres of Earth and Mars all appear to be of comparable angular width and position. If the effective width and location of the jet are fixed, the linearized, nondivergent vorticity equation has one free parameter, the Rossby parameter $Ro \equiv U/\Omega a$, with $U$ a characteristic velocity of the zonal jet, the planetary radius $a$, and the sidereal

frequency $\Omega$ of the planet's solid body rotation or, in the case of Venus, of the solid body component of its atmospheric motion. Because Mars is a smaller planet and because both the atmosphere and the surface of Venus rotate relatively slowly, the high–latitude zonal jets on Mars and Venus are characterized by larger $Ro$ than on Earth. Thus, our results for Mars are complementary to Hartmann's (1983) parametric studies for Earth's stratosphere and can be presented in the context of that larger parameter space. Hartmann's results showed that the growth rate of a barotropically unstable mode with zonal wavenumber $k = 2$ became comparable to the fastest growing $k = 1$ mode for the strongest jets. Our calculations show that the $k = 2$ mode does not become the fastest growing barotropic wave until the $Ro$ of these relatively broad jets is increased to values characteristic of Mars ($Ro \sim 0.4$). Both the $k = 1$ and $k = 2$ modes have their maximum amplitude poleward of the zonal wind maximum for this $Ro$ range. However, at the somewhat larger $Ro$ which may be characteristic of the strongest jets on Mars or Venus, the fastest growing barotropic mode is a $k = 2$ mode whose maximum amplitude is now on the equatorward flank of the jet. Hartmann had previously found mid–latitude modes associated with the region of negative absolute vorticity on the equatorward flank of the high–latitude zonal jets, but these were never the fastest growing barotropic modes for the terrestrial stratosphere. This general variation with increasing $Ro$ for fixed position and width of the jet is discussed in Section 4.

First, however, we briefly describe, in Section 2, the barotropic nondivergent vorticity model used to characterize the fastest growing modes. Then in Section 3 we select a range of zonal jet parameters — primarily $Ro$ and the jet width — appropriate to Venus and to Mars. Section 4 follows with a unified presentation (in terms of the $Ro$ parameter) of our results with those of Elson (1982) and Hartmann (1983) for nondivergent, barotropically unstable modes of relatively broad,

mid–latitude zonal jets in planetary atmospheres. Section 5 presents some specific examples appropriate to Venus and Mars.

## 3.2 Barotropic Model

Following Hartmann (1983), we represent the zonal–mean zonal wind $\overline{u}$ by this simple analytic form:

$$\overline{u} = U_o \eta(\theta) \cos\theta \quad , \qquad \eta \equiv sech\left[\frac{2}{B}(\theta - \theta_o)\right] \tag{3.1}$$

with latitude $\theta$ and constant jet parameters $U_o$, $\theta_o$, $B$. Given the planetary radius a, $U_o a^{-1}$ is the maximum angular velocity of the zonal jet, $\theta_o$ is the latitude of that maximum, and $B$ is the width of the jet. The zonal velocity maximum is also near $\theta_o$ and its value is roughly $U_o \cos\theta_o$. For time $t$ and east longitude $\lambda$, the perturbation streamfunction $\psi'$ is assumed to have the form:

$$\psi' = \psi(\theta) \exp\left[ik(\lambda - \sigma t)\right] \tag{3.2}$$

with zonal wavenumber $k$, streamfunction $\psi$, and $\sigma = \sigma_r + i\sigma_i$ the complex frequency of the disturbance. Given (2) and the analytic form (1), the linearized barotropic nondivergent vorticity equation can be written in the following nondimensional form:

$$\left(Ro\eta - \frac{\hat{\sigma}}{2}\right)\left\{\frac{d^2}{d\theta^2} - \tan\theta\frac{d}{d\theta} - \frac{k^2}{\cos^2\theta}\right\}[\psi] + \frac{\alpha\psi}{\cos\theta} = 0 \tag{3.3}$$

with the nondimensional absolute vorticity gradient

$$\alpha = \left\{1 - Ro\left(\frac{d^2\eta}{d\theta^2} - 3\tan\theta\frac{d\eta}{d\theta} - 2\eta\right)\right\}\cos\theta \quad . \tag{3.4}$$

Solutions to (3) for fixed $\theta_o$ and $B$ depend only upon the nondimensional Rossby number $Ro \equiv (U_o/2\Omega a)$, as long as the period and $e$–folding times are expressed in terms of $\Delta$, the length of the sidereal day; i.e., $\hat{\sigma}$ is $\sigma$ normalized by the planetary rotation rate $\Omega \equiv 2\pi/\Delta$. (This choice of $Ro$ implies a velocity scale $U = U_o/2 \sim U_o \cos\theta_o$.) For Earth and Mars, the $\Omega$'s are nearly identical. For Venus $\Omega$ is taken to

be 1/4 that of Mars; this assumes that the solid body component of the atmospheric rotation is given by the Venusian "4–day" wind. Specific planetary parameters will lead to different solutions of (1) only if they combine to yield different Rossby parameters. Table 1 lists the different values for Venus, Earth, and Mars of the zonal wind velocity Uo which yield the same Rossby parameter, given the planetary parameters in Table 2.

For this simple model, the zonal–mean zonal wind equation is given by

$$\frac{\partial \overline{u}}{\partial t} = -\frac{1}{a\cos^2\theta}\frac{\partial}{\partial\theta}\left[\overline{u'v'}\cos^2\theta\right] \equiv A_u \tag{3.5}$$

where the overbar denotes a zonal (i.e., longitudinal) average and $u'$, $v'$ are the longitudinal perturbation eastward and northward wind components. $A_u$, the zonal-mean zonal acceleration induced by the barotropic perturbation, is related to the Eliassen–Palm (EP) flux–divergence $\nabla \cdot F$ by $(a\cos\theta)A_u = \nabla \cdot F$, which is also the convergence of the poleward flux of angular momentum. The enstrophy budget consistent with (3) also involves $A_u$ (Hartmann, 1983):

$$\frac{\partial}{\partial t}\left[\frac{1}{2}\overline{\varsigma'\varsigma'}\right] = -A_u\left(\frac{2\Omega\alpha}{a}\right) \quad , \tag{3.6}$$

with the perturbation relative vorticity $\varsigma' = \nabla^2\psi'$. Thus, the barotropic perturbations will grow if the acceleration $A_u$ (or equivalently, the EP flux–divergence) has the opposite sign as the meridional gradient of zonal–mean absolute vorticity. As in Hartmann, the unstable perturbations found here are growing at essentially all latitudes. A necessary and often sufficient condition for barotropic instability to occur is that the absolute vorticity gradient $\alpha$ vanish somewhere in the latitudinal domain of interest (Kuo, 1949). For large values of the Rossby parameter $Ro$ (and thus $U_o$ for a given planet), the absolute vorticity gradient derived from (1) may vanish on the equatorward side of the zonal jet, as well as on the poleward flank.

The barotropically unstable modes discussed in this paper were computed using the numerical model of Elson (1978). This model integrates the linearized nondivergent barotropic vorticity equation (3) forward in time for a given value of the zonal wavenumber $k$ and for the absolute vorticity gradient (4) and with $\eta$ given by (1). Eventually, the time–integrated streamfunction field is dominated by the fastest growing mode. The time integration is stopped when the time variation at all latitude points yields essentially the same complex frequency. Here, the perturbations are assumed to be symmetric about the equator and 91 latitudinal gridpoints were used to span the northern hemisphere. In this way, the fastest growing, barotropically unstable mode was found, given the zonal wavenumber $k$ and the zonal jet parameters $Ro$, $\theta_o$, and $B$.

TABLE 1

$U_o$ (m s$^{-1}$) for Mars, Earth and Venus Corresponding to Various $Ro = U_o/2\Omega a$
Values.

| $Ro$ | 0.10 | 0.13 | 0.20 | 0.26 | 0.41 | 0.5 | 0.58 | 0.62 |
|------|------|------|------|------|------|------|------|------|
| Mars | 48 | 64 | 96 | 124 | 200 | 240 | 280 | 300 |
| Earth | 93 | 124 | 186 | 240 | 387 | 464 | 541 | 580 |
| Venus | 21 | 28 | 43 | 56 | 89 | 107 | 125 | 134 |

TABLE 2

Planetary Parameters.

| | Venus | Earth | Mars |
|------|------|------|------|
| $a$ ( km) | 6052 | 6378 | 3394 |
| $\Omega$ (s$^{-1}$) | $1.772 \times 10^{-5}$* | $7.292 \times 10^{-5}$ | $7.088 \times 10^{-5}$ |
| $a\Omega$(m s$^{-1}$) | 107 | 465 | 241 |

* Venus rotation frequency is assumed here to be that of the atmospheric solid body
component near the cloud tops ($\sim$ 65 km); i.e., the "4–day" wind.

## 3.3 Zonal Jets: Choice of Parameters

### 3.3.1 Venus

Here the zonal–mean zonal wind in the middle atmosphere of Venus is modeled as just the superposition of a mid–latitude zonal jet upon a solid–body component of atmospheric rotation. The planetary rotation rate $\Omega_V = 2\pi\Delta_V^{-1}$ is assumed to be given by the period $\Delta_V$ of the solid body component, which is observed to vary significantly with height. $\Delta_V$ decreases with height, reaching a minimum of 4 days or so at 65 km, near the cloud tops. Winds above this level are inferred from the observed temperature field by assuming cyclostrophic balance and so are somewhat uncertain. It does appear, however, that $\Delta_V$ increases by roughly a factor of 2 by 75 km, and that there is a high–latitude jet which peaks near $\theta = 60°$ and in the 65–70 km region, where the amplitude (i.e., $U_o \cos\theta_o$) of the zonal jet relative to the solid body component may range from 50 to 110 m s$^{-1}$ (Elson, 1982; Newman et al., 1984; Taylor et al., 1985). These combinations of $\Delta_V$ and $U_o$ correspond to $Ro \geq 0.5$, with $Ro \simeq 0.5$ characteristic of the height where planetary–scale waves are observed at high–latitudes (Taylor et al., 1980; Elson, 1982). The angular width of the zonal jet is approximately 20°.

### 3.3.2 Mars

Conrath (1981) analyzed the atmospheric temperature profiles retrieved from the Mariner 9 IRIS measurements of the spectral radiance within the $CO_2$ 15 $\mu$m absorption band. The observations were taken during January and early February 1972, a period of approximately 40 days spanning late northern winter on Mars

($L_s = 330-350°$, where $L_s$ is the areocentric longitude of the sun measured from its position at the beginning of northern spring). Temperatures were retrieved at five pressure levels (0.117, 0.300, 0.518, 1.13, and 2.46 mb) and were grouped into 10° latitude intervals. When averaged over this entire period, the Mariner 9 data yield the late northern winter meridional plane cross–section of temperature shown in Fig. 1. The very cold temperatures at polar latitudes are produced primarily by a balance between heat lost by radiation to space and latent heat released by the condensation of $CO_2$, the Martian atmosphere's primary constituent. The lower mid–latitudes are becoming warmer as Mars moves toward its vernal equinox, and the thermal contrast across high mid–latitudes is particularly strong at this season. Mars rotates nearly as rapidly as does Earth, so that the winds at extratropical latitudes should be nearly in thermal wind balance. Figure 1 also shows the zonally averaged eastward winds that we have constructed from the zonally averaged temperature field derived by Conrath (1981). The gradient wind balance was used and the winds were assumed to vanish close to the Martian surface. Reasonably good fits to the gradient winds above 0.5 mb ($\sim$ 20 km) are given by (1) with $U_o$ in the range 200–240 m s$^{-1}$ and with $B = 20°$, $\theta_o = 60°$. Somewhat better fits are given by slightly wider jets ($B = 25°$, with $U_o = 180-210$ m s$^{-1}$), but the averaging of retrieved temperatures within 10° latitudinal bins may have artificially broadened the zonal jet. These values of $U_o$ combined with the Martian rotation rate and radius yield Rossby parameters in the range 0.35–0.5; these values are significantly larger than those examined by Hartmann (1983). His largest $U_o$ value (240 m s$^{-1}$) for Earth yields $Ro = 0.26$, which corresponds to $U_o = 124$ m s$^{-1}$ for Mars (see Table 1). It was therefore necessary to solve (3) for the larger $Ro$ values appropriate to Mars.

Figure 1. Observed mean meridional temperature $\overline{T}$ (K) (top) and computed mean zonal gradient wind $\overline{u}$ (m s$^{-1}$) (bottom) for northern winter on Mars. The temperature profiles used in constructing this cross section were taken from Conrath (1981), who analyzed the spectral radiances measured by the Mariner 9 Infrared Interferometer Spectrometer (IRIS). The zonal gradient winds were calculated assuming that the wind vanished at the 5 mb level, near the surface.
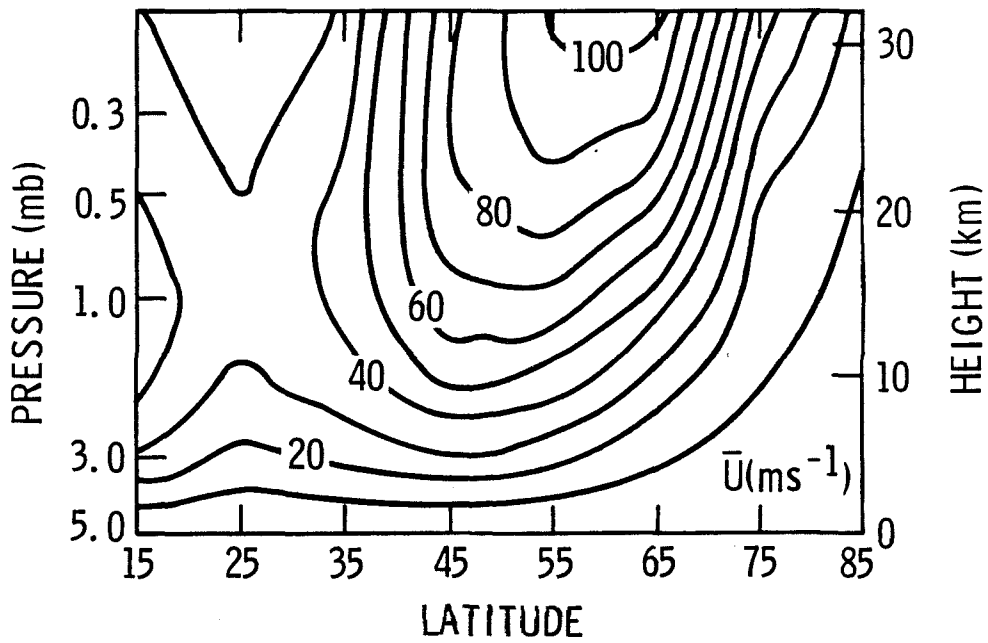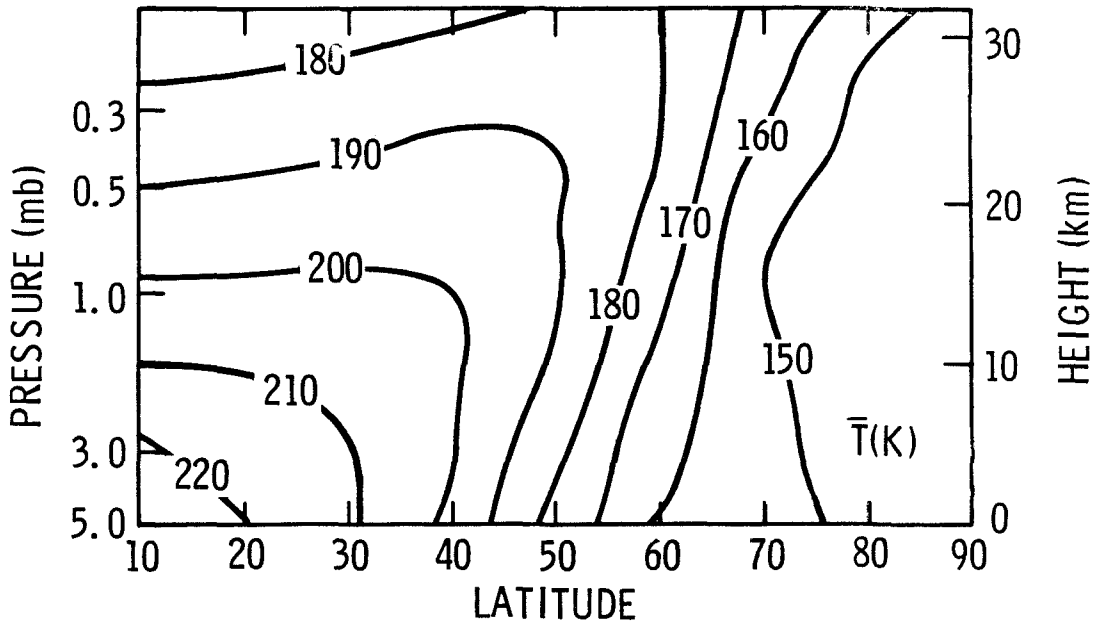
Figure 1

## 3.4 Barotropic Instability: General Results

As noted earlier, the computed periods and $e$–folding times of the solution to the linearized, nondivergent barotropic vorticity equation depend only on $Ro = U_o/2\Omega a$ for a given zonal wavenumber and for a fixed angular variation and position of the zonal jet, as long as the time scales are expressed in terms of the sidereal day $\Delta = 2\pi/\Omega$. Thus, we define the wave period $\tau_r \equiv 2\pi(k\sigma_r\Delta)^{-1}$ and the wave $e$–folding time $\tau_i \equiv (k\sigma_i\Delta)^{-1}$. This permits a unified presentation of Elson's (1982) results for Venus, Hartmann's (1983) results for Earth, and our results for Mars, with regard to the barotropic instability of high–latitude zonal jets. Figures 2 and 3 show the dependence on $Ro$ of $\tau_r$ and $\tau_i$ for a given zonal wavenumber $k$. The points indicated by the letter $E$ are taken directly from Hartmann's (1983) tables and are representative of barotropic instability for the terrestrial polar night jet. As a test, the growth times and periods of the fastest growing waves for $Ro \sim 0.20$ and $0.26$ ($U_o = 180$ and $240$ m s$^{-1}$) and with $k = 1, 2$ were exactly reproduced by our model. All cases shown in Figures 2 and 3 used the zonal wind profile given by (1) with $\theta_o = 60°$ and $B = 20°$, except for the point for Venus indicated by the letter $V$. This was taken from Elson's (1982) Table 2 (the "low–latitude" model with $\theta_o = 62°$ and $k = 2$) and normalized by a sidereal day $\Delta_V = 4\,\Delta_M$ (i.e., a 4–day wind). The results labeled $V'$ in Figures 2 and 3 were computed using (1) with $U_o = 100$ m s$^{-1}$, as suggested by Elson's representation of the mean zonal wind near the Venus cloud tops. The agreement between the points $V$ and $V'$ is very good, considering the somewhat different latitudinal shapes assumed for the cyclostrophic Venus jet by Elson and by us. The value indicated by $V''$ in Figure 2 is for a case having the same parameters as for case $V'$, except that $Ro$ is slightly

Figure 2. Periods $\tau_r$ as a function of $Ro$ for various zonal wavenumbers. The periods have been normalized by $\Delta$, the length of the sidereal day. The letter $E$ indicates values from Hartmann (1983). The letters $V'$, $V''$ indicate Venus values derived for slightly different $Ro$ values and the dashed line connecting them delineates a discontinuous transition for the $k = 2$ curve. The letter $V$ denotes a Venus case derived from Elson's (1982) tabulated results.

Figure 3. Same as Figure 2, except for the $e$–folding times $\tau_i$, also normalized by $\Delta$. The dashed line through the value indicated by $V'$ denotes a hypothetical solution in which the physical growth time $\tau_i \Delta_V$ would remain constant for Venus as $\Delta_V$, but not $U_o$, changes. The horizontal arrows depict typical ranges of $Ro$ for Earth, Mars, and Venus.
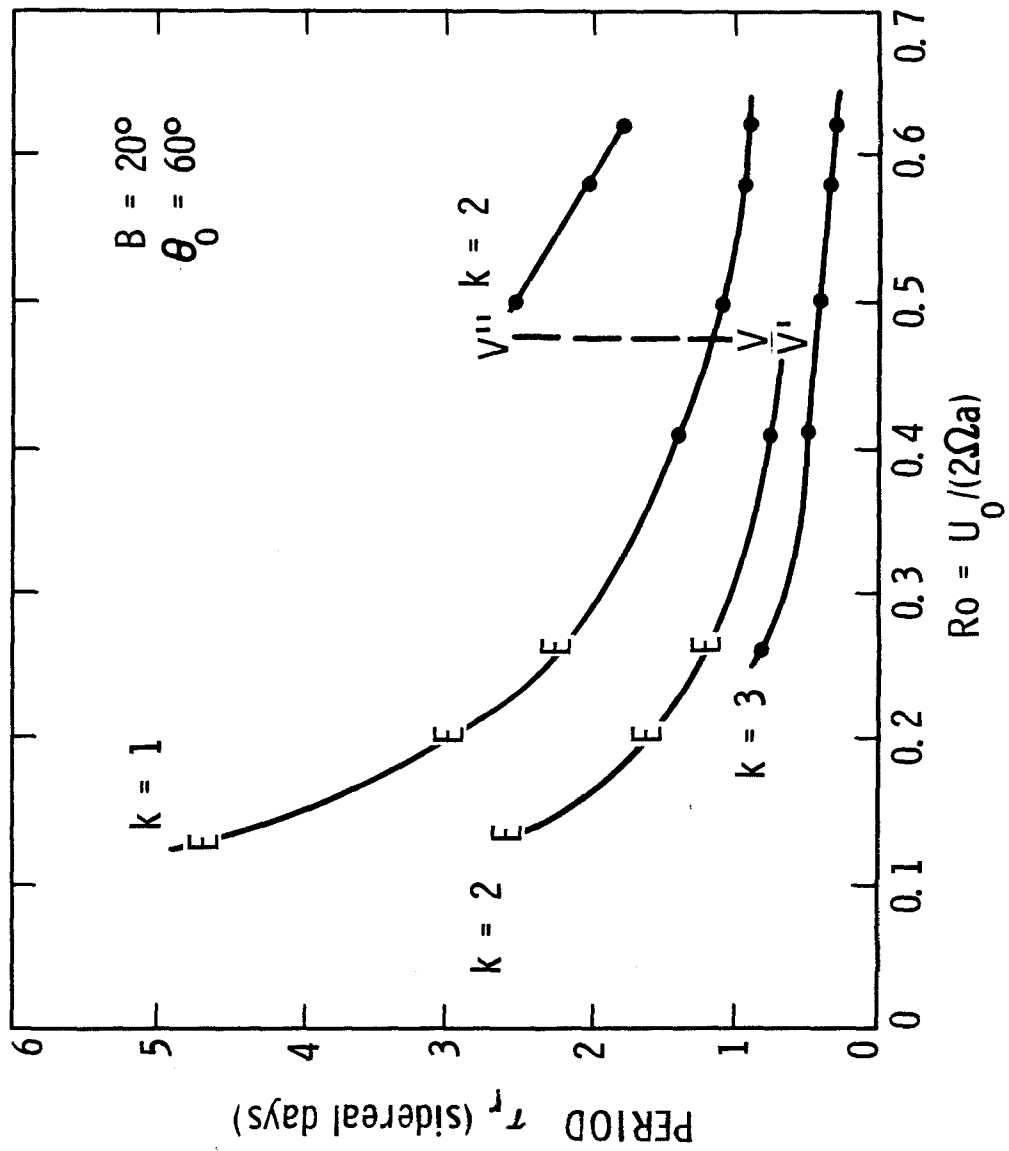
Figure 2
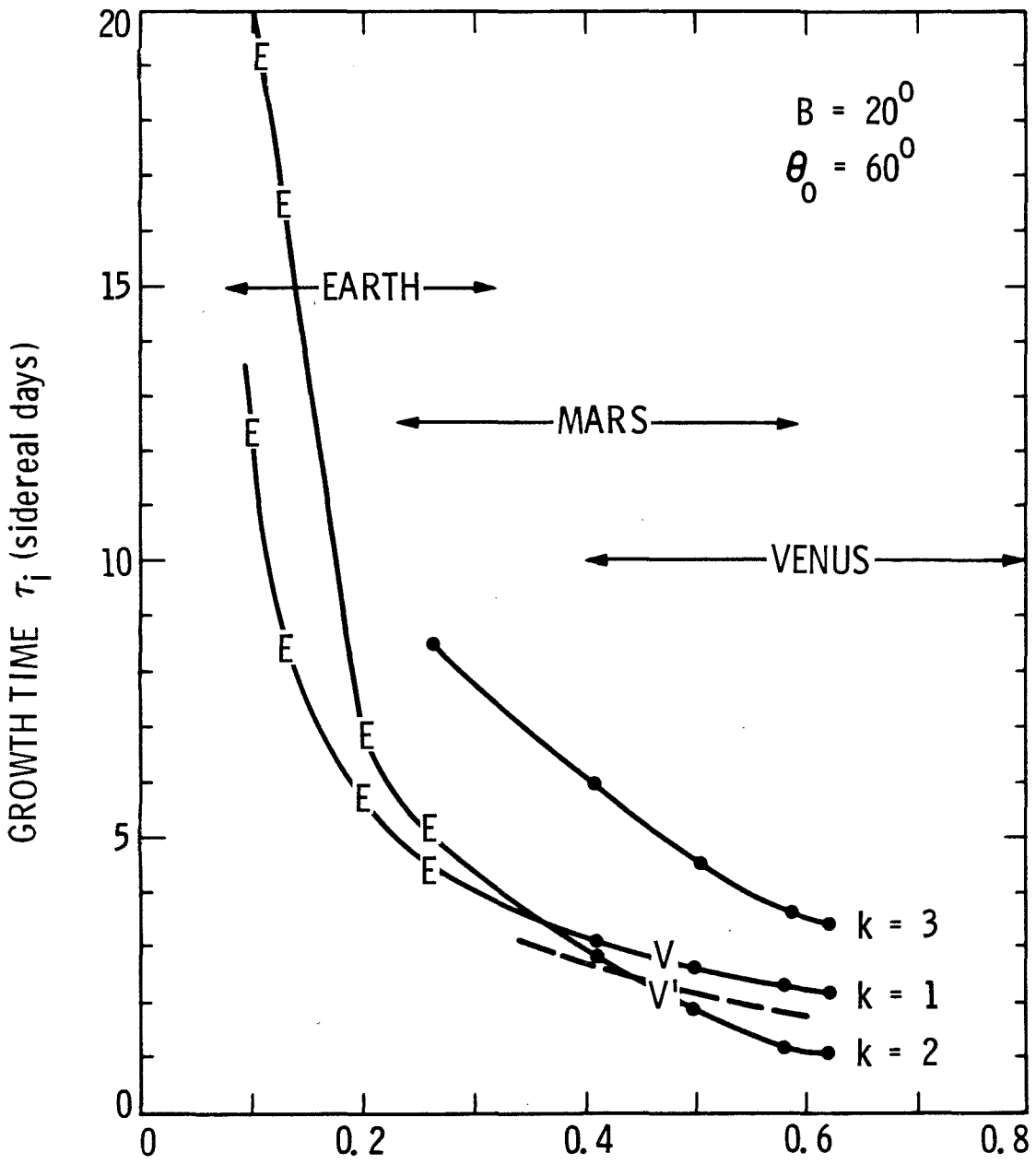
Figure 3

larger. The discontinuous change in the wave period signifies a transition in which
barotropically unstable modes on the equatorward flank of the jet grow more rapidly
than those on the poleward flank, for zonal wavenumber $k = 2$. This transition
occurs at larger $Ro$ for wider jets and, in fact, has moved between $Ro = 0.62$ and
$0.65$ for $B = 25°$ (Fig. 4).

The sensitivity of the period and growth rate of the unstable waves to the
width of the jet can be seen in Figures 4 and 5. From Figures 3 and 5 it is clear
that the fastest growing wave is of wavenumber 1 or 2, with the latter favored for
narrower jets and for larger $Ro$. The $e$–folding times $\tau_i$ become quite short for
large $Ro$, ranging from 1 to 3 days. The wave period $\tau_r$ decreases for larger zonal
wavenumbers or as $Ro$ increases, except for $k = 2$ and $B < 25°$, where $\tau_r$ increases
discontinuously by a factor of 4 or more. These longer period modes are members of
the same family of mid–latitude modes studied by Hartmann (1983), except that for
$Ro \gtrsim 0.45$ and for jets which are not too broad, these mid–latitude modes become
the fastest growing barotropic instabilities. Thus, for $B = 20°$ and $\theta = 60°$, the
fastest growing mode shifts as $Ro$ increases from a polar $k = 1$ wave to a shorter
period $k = 2$ polar mode and then to a longer period, $k = 2$ mid–latitude mode. For
a sufficiently broad jet $(B = 25°)$, the polar $k = 1$ and $k = 2$ modes may continue
to dominate as $Ro$ increases (Figs. 4 and 5). The position of the jet $(\theta_o)$ was also
varied, and the results are listed in Table 3. The sensitivity of $\tau_i$ to $\theta_o$ is comparable
to that for $B$, the jet width, while $\tau_r$ is more sensitive to $\theta_o$. Again, this is because
of a shift from a poleward to an equatorward mode as the jet maximum is moved
to a lower latitude. In this sense, a shift to lower latitude has the same effect as
narrowing the jet. The contrast between the poleward modes and the longer period,
mid–latitude modes is clearly evident in Figures 6, 7, and 8 where the perturbation

Figure 4.   Normalized periods $\tau_r$ for Mars as a function of zonal wavenumber, showing the effects of varying the width of the zonal jet.

Figure 5. Normalized growth times $\tau_i$ for the same cases as in Fig. 4.
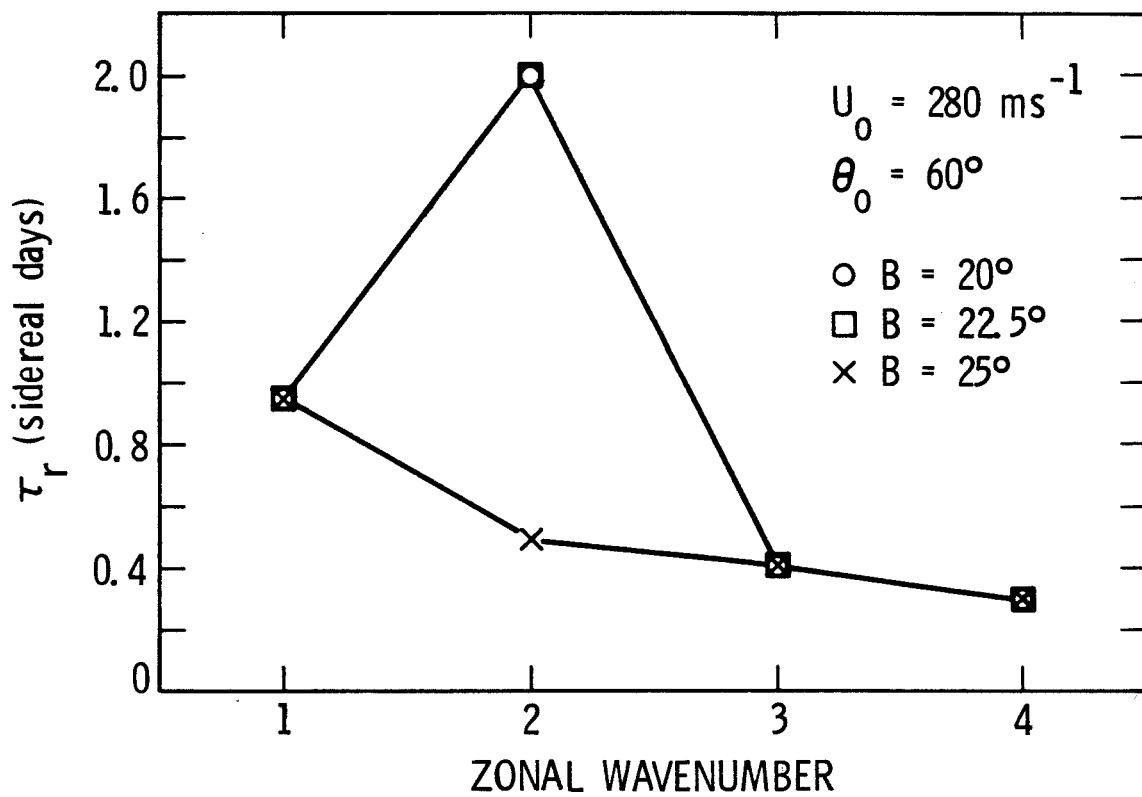
Figure 4
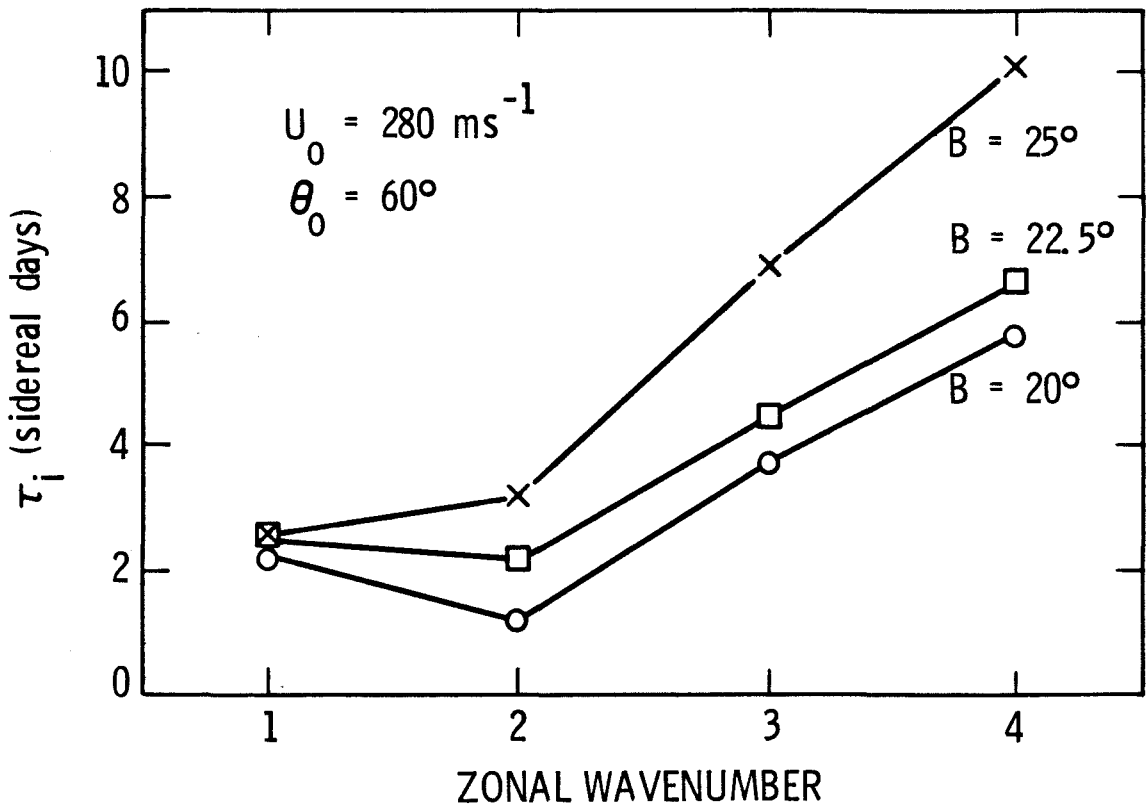
Figure 5

## TABLE 3

The $e$-folding times $(\tau_i)$ and periods $(\tau_r)$, given in sidereal days, for the fastest growing barotropic wave for various positions $(\theta_o)$ of the jet maximum and for $Ro = 0.58$, $B = 22.5°$, $k = 2$. The latitude $\theta_*$ of the maximum in streamfunction amplitude is also given.

| $\theta_o$ | $\tau_i$ | $\tau_r$ | $\theta_*$ |
|:---:|:---:|:---:|:---:|
| 45° | 1.1 | 1.3 | 42° |
| 60° | 2.2 | 2.0 | 54° |
| 70° | 6.4 | 0.5 | 78° |

streamfunction amplitude structure and the wave–induced acceleration $A_u$, together with the basic state $\overline{u}$ and $\alpha$, are shown, all scaled to arbitrary amplitudes. For both the poleward and equatorward modes, the wave induced zonal forcing per unit mass is such that the zonal jet is being deaccelerated near its maximum and accelerated on the poleward and equatorward flanks, respectively.

Figure 6. Structure of the most unstable barotropic mode for $\overline{u}$ given by Eq. (1) with $\theta_o = 60°$, $B = 20°$ and $Ro = 0.46$. For this mode $k = 2$, $\tau_r = 0.7$ days and $\tau_i = 2.5$ days. The zonal mean wind $\overline{u}$, basic state vorticity gradient $\alpha$, perturbation streamfunction amplitude $|\psi|$ and wave–induced acceleration $A_u$ are given in arbitrary units.

Figure 7. Same as Figure 6, except $Ro = 0.50$. $\tau_r = 2.5$ days and $\tau_i = 2.0$ days. Note the equatorward shift of $\psi$ and of the wave–induced acceleration $A_u$.

Figure 8. Same as Figure 6, except for $B = 25°$. For this mode $k = 1$, and $\tau_r = 1.2$ days and $\tau_i = 3.2$ days. The phase of the streamfunction is also shown.

Figure 6

LATITUDE (degrees)

Figure 7

$R_0 = 0.50$
$B = 20^0$
$\theta_0 = 60^0$
$k = 2$
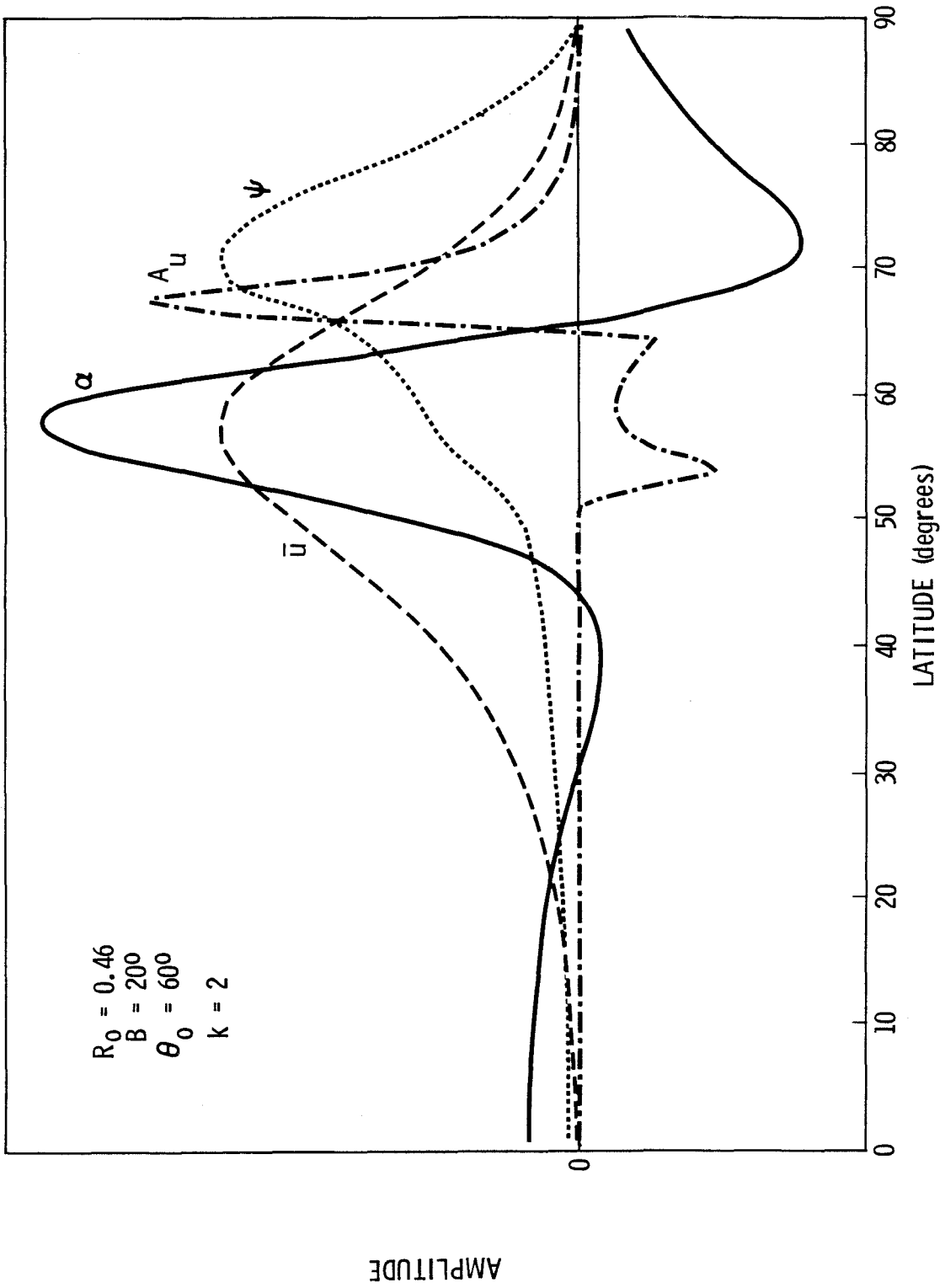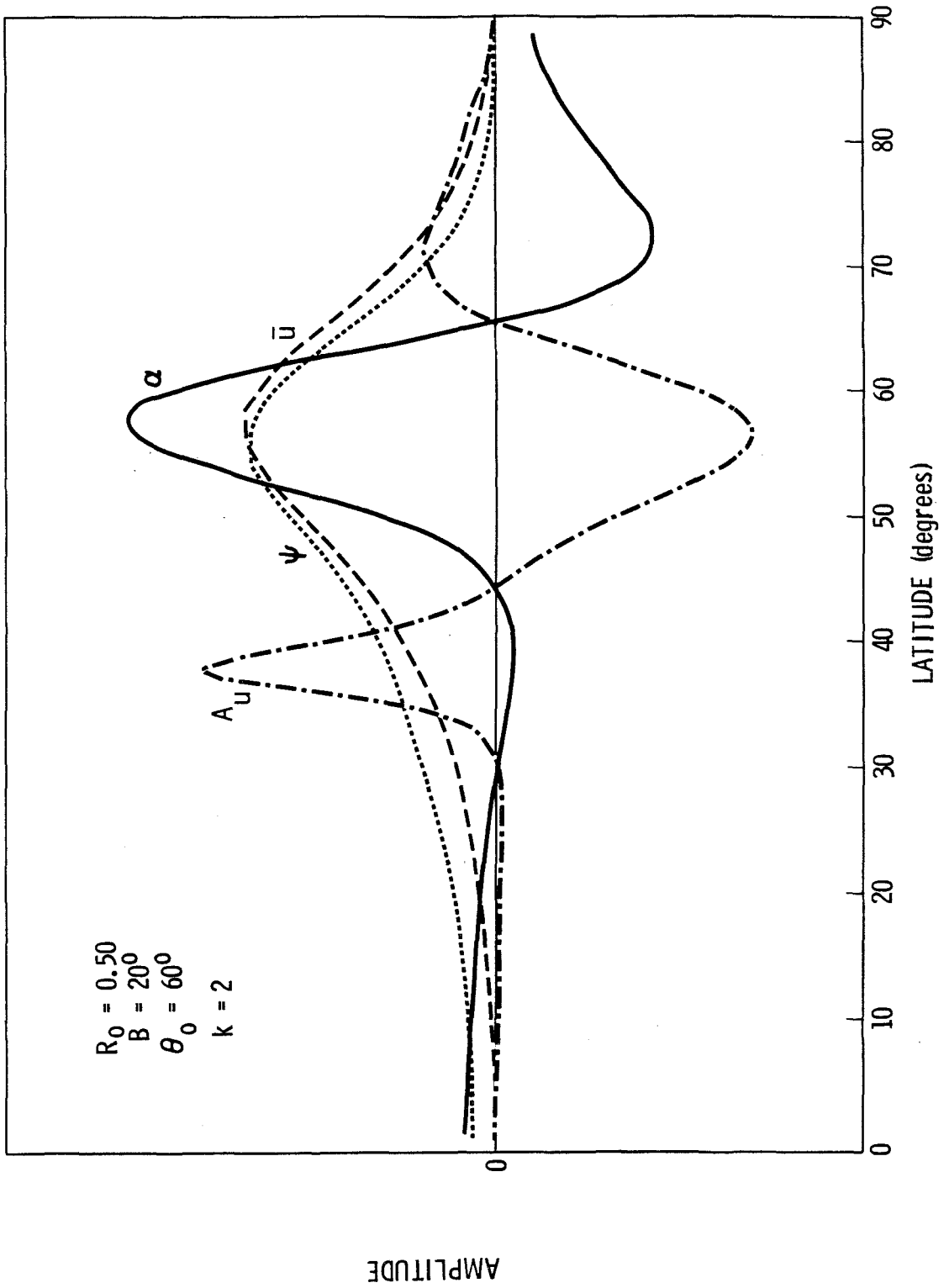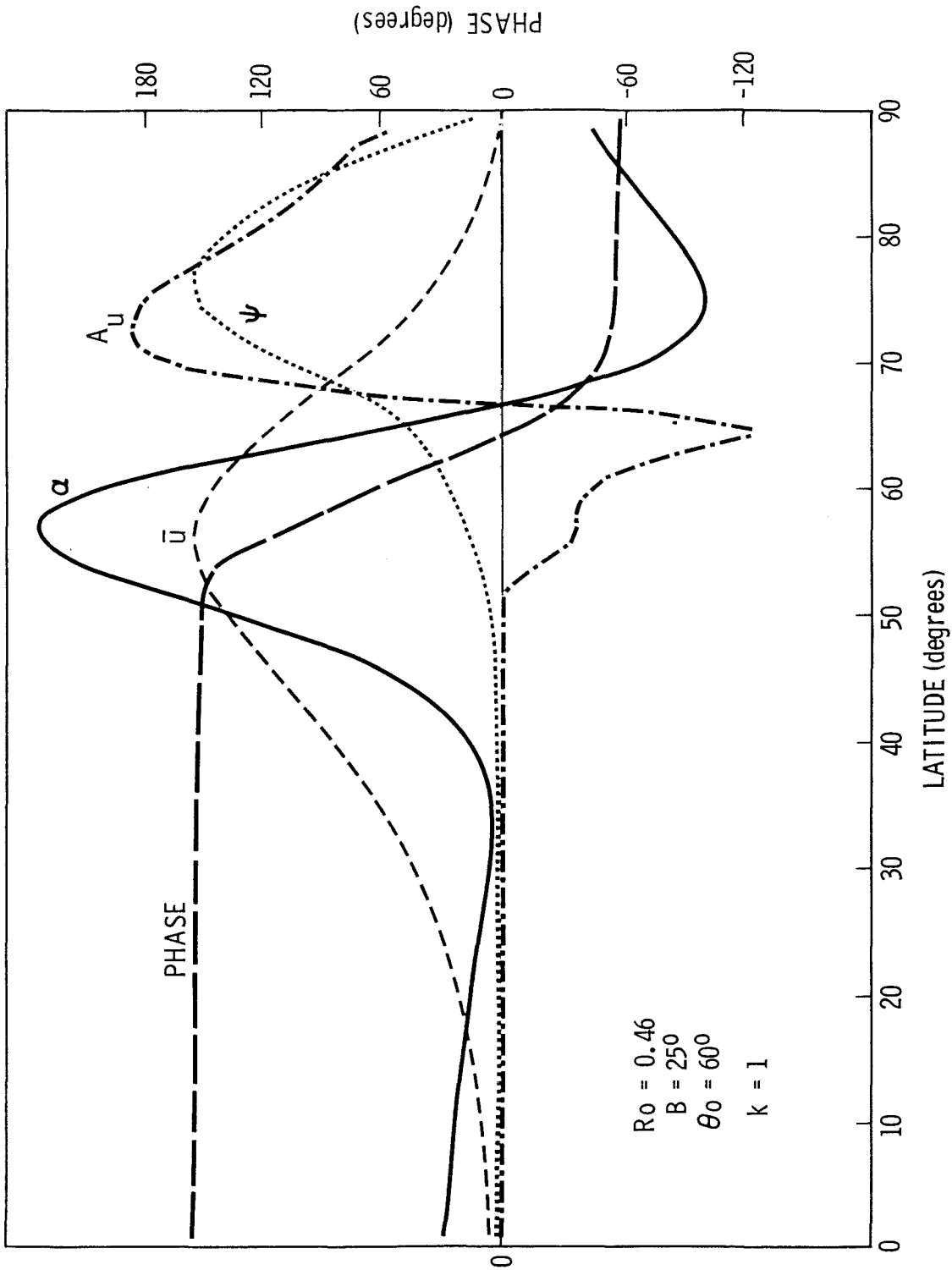
AMPLITUDE

Figure 8

## 3.5    Barotropic Instability: Specific Results

### 3.5.1    Venus

In Figure 6, the perturbation streamfunction $\chi$ has its maximum amplitude near 70°, poleward of the jet maximum. This mode is similar to the fastest growing wave computed by Elson (1982) for Venus and to the poleward modes found by Hartmann (compare Fig. 6, for instance, with his Fig. 5). Venus appears perilously close to the transition between poleward and equatorward modes (Figs. 6 and 7). Since the jet is unlikely to remain constant in time or with latitude, the "dipole" thermal feature on Venus may change substantially with time. For situations characterized by higher $Ro$, the barotropic "dipole" should move equatorward to the vicinity of the zonal jet and have a much longer period ($\sim$ 10 Earth days). For sufficiently lower $Ro$, the dipole should transform into a $k = 1$ pattern, still at high latitude, but again with a long period ($\sim$ 6 Earth days).

The normalization of the growth times and periods by $\Delta$ may be misleading for slowly rotating planets like Venus where $\Delta_V$ is the solid–body component of an atmospheric rotation which varies with height. If the characteristic angular velocity of the jet decreases as rapidly with height as the Venus atmosphere's solid–body rotation, then the middle atmosphere will have constant $Ro$, $\tau_i$, and $\tau_r$, while the actual growth times ($\tau_i\Delta$) and periods ($\tau_r\Delta$) will increase with $\Delta$ and thus with height. In this case, the fastest growing barotropic waves would be near the cloud–top region where the thermal polar "dipole" was observed (Taylor $et~al.$, 1980). The dashed curve through the point labeled $V'$ in Figure 3 shows a hypothetical solution for $\tau_i$ in which $\tau_i\Delta$ remains constant for $k = 2$ even as the atmospheric rotational

period $\Delta$, but not the relative angular velocity of the zonal jet, changes. Since the slope of the $k = 2$ curve is steeper than that of this hypothetical solution near the current Venus solution, the dimensional, as well as the nondimensional, growth time will decrease with height, for this case of nearly constant $U_o$. This suggests that barotropically unstable modes could grow faster near 75 km than at the visible cloud tops near 65 km, but ignores possible effects of the vertical shear itself. If the barotropic zonal jet remains relatively narrow, the mode at 75 km should have its maximum amplitude on the equatorward side of the jet and its actual period in the range 8–10 Earth days. The thermal structure of an unstable wave having these characteristics was not detected in the 72–day Pioneer Venus OIR data record (Apt and Leung, 1982). Above 75 km on Venus, the rotational period $\Delta_V$ may become very large (Elson, 1978; Newman $et$ $al.$, 1984). Eventually, the jet too decays with height and the actual growth times will begin to increase. Thus, barotropically unstable waves seem less likely to be present in the upper regions of the Venus middle atmosphere.

### 3.5.2    Mars

The gradient wind shown in Figure 1 has considerable vertical structure. In order to check whether or not the atmosphere away from the surface was itself baroclinically unstable, the contribution of the vertical shear and curvature terms to changing the sign of the meridional gradient of quasi–geostrophic potential vorticity was computed for the fields shown in Figure 1. Except near the surface, this contribution was small compared to that of the meridional gradient of absolute vorticity. Of course, the presence of a latitudinal gradient of potential temperature at the surface can still produce baroclinically unstable waves (Charney and Stern,

1962; Barnes, 1984). Barnes (1980, 1981) found strong evidence in the Viking Lander 2 surface wind, temperature, and pressure data, for eastward–traveling quasi–geostrophic waves of zonal wavenumbers between 2 and 4 at $48°N$  The corresponding periods were between 8 and 2 Martian days (sols). These observed values are inconsistent with the barotropic wave parameters computed here, but that does not preclude the presence of waves at higher altitudes which are largely barotropic in nature. Pfister (1979) showed that the vertical shear of $\bar{u}$ will tend to confine barotropic modes near the levels of strongest horizontal shear. For Mars and the winds shown in Figure 1, this means that the barotropically unstable modes should have little amplitude at the surface.

Conrath's (1981) wave–analysis of the Mariner 9 temperature data implied long periods of 10 days or more for low wavenumbers, consistent with the analyses by Barnes (1980, 1984) of the Viking Lander meteorological data. However, the Mariner 9 data were restricted by the spacecraft orbit and limitations in data transmission to sampling in time just once per day. As pointed out clearly by Conrath, this infrequent sampling could have led to serious aliasing of the data, so that there were many well defined, but disjoint frequencies which were consistent with the observations for a given zonal wavenumber.

For wavenumbers 1 and 2, which are barotropically the fastest growing waves for the Mars mid–latitude jet, the first–order alias of Conrath's analysis yields eastward traveling waves with periods of 1.24 to 1.105 days for $k = 1$ and 1.20 or 1.07 days for $k = 2$. In Figure 2, these periods correspond to an $Ro$ of 0.46 or 0.5 for $k = 1$ and to 0.26 or 0.29 for $k = 2$. For the zonal jet shown in Figure 1 these two $Ro$ ranges occur above the 0.3 and near the 1.0 mb levels, respectively. Conrath (1981) found that the largest temperature wave observed by Mariner 9

had its maximum amplitude in the region between 1.5 and 0.6 mb, where the $k = 2$ mode has the correct period. However, in this $Ro$ range (0.26–0.31), the $k = 1$ mode should grow somewhat faster than the $k = 2$ wave (see Fig. 3). In fact, the structure of the primary temperature wave identified by Conrath is characteristic below 0.5 mb of a vertically propagating wave, perhaps generated by baroclinic instability at the surface. Both Conrath's calculation of the index of refraction for a vertically propagating wave and the linear baroclinic instability study by Barnes (1984) indicate that such a wave would have little temperature amplitude at 0.5 mb and, indeed the observed phase of the wave ceases to tilt westward with height near this level. However, the observations suggest that there is still sizeable amplitude above this level where the fastest growing barotropically unstable wave is a $k = 1$ mode with the proper period. Such a mode is shown in Figure 8.

Hartmann's (1983) results indicate that the latitude of maximum temperature amplitude for the quasi–geostrophic barotropic modes for Earth will be close to that of the maximum streamfunction amplitude for the nondivergent modes. If so, the poleward mode shown in Figure 8 could not account for the temperature variation found by Conrath for the 40°–70° latitudinal zone. Mid–latitude (i.e., $k = 2$) modes have their maximum at the right latitudes (Fig. 7), and would be the fastest growing barotropic modes for a narrower zonal jet (Fig. 3). However, their periods are too long. Faster growing mid–latitude barotropic modes may also occur above the 0.1 mb level if the wind continues to increase with height. The thermal signature of these modes may depend critically on the radiative damping time, which should decrease rapidly with height in this region. Our results do suggest that the character of the fastest growing barotropic mode in the middle Martian atmosphere may change significantly (e.g., the maximum amplitude may

shift from the poleward to the equatorward flank) as the width of the zonal jet changes seasonally or from year to year. During a great dust storm on Mars, for instance, the zonal jet near the northern polar night may be narrowed and shifted poleward. As noted in Section 4, these are competing effects. The Mariner 9 data used to construct Figure 1 were taken, in fact, during the final stages of one of the most global of these dust storms.

## 3.6  Conclusion

Barotropically unstable, relatively broad, high–latitude zonal jets appear to be present on all three of the inner planets having atmospheres of any consequence: Earth, Mars, and Venus. The unstable modes derived here for the Martian polar night jet can be easily related parametrically to the Venus modes found by Elson (1982) and to the terrestrial modes computed by Hartmann (1983), since all solutions to the linearized, nondivergent barotropic vorticity equation depend primarily on the Rossby number of the zonal jet, when the width of the jet is itself planetary–scale. Mars, with its fast circumpolar jet and small planetary radius, and Venus, with its slower rotation rate, both have characteristically larger $Ro$ than does Earth, but the families of barotropic modes are extensions of those studied by Hartmann (1983) for the terrestrial stratosphere. As $Ro$ increases into the range appropriate for Mars and Venus, the *fastest* growing barotropic mode shifts first from a polar $k = 1$ mode to a shorter period, but still polar, $k = 2$ mode and then possibly to a mid–latitude, longer period $k = 2$ mode. Thus, unstable modes having zonal wavenumber $k = 2$ and periods of 1–3 sidereal days are more likely to be the dominant barotropic modes on Mars and Venus, than on Earth, where modes having $k = 1$ and periods of 2–4 days seem more likely to appear. Furthermore, for the hyperbolic jet profiles examined here, the existence for Mars and Venus of two families of unstable modes having comparable growth rates but different periods and generated on opposite sides of the zonal jet implies that there may be greater variability in planetary–scale wave characteristics near the mid–latitude zonal jets on these two planets than on Earth.

Whether or not these barotropic modes or their quasi–divergent counterparts

can directly account for the temperature waves seen in the satellite radiance data for Venus, Earth, and Mars remains to be seen. Hartmann has suggested that the primary effect of barotropic instability may be to interact strongly with and to locally enhance planetary waves propagating from below. This may be particularly true for Mars where baroclinic instability at and near the surface is known to generate waves of planetary–scale at high latitudes (Barnes, 1984). The combination of the zonal wind and the horizontal wind associated with barotropically unstable waves may also produce for Mars a longitudinally varying waveguide which modulates the ability of other planetary–scale waves, however they are produced, to propagate to the levels observed. The case for Venus is, as usual, more enigmatic. In all cases, the final determination must include the effects of divergence and of the vertical, as well as meridional, variations of the high–latitude zonal jets that are present in each of the three planetary atmospheres.

## Acknowledgements

# References

Apt, J. and J. Leung,  Thermal periodicities in the Venus atmosphere.  *Icarus* **49**, 427–437, 1982.

Barnes, J. R.,  Time spectral analysis of midlatitude distrubances in the Martian atmosphere.  *J. Atmos. Sci.* **37**, 2002–2015, 1980.

Barnes, J. R.,  Midlatitude disturbances in the Martian atmosphere:  A second Mars year.  *J. Atmos. Sci.* **38**, 225–234, 1981.

Barnes, J. R.,  Linear baroclinic instability in the Martian atmosphere.  *J. Atmos. Sci.* **41**, 1536–1550, 1984.

Charney, J. G. and M. Stern,  On the stability of internal baroclinic jets in a rotating atmosphere.  *J. Atmos. Sci.* **19**, 159–172, 1962.

Conrath, B. J.,  Planetary–scale wave structure in the Martian atmosphere.  *Icarus* **48**, 246–255, 1981.

Elson, L. S.,  Barotropic instability in the upper atmosphere of Venus.  *Geophys. Res. Lett.* **5**, 603–605, 1978.

Elson, L. S.,  Wave instability in the polar region of Venus.  *J. Atmos. Sci.* **39**, 2356–2362, 1982.

Hartmann, D. L.,  Barotropic instability of the polar night jet stream.  *J. Atmos. Sci.* **40**, 817–835, 1983.

Kuo, H.-L.,  Dynamic instability of two–dimensional nondivergent flow in the barotropic atmosphere.  *J. Meteor.* **6**, 105–122, 1949.

Martin, T. Z., and H. H. Kieffer, Thermal infrared properties of the Martian atmosphere 2. The 15 $\mu$m band measurements. *J. Geophys. Res.* **84**, 2843–2852, 1979.

Newman, M., G. Schubert, A. J. Kliore, and I. R. Patel., Zonal winds in the middle atmosphere of Venus from Pioneer Venus radio occultation data. *J. Atmos. Sci.* **41**, 1901–1913, 1984.

Pfister, L., A theoretical study of three–dimensional barotropic instability with applications to the upper stratosphere. *J. Atmos. Sci.* **36**, 908–920, 1979.

Taylor, F. W., J. T. Schofield, and P. J. Valdes, Temperature structure and dynamics of the middle atmosphere of Venus. *Adv. Space Res.* **5**, 5–23, 1985.

Taylor, F. W., R. Beer, M. T. Chahine, D. J. Diner, L. S. Elson, R. D. Haskins, D. J. McCleese, J. V. Martonchik, P. E. Reichley, S. P. Bradley, J. Delderfield, J. T. Schofield, C. B. Farmer, L. Froidevaux, J. Leung, M. T. Coffey, and J. C. Gille, Structure and meteorology of the middle atmosphere of Venus: Infrared remote sensing from the Pioneer Orbiter. *J. Geophys. Res.* **85**, 7963–8006, 1980.

Venne, D. E. and J. L. Stanford, Observation of a 4–day temperature wave in the polar winter stratosphere. *J. Atmos. Sci.* **36**, 2016–2019, 1979.

Venne, D. E. and J. L. Stanford, An observational study of high–latitude stratospheric planetary waves in winter. *J. Atmos. Sci.* **39**, 1026–1034, 1982.